

# Long-Term Stability Tests of Intrinsic Fabry-Pérot Optical Fibre Sensors at High Temperatures

Dimitrios Polyzos

A dissertation submitted for the degree of Doctor of Philosophy

Heriot-Watt University

School of Engineering and Physical Sciences

January 2018

The copyright in this thesis is owned by the author. Any quotation from the thesis or use of any of the information contained in it must acknowledge this thesis as the source of the quotation or information.

## Abstract

The main aim of this thesis is to develop and gain a better understanding of intrinsic Fabry-Pérot optical fibre sensors in high temperature environments. This thesis will describe the characteristics, manufacturing process, and applications of intrinsic Fabry-Pérot optical fibre sensors and their suitability for temperature sensing in high temperature environments.

Intrinsic Fabry-Pérot optical fibre sensors with different types of sensing elements were manufactured and investigated throughout this project. The types of sensors differ at the dopant of their Fabry-Pérot cavity (sensing element), such as Ge-doped core, F-doped depressed cladding and pure SiO<sub>2</sub>. Their long-term phase stability response at temperatures up to 1150°C over up to 4 months continuously monitoring is presented. Most promising results were given by pure SiO<sub>2</sub> sensors up to 1000°C with a minimum temperature drift of less than 1°C. Above that temperature, all types of sensors showed temperature drifts from 20°C up to 100°C due to permanent changes of the core refractive index. At elevated temperatures, permanent changes of the core refractive index arise due to dopant diffusion in the optical fibre sensor, from core to cladding and vice versa, as well as tapering phenomena leading to phase response drifting and modulated behaviours.

The presence of dopant in the Fabry-Pérot cavity proved to affect the phase stability of the sensors, especially for temperatures above 1000°C. An investigation of how dopant diffusion affects the core radius by making it larger is presented in this thesis as well. Using Scanning Electron Microscopy (SEM) coupled with Energy Dispersive X-ray (EDX) Spectroscopy, optical fibre sensors tested at temperatures up to 1150°C over long periods are investigated for dopant diffusion. After 85 days at temperatures above 900°C, germanium concentration in the core of the sensor has been dropped down to the 60% of its initial dopant concentration. Through calculations of FWHM and germanium wt. % concentration, the 40% of germanium dopant that have been diffused towards the cladding expanded the core radius by 0.9µm. This can lead to expanding tapering phenomena along the optical fibre and transformation of the single mode core to a multimode core, for specific wavelengths. Also, a modelled theoretical analysis of a 2<sup>nd</sup> order mode cavity interference in the fundamental cavity has been conducted proving its correlation with the modulated phase response at high temperatures.

*To*

*Konstantinos and Anastasia*

“Love responsibility. Say: It is my duty, and mine alone, to save the world. If it is not saved, then I alone am to blame.”

“Ν' αγαπάς την ευθύνη. Να λες: Εγώ, εγώ μονάχος μου θα σώσω τον κόσμο. Αν δε σωθεί, εγώ φταίω.”

Nikos Kazantzakis/ Νίκος Καζαντζάκης

## **Acknowledgements**

First of all, I would like to thank my supervisor Dr R R J Maier who gave me the opportunity to accomplish a PhD in Applied Optics and Photonics group in Heriot Watt University. Also, I must thank him for his patience and thorough answers to all of my queries that came up during my PhD life. I believe I gained a lot during my PhD studies from his in-depth knowledge in optical fibre sensing scientific field.

Secondly, I would like to thank my second supervisor Dr W N MacPherson for being always present for a second opinion and guidance. Special thanks go to Dr Jinesh Mathew, Dr Jonathan Morton and Dr Richard Carter. The first one for always being supportive to help me with any scientific problems that came up, the second one for proof reading my thesis and the last one for the helpful suggestions on problem solving and the interesting discussions about world history.

Big thanks to my colleagues Wojciech, Niki, Georgia, Andrew, Jianyong, and Dirk for the funny times we spent in the university and especially outside of it. Also, I should give my appreciations to all the people of the Applied Optics and Photonics research group. In addition, I would like to thank EPSRC for supporting this work.

Finally, special thanks must go to my siblings Athanasios and Eleni, my girlfriend Ioanna and all my friends for supporting me in their own way individually.



# ACADEMIC REGISTRY

## Internal Examiner Declaration Form

(This form must be type written)

Candidate's Name: (in capitals)		Heriot-Watt Person ID:	
School:		Degree Sought:	

### Declaration

Have the corrections to the thesis of the above-named been carried out to the satisfaction of the examiners ?

Yes ☐ No ☐ N/A ☐

Has there been any change to the thesis title since the temporary thesis was submitted?

Yes ☐ No ☐ N/A ☐

If so, please provide details of amended title here:

--

If the Examiner's Joint Recommendation Form states (c) 'Award degree following satisfactory completion of significant changes', please complete section below to demonstrate that the particular changes are satisfactory. If (d) or (e), requiring 're-submission after further work' then all examiners are required to submit further reports.

--

I confirm that this is a re-submission.

Yes ☐ N/A ☐

The candidate is being awarded a joint degree

Yes ☐ N/A ☐

I confirm that I have seen the presentation (final bound) thesis and it has been bound in accordance with University regulations.

Yes ☐ No ☐

### Electronic Thesis

As the Internal Examiner, I confirm that the student has prepared an electronic version of the thesis in accordance with University guidelines **and it is an exact copy of the final bound thesis**

Signature:

--

In accordance with Heriot-Watt University Regulations\*, all students submitting research theses to the University for the awards of Doctor of Philosophy and/or Master of Philosophy must provide an electronic version of their final thesis. Further information on electronic thesis submission is available in the Submission and Format of Thesis Guidelines, available at <https://www.hw.ac.uk/students/studies/examinations/thesis.htm>

\* Regulation-6 (Degree of Doctor of Philosophy), paragraph 9.2; Regulation 37 (Degree of Doctor of Engineering) paragraph 12.2; Regulation 41 (Degree of Doctor of Business Administration) paragraph 8.2; Regulation 43 (Degree of Doctor of Philosophy by Published Research) paragraph 9.8, Regulation-49 (Higher Degrees of Master (Research) paragraph 7.4.7, 11.5.5 and 11.6.5)

### Internal Examiner

Print Name:		Date:	
Signature:		School:	

### Notes

- Please note that under current University regulations two presentation (final bound) and one electronic copy of the thesis are required for final submission.
- The Internal Examiner's Declaration Form should be submitted along with the presentation (final bound) and electronic copy of the thesis to the Student Service Centre.

Academic Registry/Version (2) January 2017

## ACADEMIC REGISTRY

### Research Thesis Submission

Name:	Dimitrios Polyzos		
School:	School of Engineering and Physical Sciences		
Version: <small>(i.e. First, Resubmission, Final)</small>	Final	Degree Sought:	Doctor of Philosophy in Physics

#### **Declaration**

In accordance with the appropriate regulations I hereby submit my thesis and I declare that:

- 1) the thesis embodies the results of my own work and has been composed by myself
- 2) where appropriate, I have made acknowledgement of the work of others and have made reference to work carried out in collaboration with other persons
- 3) the thesis is the correct version of the thesis for submission and is the same version as any electronic versions submitted\*.
- 4) my thesis for the award referred to, deposited in the Heriot-Watt University Library, should be made available for loan or photocopying and be available via the Institutional Repository, subject to such conditions as the Librarian may require
- 5) I understand that as a student of the University I am required to abide by the Regulations of the University and to conform to its discipline.
- 6) I confirm that the thesis has been verified against plagiarism via an approved plagiarism detection application e.g. Turnitin.

\* Please note that it is the responsibility of the candidate to ensure that the correct version of the thesis is submitted.

Signature of Candidate:		Date:	
-------------------------	--	-------	--

#### **Submission**

Submitted By <small>(name in capitals):</small>	Dimitrios Polyzos
Signature of Individual Submitting:	
Date Submitted:	

#### **For Completion in the Student Service Centre (SSC)**

Received in the SSC by <small>(name in capitals):</small>			
<b>Method of Submission</b> <small>(Handed in to SSC; posted through internal/external mail):</small>			
<b>E-thesis Submitted</b> (mandatory for final theses)			
Signature:		Date:	

## Table of Contents

<b>Abstract.....</b>	<b>ii</b>
<b>Acknowledgements.....</b>	<b>iv</b>
<b>Table of Contents .....</b>	<b>vii</b>
<b>Chapter 1 : Introduction .....</b>	<b>1</b>
1.1 Thesis Aims and Objectives .....	1
1.2 Thesis Structure .....	3
<b>Chapter 2 : Literature Review.....</b>	<b>5</b>
2.1 Introduction to Optical Fibres Sensors .....	5
2.2 Background of Optical Fibre Sensors (OFS) .....	5
2.2.1 Optical Fibre Overview .....	7
2.2.1.1 Ray Optics of Waveguiding Light in Optical Fibre .....	9
2.2.1.2 Wave Optics Principles of Light in Optical Fibre.....	10
2.2.1.3 Types of Optical Fibres.....	12
2.2.1.4 Thermo-optic (CTO) and Thermal Expansion (CTE) Coefficient.....	13
2.2.2 High Temperature Impact on Optical Fibres .....	16
2.2.2.1 Viscosity of Fused Silica (SiO <sub>2</sub> ) .....	17
2.2.2.2 Phase Transition Point—Softening of Glass.....	17
2.2.2.3 Dopant Diffusion in Optical Fibres.....	19
2.2.2.4 Effects on Optical Fibres during Optical Fibre Drawing .....	21
2.2.2.5 Summary of High Temperature Effect on Optical Fibres .....	23
2.3 Optical Fibre Sensors (OFS) .....	23
2.3.1 Temperature Sensing with Optical Fibre Sensors (OFS).....	25
2.3.2 Interferometer Theory of Fabry-Pérot OFS .....	26
2.3.3 Interrogation Data Analysis Routine on LabVIEW Software.....	31
2.4 Experimental Setup .....	35
2.5 Thermocouples (TCs).....	37
2.5.1 Annealing of Thermocouples - Hysteresis.....	38
2.5.2 Type-K and Type-N Thermocouples .....	38
2.6 Summary of Chapter 2 .....	40
<b>Chapter 3 : Manufacturing process of Fabry-Pérot sensors .....</b>	<b>41</b>
3.1 Introduction .....	41
3.2 Cleaving.....	41
3.3 Coating of Fibre Tip .....	42
3.3.1 Chromium Thickness – Thin Mirror Reflectivity .....	42
3.3.1.1 Theoretical analysis of thin mirror reflectivity .....	43
3.3.1.2 Experimental analysis of thin mirror reflectivity.....	45

3.4	Splicing.....	48
3.4.1	Splice Quality and Faulty Splices .....	48
3.4.2	Splice Strength Testing .....	50
3.5	Integration of Intrinsic Optical Fibre Fabry-Pérot sensor .....	51
3.5.1	Sensor Type 1 formation: 125µm-Cr-125µm.....	52
3.5.2	Sensor Type 2 formation: 125µm-80µm-50µm-Cr-50µm .....	53
3.5.3	Sensor Type 3 formation: 125µm-Cr-125µm (PCF-ESM12) .....	55
3.6	Conclusions of Chapter 3 .....	57
<b>Chapter 4 : Long-Term Stability Tests at High Temperatures.....</b>		<b>58</b>
4.1	High Precision Thermometer (PREMA) Error Analysis under Ambient Temperature Variations .....	58
4.1.1	High Precision Thermometer (PREMA) Stability Tests.....	59
4.1.1.1	Thermometer Stability Testing without the Use of a RTD sensor.....	60
4.1.2	Prema Thermometer Stability Testing Using a RTD sensor.....	62
4.1.2.1	RTD Sensor Positioned out of The Foam Box.....	62
4.1.2.2	RTD Sensor Heated Separately.....	63
4.1.2.3	RTD Sensor Positioned in the Foam Box .....	64
4.2	Experimental and Theoretical Sensor Sensitivity Analysis.....	66
4.3	Ge-doped (SMF28 ultra) Fabry-Pérot sensor .....	70
4.3.1	Annealing and Thermal Cycling of Ge-doped core Fabry-Pérot sensors ..	70
4.3.2	Long-Term Stability Tests of Ge-doped core Fabry-Pérot sensors .....	76
4.3.2.1	Sensor Type 1: 125µm-Cr-125µm .....	76
4.3.2.2	Sensor Type 2: 125µm-80µm-50µm-Cr-50µm (Stepped).....	81
4.4	F-doped depressed cladding (F-SM1500SC-P) Fabry-Pérot sensor .....	84
4.4.1	Annealing and Thermal Cycling of F-doped depressed cladding Fabry-Pérot sensor .....	84
4.4.2	Long-Term Phase Stability Tests of F-doped depressed cladding Fabry-Pérot sensors .....	86
4.5	Pure SiO <sub>2</sub> (ESM-12B) Fabry-Pérot sensor .....	87
4.5.1	Annealing and Thermal Cycling of pure SiO <sub>2</sub> Fabry-Pérot sensors .....	88
4.5.2	Long-Term Phase Stability Tests of pure SiO <sub>2</sub> Fabry-Pérot sensors .....	91
4.6	Conclusions of Chapter 4 .....	96
<b>Chapter 5 : Dopant Diffusion of Optical Fibres at High Temperatures .....</b>		<b>99</b>
5.1	Longitudinal Temperature Furnace's Profile .....	99
5.2	Propagating mode analysis .....	100
5.3	Schematic tapering representation of Fabry-Pérot sensor .....	104
5.4	Theoretical phase modulated behaviour .....	107

5.5	Dopant Diffusion Experimental Results.....	110
5.5.1	Fibre preparation for Energy Dispersive X-rays (EDX) analysis .....	110
5.5.2	Single EDX line scan .....	111
5.5.3	Multiple EDX line scan.....	114
5.6	Conclusions of Chapter 5 .....	122
<b>Chapter 6 : Conclusions and Future Work .....</b>		<b>124</b>
6.1	Conclusions and Discussion .....	124
6.2	Future Work .....	127
<b>REFERENCES.....</b>		<b>129</b>

## Table of Publications

### Journal Publications

1. J. Mathew, O. Schneller, **D. Polyzos**, D. Havermann, W.N. Macpherson, D. P. Hand, R. R. J. Maier, “*In-Fibre Fabry–Pérot Cavity Sensor for High-Temperature Applications*”, Journal of Lightwave Technology, Vol. 33 (12), pp. 2419- 2425, 2015.
2. Jinesh Mathew, Carl Hauser, Philipp Stoll, Christoph Kenel, **Dimitrios Polyzos** Dirk Havermann, William N. MacPherson, Duncan P. Hand, Christian Leinenbach, Adrian Spierings, Kamilla Koenig-Urban and Robert R. J. Maier “Integrating fibre Fabry-Pérot cavity sensor in to 3D printed metal components for extreme high temperature monitoring applications” IEEE Sensors Journal, 10 May 2017, Volume: PP Issue: 99.
3. **Dimitrios Polyzos**, Jinesh Mathew, William N. MacPherson and Robert R.J. Maier “Effect of Dopant Diffusion on the Long-Term Stability of Fabry-Pérot Optical Fibre Sensors”, Journal of Lightwave Technology (Volume: 35, Issue: 24, Dec.15, 15 2017)

### Conference contributions

1. **Dimitrios Polyzos**, Jinesh Mathew, William N. MacPherson and Robert R. J. Maier “Long-term stability testing of optical fibre Fabry-Pérot temperature sensors”, Proc. of SPIE - The International Society for Optical Engineering, vol. 9852 (2016)
2. **Dimitrios Polyzos**, Jinesh Mathew, William N. MacPherson and Robert R. J. Maier “High temperature stability testing of Ge-doped and F-doped Fabry-Pérot fibre optical sensors”, Proc. of SPIE - The International Society for Optical Engineering, vol. 9916 (2016)
3. **Dimitrios Polyzos**, Jinesh Mathew, William N. MacPherson, Duncan P. Hand, Robert R. J. Maier ‘Optical fibre Fabry-Pérot sensor stability at high temperatures’, Proc. SPIE 10323, 25th International Conference on Optical Fibre Sensors, (April 23, 2017) vol. 10323

4. R. R. J. Maier, D. Havermann, O. Schneller, J. Mathew, **D. Polyzos**, W. N. MacPherson, D. P. Hand, ‘Optical fibre sensing in metals by embedment in 3D printed metallic structures”, Proc. SPIE 9157, 23rd International Conference on Optical Fibre Sensors, (June 2, 2014) vol. 9157
5. Jinesh Mathew, Dirk Havermann, **Dimitrios Polyzos**, William N. MacPherson, Duncan P. Hand, Robert R. J. Maier, ‘SS316 structure fabricated by selective laser melting and integrated with strain isolated optical fibre high temperature sensor”, Proc. SPIE 9634, 24th International Conference on Optical Fibre Sensors, (September 28, 2015) vol. 9634

## Chapter 1: Introduction

This chapter presents the objective and motivation of the subject matter in this thesis and the layout of the thesis with a short description of each chapter.

### 1.1 Thesis Aims and Objectives

This thesis aims to the development and understanding of optical fibre intrinsic Fabry-Pérot sensors in harsh environments surrounded by temperatures up to 1100°C. Interferometer in-fibre Fabry-Pérot (F-P) optic sensors (**Figure 1**) are a design idea which proved to be beneficial for temperature monitoring in a temperature range up to 1100°C [1]. A thorough analysis of characteristics, functionalities, challenges, and performance of Fabry-Pérot optical fibre sensors at high temperatures, is presented.

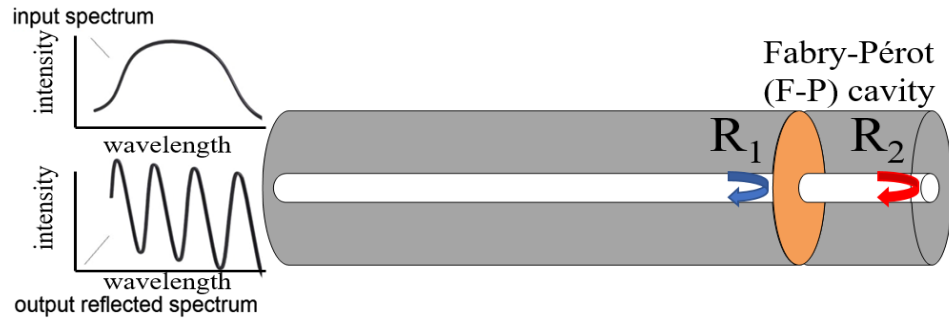


**Figure 1.** General operation principle of a Fabry-Pérot in-fibre optical sensor. Both input and output reflected spectra of the sensor are depicted.

**Figure 2** depicts the cross section and dimensions of a standard telecommunication optical fibre. For each intrinsic Fabry-Pérot sensor manufactured throughout this work was used an 8.2µm core diameter single mode optical fibre (SMF28 ultra). Many intrinsic Fabry-Pérot sensors were manufactured and were tested evaluating their repeatability and phase response stability at high temperatures. The goal is to achieve intrinsic Fabry-Pérot optical fibre sensors suitable and robust for long-term temperature sensing in a range between 800°C and 1100°C [2, 3]. The resolution of Micron Optics interrogator which has been used for our data acquisition is 5pm. As the temperature range we aim to test the sensors in this thesis is very high, a sensor resolution of less than 5°C would be suitable and applicable according to our data analysis equipment.



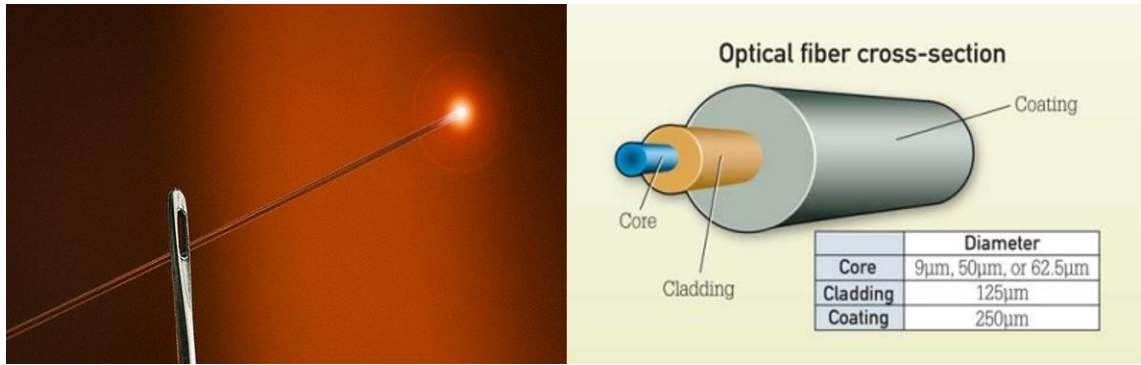


**Figure 2.** The left photo depicts an optical fibre threaded in a needle [4], while the right photo presents the cross section and dimensions of an optical fibre [5].

Different sensing elements were used during the manufacturing process, investigating the optimum type of Fabry-Pérot sensor for temperature monitoring. The long-term stability response up to 4 months of continuous monitoring was conducted. During the long-term stability tests, sensors were exposed to temperatures between 800°C and 1150°C. The goal is to estimate the maximum temperature at which the sensors can continuously function without any phase drifting. Also, the source which causes sensor's phase drifting is an objective that is investigated in this thesis. Thus, detailed study of the challenges, such as dopant diffusion and tapering phenomena that might occur to a sensor at extreme heat conditions is addressed [6, 7]. Experimental chemical element analysis, mapping the heated optical fibre's cross section, combined with theoretical calculations of propagating mode analysis helped to address and justify the dopant diffusion phenomena and the modulations at the phase response of the Fabry-Pérot optical fibre sensor. The novelty in this thesis can be spotted on the long-term stability up to 4 months of the intrinsic Fabry-Pérot optical fibre sensors, as well as the combination of phase and frequency, extracted from their spectrum, with which ambient's temperature change can be detected. In addition, the EDX multiple linescan mapping of germanium distribution at the cross section of the optical fibre sensor can be considered an innovative method for the investigation of dopant diffusion and tapering phenomena in optical fibres.

The long-term goal after establishing the phase response stabilization of in-fibre Fabry-Pérot (F-P) optical fibre sensors is their embedment in metallic structures throughout additive manufacturing. This can be achieved using Selective Laser Melting (SLM) and Layered Metal Deposition (LMD) techniques, in order to allow temperature sensing while the in-fibre optical sensor is embedded in a metallic component (**Figure 3**). A successful integration of these components is highly desirable for harsh

environment applications in aircraft, energy and aerospace and aircraft turbine systems where high temperature conditions, up to 950°C, take place [8-11].

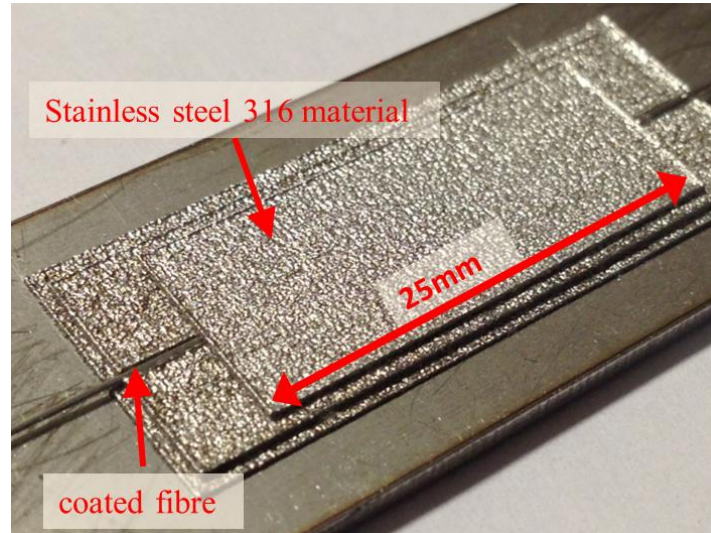


*Figure 3. Optical fibre embedded into metallic structure (Stainless steel 316) using Selective Laser Melting [9].*

## 1.2 Thesis Structure

The chapters of the thesis are described below:

- **Chapter 2** focusses on the theoretical background of optical fibre sensing applications. Fibre optic technologies for high temperature measurement reported in literature are presented, leading to the purpose of this thesis. The basic principles of optical fibre waveguiding and operation of a Fabry-Pérot fibre sensor are specified. Additionally, a thorough analysis of the mathematical equations, which describe the Fabry-Pérot interferometer sensor, are presented. On these equations is based the data analysis routine that has been built on LabVIEW software. At last, a short description of the experimental setup and equipment that has been used for the completion of this thesis is also outlined.
- **Chapter 3** describes the manufacturing process of building an intrinsic optical Fabry-Pérot fibre sensor. Each step of the manufacturing process such as cleaving, thin film deposition and splicing techniques is analysed. Different type of sensing cavity elements characterizes each type of intrinsic Fabry-Pérot sensor. The manufacturing process of each sensing element type is demonstrated in this chapter. The limitations of these manufacturing techniques are

highlighted as well, leading to a well-defined optical fibre sensor without losses and interferences in its sinusoidal spectrum. A theoretical and experimental analysis of thin mirror's reflectivity is obtained. In addition, breaking strength experiments were conducted, finding the optimum splice strength of the sensor.

- **Chapter 4** investigates the accuracy and errors of temperature recording lying in the experimental equipment that has been used throughout the high temperature experiments. PREMA thermometer was subjected to ambient temperature control, in order to investigate the temperature monitoring stability. Furthermore, is presented the annealing cycle, thermal cycle, and the long-term stability response of each Fabry-Pérot (F-P) sensor that has been manufactured. A thorough investigation of the phase stability response of Fabry-Pérot sensor is described, between a temperature range of 850°C and 1100°C, for long periods of time up to 4 months. An experimental and theoretical analysis of sensors with various cavity lengths is also examined.
- **Chapter 5** focusses on the dopant diffusion and tapering phenomena occurring in an optical fibre which have an impact on sensor's phase stability and robustness at high temperatures. Scanning Electron Microscopy (SEM) coupled with Energy Dispersive X-ray (EDX) spectroscopy was used to investigate the germanium dopant diffusion of optical fibre sensors that have been heated up to 1150°C over 100 days. Based on theoretical modelling calculations, an analysis of a 2<sup>nd</sup> order mode interference in the fundamental cavity has been conducted. In addition, an evaluation of the circumstances that could rise a 2<sup>nd</sup> order mode cavity in the optical fibre, are analysed.
- **Chapter 6** reviews the work that was conducted throughout this scientific research followed by an analysis of the core conclusions and providing a viewpoint for future work.

## **Chapter 2: Literature Review**

### **2.1 Introduction to Optical Fibres Sensors**

The goal of this chapter is to establish the background of the research work presented in this thesis. Initially, is provided a summary of optical fibres in which their properties and operational characteristics are described. Even though electromagnetic theory is needed for the explanation of optical fibre functionality at high temperatures, it is similarly being explained by basic optics theory, both described in this chapter. Based on both theories, the challenges and performance impacts on optical fibres at high temperatures are also reviewed. Additionally, their use as sensors for measuring various environmental parameters is presented, focussing more to the essence of this work which is high temperature sensing. Moreover, there will be addressed the main advantages and disadvantages of this interferometric technology providing a hopeful technique for accurate and stable temperature monitoring at high temperatures.

The main sensor investigated in this research is the intrinsic Fabry-Pérot optical fibre sensor. A description of basic operation principles of Fabry-Pérot interferometry and its implementation in optical fibre sensors is included in this chapter. The interrogation routine of data analysis built on LabVIEW software is also described. Finally, a brief description of thermometers and thermocouples are presented, including the experimental setup and equipment that had been used for the completion of the scientific experiments of this thesis.

### **2.2 Background of Optical Fibre Sensors (OFS)**

In 1970, Corning Glass Works successfully manufactured single mode fibres with attenuation less than 20dB/km using titanium dopants in silica glass [12]. Three years later, Bell Laboratories established a modified process using chemical vapour deposition forming ultra-transparent glass by heating chemical vapours and oxygen. In this way, low-loss optical fibres could be massively produced [13]. Nowadays, optical fibres are still being manufactured by chemical vapour deposition process remaining an ordinary method.

In the last few decades, optical fibre sensing has attracted significant attention due to the disadvantages of the conventional sensing techniques. These disadvantages have given the opportunity to make significant improvements to a variety of optical fibre sensors for measuring various conditions. Fibre optic sensors offer a series of

advantages as they prove to be lightweight, highly sensitive, immune to electromagnetic radiation and they can be embedded in metallic components[8, 10, 14]. Depending on the application, an optical fibre sensor can be used in spaces characterized by micron size scale (**Figure 2**), or at places with high voltage electricity or flammable materials at the remote location such as jet fuel. Also, they can be multiplexed by using distributed Bragg gratings along its length for each sensor making them suitable for in remote sensing [15]. Their multiplexing ability to connect many optical sensors of different types to a single optical fibre is cost effective and less complex for installation [16]. Liquid level [17], refractive index [18], strain [19], pressure [20], temperature [2, 11, 21, 22] and many of other measurands can be measured by optical fibre sensors. Hence, they have been broadly used for many applications in military services, biometric companies, civil engineering structural health monitoring, aircraft health monitoring and for petrochemical installation in oil industry [19, 23].

Temperature measurements require suitable sensor technologies for real-time process condition monitoring at high temperatures exceeding 1000 °C [24]. At high temperatures electrical sensors showed restrictions at their reliability due to disturbances by electromagnetic fields. Due to their inherent electrical conductivity, they are vulnerable to electromagnetic interference and risky high voltages can introduce errors during measuring. Furthermore, electrical sensors such as thermocouples exhibit low-level electrical signals with susceptibility to noise. The resistance of long lead wires creates a voltage drop which makes it difficult to use these sensors for remote sensing. In addition, they don't offer the capability of multiplexing, compared to optical fibre sensors. Optical fibre sensors made by fused silica ( $\text{SiO}_2$ ) material proved to eliminate these limitations [12].

Many applications need sensors that exhibit sustainability at high temperature processes of many hundreds Celsius degrees. Fused silica optical fibre sensors proved to be an excellent choice. One of their characteristic is their high strain point which is in the range of 990-1100°C [25], making them an excellent candidate with potential to function at temperatures up to 1100°C. Their softening point is close to 1200°C [26] meaning that optical fibre sensors based on fused silica material are very suitable for applications in the energy and aerospace industry, which demand high temperature environments [21, 27, 28]. Mechanical strength of fused silica fibres exhibits no stress ageing when they are subjected to harsh conditions, for example humidity or extreme temperature surroundings. Usually, optical fibre sensors are exposed to extreme

condition levels of mechanical demands, temperatures, and chemical aggressiveness exceeding the limits of a standard telecommunication fibre (SMF28). An extended research work has been done on optical fibre sensors at high temperatures such as sapphire fibre sensors up to 2000°C [29, 30], regenerated Bragg gratings up to 1100°C [21] and intrinsic Fabry-Pérot sensors up to 1200°C [11, 31].

Optical fibres exhibit some limitations which can affect their durability and robustness. Mechanical damage to the fibre surface during installation or construction activities, stripping for example, can limit its functionality degrading fibre's strength and leading to the development of surface cracks. Dust, humid atmosphere, and chemical substances during fibre treatment can cause additional strength degradation as well [12, 23]. Additionally, fibre optic sensors show limitations on cost rather than technology as the installation costs while dropping, are still high as specialized optical test equipment is often required. Also, optical fibre sensors are affected by interference from multiple effects. For instance, a sensor used for measuring pressure or strain exhibits sensitivity to temperature variation [32].

In general, optical fibres can survive at high temperatures better than electrical cable sensors as they prove to be more robust in the presence of destructive chemicals and harsh temperature environments. Intrinsic Fabry-Pérot optical fibre sensors have been extensively examined in our research to investigate stability at high temperatures.

### ***2.2.1 Optical Fibre Overview***

Usually, in an optical fibre the light is guided in the core, which is surrounded by an external cladding. Fibre's core refractive index ( $n_1$ ) is constant and slightly higher than the refractive index ( $n_2$ ) of the cladding, depicted in **Figure 4**. The three regions of a typical optical fibre are presented below:

1. primary-secondary buffer (plastic material for stress and handling protection)
2. cladding (fused silica glass with refractive index  $n_2$ )
3. core (fused silica glass with refractive index  $n_1$ ) [33-35]

Optical fibres are usually made of fused silica material ( $\text{SiO}_2$ ) of high purity. Fused silica has the specific characteristic of no solidification at discrete freezing temperature, on the contrary its hardness gradually increases. Additionally, it is extremely transparent and is characterized by extremely low light transmission loss [36]. However, the optical domain of a fused silica optical fibre presents a number of different types of attenuation such as absorption losses, scattering losses and dispersion phenomena [12, 35, 36].

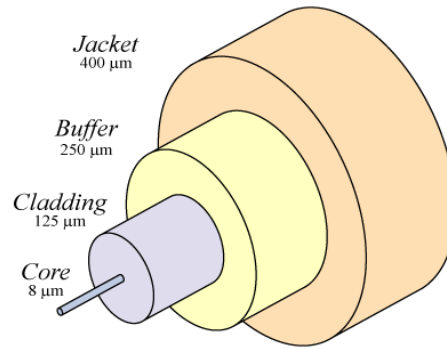


**Figure 4.** A schematic representation of standard single mode communication fibre (SMF28), showing the different diameters of the component layers [37].

Light attenuation depends on the type of the fibre and the wavelength that is travelling through, which shows an exponential power decrease with regards to distance. Scattering phenomena and absorption of light in the optical fibre are the main reasons of light attenuation, as it is presented in **Figure 5**. Waveguide imperfections (horizontal dashed line) such as molecular resonances and wavelength impurities in fibre's material, is one reason that can absorb the waveguiding light. Also,  $\text{OH}^-$  absorption (red circles in **Figure 5**) is generated by the presence of hydrogen or hydroxide ions resulting from water residuals during manufacturing or scattering humidity in the environment. UV absorption results from electronic absorption bands in the ultraviolet region, which they are associated with the band gaps of amorphous glass materials. Finally, Rayleigh which is wavelength dependent is caused by material inhomogeneities which are smaller than light signal's wavelength. All the above mentioned factors contribute to the attenuation of light travelling through an optical fibre. The wavelengths for which light exhibits the minimum loss ( $<0.2\text{dB}$ ) is at  $1.3\mu\text{m}$  and  $1.55\mu\text{m}$ . The units of attenuation coefficient are usually expressed in  $\text{dB/km}$  [38].

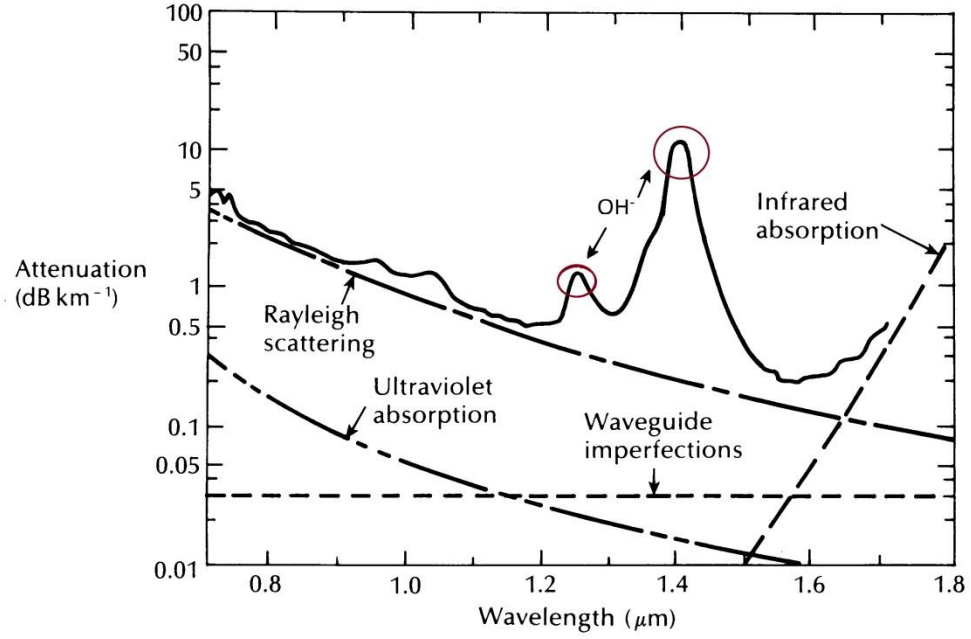


**Figure 5.** Attenuation behaviour (solid black line) of a fused silica ( $\text{SiO}_2$ ) optical fibre with respect to wavelength [39]. The dashed/dotted lines represent the attenuation of an optical fibre caused by various factors individually.

#### 2.2.1.1 Ray Optics of Waveguiding Light in Optical Fibre

The refractive indices of the cladding region and the core region ( $n_1 > n_2$ ) differ by a very small percentage. Based on this regime, total internal reflection is occurring and the waves travel across the fibre by multiple scattering at the interface of these two regions. **Figure 6** shows total-internal reflection (TIR) phenomenon where incident light ray hits on a boundary of two mediums, with difference in density, at a larger angle than the critical angle, regarding the normal of the surface. Total internal reflection takes place when the critical angle ( $\alpha_c$ ) is the same with the angle of incidence, given by **Equation 1**. The outcome is the reflected wave to shift in phase, which is related with the incident angle and both media refractive indices (RI) [34].

$$\alpha_c = \sin^{-1} \frac{n_1}{n_2} \quad \text{Equation 1}$$



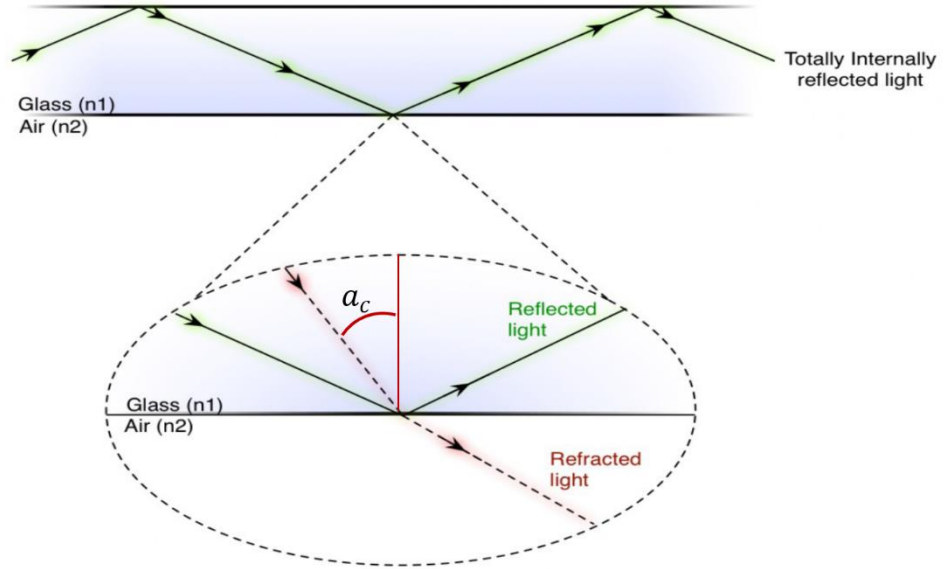


**Figure 6.** Schematic representation of total internal reflection in the fibre.

**Figure 6** shows the total internal reflection taking place in a fibre's core where a waveguiding signal travels through. Only light of a specific angle ( $\alpha_c$ ) will be reflected, any other light will be refracted out of the medium. This can be used to make light travel through a suitable guide such as glass or water [36].

$$\Delta = \frac{n_1 - n_2}{n_1} \quad \text{Equation 2}$$

$$V = k_0 * \alpha * (n_1^2 - n_2^2)^{\frac{1}{2}} = k_0 * \alpha * NA \quad \text{Equation 3}$$

where  $k_0 = 2\pi/\lambda$  is the wavenumber,  $\alpha$  is the radius of the core and  $\lambda$  is transmitted light's wavelength. **Equation 3** shows that the V number is proportional to both numerical aperture (NA) and core's radius ( $\alpha$ ), and is inversely proportional to wavelength ( $\lambda$ ). The V normalized frequency provides information about the optical fibre's modes, determining the number of the transmitted modes and consequently if the optical fibre will be multimode or single model [40, 41].

### 2.2.1.2 Wave Optics Principles of Light in Optical Fibre

Light guidance by optical fibres can be understood by considering rays of light and the principle of total internal reflection. However, for single-mode fibres where only one mode can propagate, a more thorough description of light propagation is provided by electromagnetic wave theory. Most optical fibres have a radially symmetric

refractive index profile and exhibit very low refractive index difference between cladding and core. Hence, a weakly guiding approximation can be used on them, where their propagating modes can be characterised as linearly polarized (LP) modes [42-44]. The intensity distribution is derived after solving the Maxwell equations, where the exact solutions for the electromagnetic field components can be found. Due to the cylindrical geometry of the optical fibre, the wave propagation solutions have the form of Bessel functions. **Equation 4** presents, in cylindrical coordinates, the wave equation for the complex electric field profile  $E(r, \phi)$ . A thorough analysis on Bessel functions it is not the purpose of this thesis and it can be found in literature [39, 43].

$$\frac{\partial^2 E}{\partial r^2} + \frac{1}{r} \frac{\partial E}{\partial r} + \frac{1}{r^2} \frac{\partial^2 E}{\partial \phi^2} + \beta * E = 0 \quad \text{Equation 4}$$

The fundamental mode includes two eigenmodes, differing only by their polarization ( $HE_{11}$  and  $EH_{11}$ ). The modes in a cylindrical dielectric waveguide are described as either TE, TM or hybrid. The hybrid modes are separated to 2 categories, HE modes where the axial electric field distribution  $E_z$  remains larger compared to  $E_r$  or  $E_\phi$ , and EH modes where the axial magnetic field distribution  $H_z$  remains larger compared to  $H_r$  or  $H_\phi$  [36, 41]. **Table 1** presents the V normalized frequency regions and their correspondent linear polarized propagating modes and degenerate modes. The latter modes share the same propagation constants ( $\beta$ ) but different orientations, for instance  $LP_{lm}$  modes with  $l \neq 0$  are degenerate. Many modes can be supported for V number larger than 5.1356 [43]. However, our work was conducted with single mode optical fibres which under extreme heating we estimate that they can support a 2<sup>nd</sup> order mode, where its normalized frequency lies between 2.4048 and 3.8317.

**Table 1. V normalized frequency regions and the correspondent modes of propagation.**

V number	Linear Polarized modes ( $LP_{lm}$ )	Degenerate modes	Full number of modes
<b>0 - 2.4048</b>	$LP_{01}$	$HE_{11}$	2
<b>2.4048 - 3.8317</b>	$LP_{11}$	$TE_{01}, TM_{01}, HE_{21}$	6
<b>3.8317 – 5.1356</b>	$LP_{21}, LP_{02}$	$HE_{12}, EH_{11}, HE_{31}$	12

The effective refractive index ( $n_{eff}$ ), also called modal index, has the analogous meaning with the phase constant ( $\beta$ ) for light propagation in a waveguide. Their relationship is linear for a specific wavelength, given by **Equation 5**. The effective

refractive index of guided modes takes values between the refractive indices of cladding and core. The effective index is not just a material property, but depends on the design of the waveguide, so it could be a complex quantity. In that case, the imaginary part describes gain or loss [45]. The intensity profile of the lowest-order mode, which is  $LP_{01}$ , it is conformable to a Gaussian distribution [44, 46].

$$\beta = n_{eff} * \frac{2\pi}{\lambda} = n_{eff} * k_0 \quad \text{Equation 5}$$

**Figure 7** shows the effective refractive index with respect to  $V$  parameter which correspond to the first seven modes in an optical fibre. Single-mode propagation is achieved, for a given wavelength, when  $V < 2.405$ , where only  $HE_{11}$  ( $LP_{01}$ ) mode can be supported. For normalized frequency values larger than 2.405, more modes are introduced in the optical fibre. As it is presented in the latter figure, the  $n_{eff}$  for every mode is monotonically increased with regards to the normalized frequency. An explanation is that the modal fields are more confined in the core with the increase of the  $V$  number.

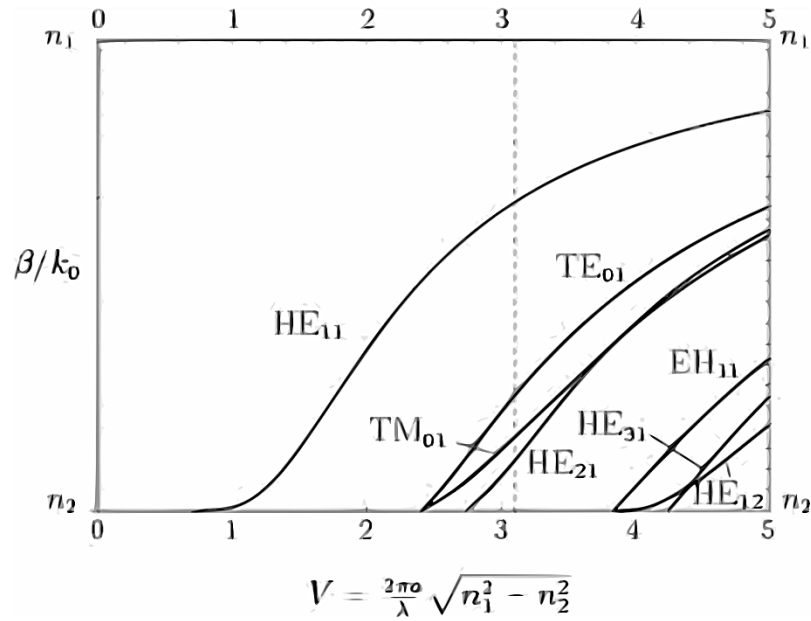


**Figure 7.** Effective refractive index with respect to normalized frequency of the seven lowest-order modes [44].

### 2.2.1.3 Types of Optical Fibres

**Figure 8** demonstrates the three most common optical fibre types which are from top to bottom the multimode stepped index fibre, the multimode graded index fibre and the single-mode stepped index fibre, respectively. Additionally, the diameters, refractive index profiles and output pulses of each type of optical fibre are depicted in **Figure 8**.

The single mode stepped refractive index fibre is the type we are currently using for the development of Fabry-Pérot optical fibre sensors. The number of guided modes in a stepped index optical fibre can be defined by **Equation 3** and is given by  $V^2/2$  [47]. A thorough analysis of the refractive index profile of various optical fibres, such as F-doped depressed cladding, Ge-doped core and graded index profile fibres can be found in the literature [48].

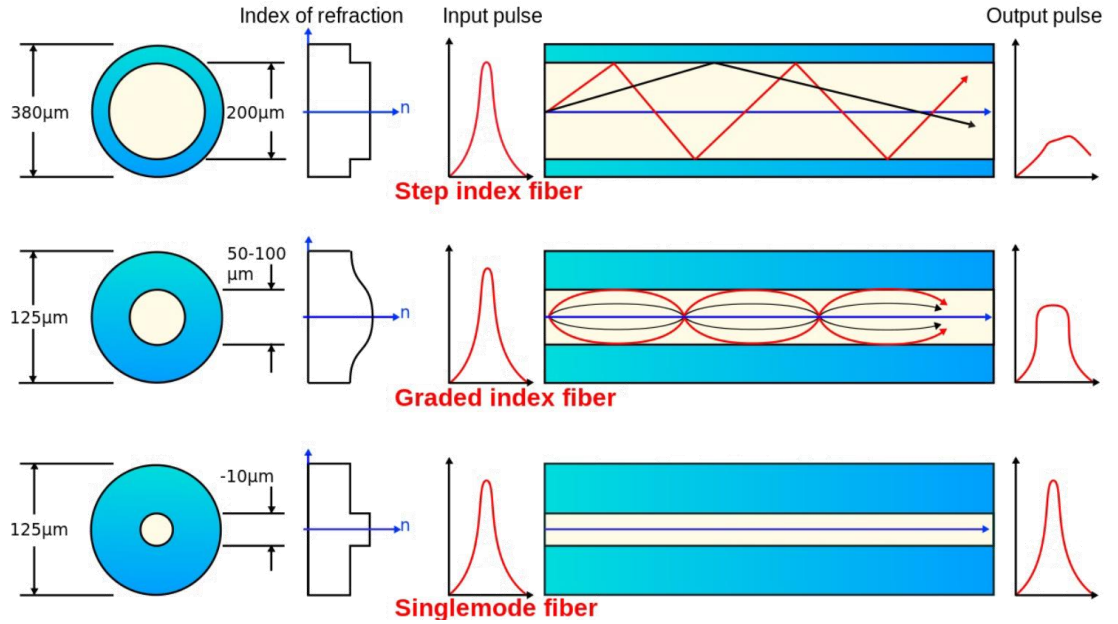


**Figure 8. Types of optical fibres. From top to bottom are depicted the multimode stepped index fibre, multimode graded index fibre and single-mode stepped index fibre [47].**

For the step index (single mode or multimode) optical fibre, the core follows a constant refractive index profile. Instead, graded index optical fibres show a non-linear symmetric refractive index profile, gradually decreasing from the core's centre towards cladding. As a result, the rays travel through the core in a twisting form around the optical axis, known as intermodal dispersion arising by different modes traveling with different speeds [49, 50]. High temperature impact on single mode refractive index profile proved to provoke a transformation to multimode graded refractive index profile [51]. Propagating modes characteristics of graded-index optical fibres, with a core refractive index which varies arbitrarily with radius, have been studied in [52, 53], using the most accurate approximations.

#### **2.2.1.4 Thermo-optic (CTO) and Thermal Expansion (CTE) Coefficient**

Another essential point which needs to be understood is how temperature affects the refractive index of the optical fibre, and how heat induces the basic material of the sensor, which is fused silica ( $\text{SiO}_2$ ). The thermo-optic coefficient (CTO) and dispersion

defined by  $\frac{dn}{dT}$ , and  $\frac{dn}{d\lambda}$ , respectively, are also characteristics of optical glasses which are used in laser devices. The refractive indices of the core and the cladding can be calculated by the dispersion Sellmeier equation (**Equation 6**). The refractive index values of core and cladding, at 1550nm, which were used for theoretical modelling are 1.44934 and 1.44395, respectively. Both emanate from:

$$n(\lambda) = \sqrt{1 + \sum_{i=1}^3 \frac{A_i \lambda^2}{\lambda^2 - B_i^2}} \quad \text{Equation 6}$$

where  $\lambda$  is the wavelength and  $A_i$ ,  $B_i$  are the Sellmeier coefficients. The Sellmeier coefficients ( $A_1, A_2, A_3, B_1, B_2, B_3$ ) that were used, can be found in literature [54].

Medium absorbs part of the transmitted laser power exhibiting heat increase, which consequently changes its refractive index. Ambient temperature variations will have analogous effects at the refractive index, as well. In 1995 G.Ghosh proposed that thermo-optic coefficient of optical glasses is mostly affected by the temperature coefficient of the excitonic band gap ( $E_{eg}$ ), an isentropic band gap ( $E_{ig}$ ) and the thermal expansion coefficient ( $\alpha$ ), rather than the temperature coefficient of the electronic polarizability that was considered to be the basic reason in the first place [55-57]. In transmission region, thermo-optic coefficient (CTO) which describes the variation of refractive index with respect to temperature, is dispersive. The dispersions of the refractive index and the thermo-optic coefficient, are not equal. Thermo-optic coefficient includes contributions of both optical phonons and electrons, and it can be described by **Equation 7**.

$$2n \frac{dn}{dT} = (n_0^2 - 1) * \left( -3\alpha R - \frac{1}{E_{eg}} \frac{dE_{eg}}{dT} R^2 \right) = G * R + H * R^2 \quad \text{Equation 7}$$

In **Equation 7**,  $n_0$  corresponds to the refractive index of low-frequency in the infrared region,  $\alpha$  corresponds to the thermal expansion coefficient,  $E_{eg}$  corresponds to the excitonic bandgap, and  $R$  is the normalized dispersive wavelength, determined by

$$R = \frac{\lambda^2}{\lambda^2 - \lambda_{ig}^2} \quad \text{Equation 8}$$

where  $\lambda_{ig}$  is the corresponding wavelength to the isentropic bandgap,  $E_{ig}$ .

At the second part of **Equation 7**, constant  $G$  is correlated to the thermal expansion coefficient ( $\alpha$ ) while constant  $H$  is correlated to the temperature coefficient of the excitonic band gap ( $E_{eg}$ ). Obviously, these two factors control the thermo-optic

coefficient, from which  $dn/dT$  can take positive or negative values. In addition, thermo-optic coefficient of the glass can be affected by the type and concentration of the dopant in the optical fibre, which is used to increase the refractive index of the core [58]. For optical glasses, fibre glasses, and non-linear crystals the contribution from the thermal expansion coefficient ( $\alpha$ ), which is the first factor, is negative as  $\alpha$  is normally positive.

The contribution is also small, more specific in the order of  $10^{-6}/^{\circ}\text{C}$ . Additionally, the temperature variation of the excitonic band gap ( $E_{eg}$ ), which is the second factor, is normally negative for the glasses and non-linear crystals [59]. Due to the fact that the first part is also negative this contribution it will be positive and larger than the first contribution to produce positive values of  $\frac{dn}{dT}$  [55, 60]. Analysing his experimental refractive-index data, Ghosh's calculations showed a dependence of  $E_{eg}$  from temperature through a nonlinear behaviour [57]. With the significant help of LabVIEW software package, we developed a theoretical model which includes the non-linearity of the thermo-optic coefficient quoted in **Equation 9**.

$$\frac{dn(T)}{dT} = a + b * T + c * T^2 \quad \text{Equation 9}$$

The values of  $a$ ,  $b$  and  $c$  parameters that have been used for our theoretical modelled calculations are  $8.16638 \times 10^{-6}$ ,  $1.04124 \times 10^{-8}$ , and  $-5.59781 \times 10^{-12}$ , respectively [54]. The latter values characterize the thermo-optic coefficient of fused silica. Nevertheless, optical fibre's core is made from fused silica doped with germanium to increase the refractive index, according to SMF28 ultra fibre spreadsheet. The germanium dopant will alter the thermo-optic coefficient. Nevertheless, given that the difference between the refractive index of the core and the cladding is approximately  $\sim 0.36\%$  [61] the exact germanium concentration in the core is very small. Thus, the temperature response of both optical fibre and fused silica are considered identical.

When a material is heated by a temperature difference  $\Delta T$ , expansion takes place. This expansion over its initial length can define the thermal expansion coefficient. The mathematical equation of TCE for an elongation of an optical fibre is linear and is given by **Equation 10**. An important measure of thermal shock resistance of glass is its expansion as the temperature increases. Normally, if the expansion coefficient is high then a rapid heating or cooling can cause a fracture to the glass [62].

$$\alpha = \frac{\Delta L}{L_0 \Delta T}$$

**Equation 10**

**Figure 9** and **Figure 10** show the dependency of the thermal expansion coefficient ( $\alpha$ ), for various doped optical fibres, on temperature and on dopant's relative refractive difference, respectively. Additionally, the thermal expansion coefficient it is the reason for the growth of thermal stress at the core-cladding interface, in doped silica fibres. This effect can be relieved with thermal annealing [63]. This is caused due to the two different materials of the core (Ge-doped  $\text{SiO}_2$ ) and cladding ( $\text{SiO}_2$ ). A difference between the TCEs of less than  $2 \times 10^{-7} \text{ }^\circ\text{C}^{-1}$  is optimum for glass sealing, avoiding any failure at high temperatures [62].

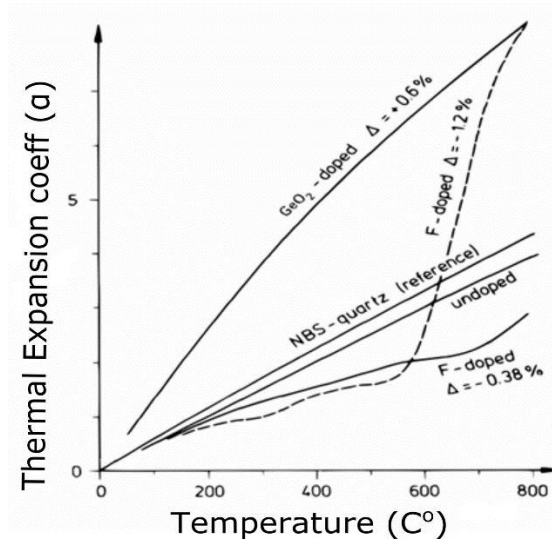


**Figure 9.** Thermal expansion coefficient for various doped optical fibres with respect to temperature[63].

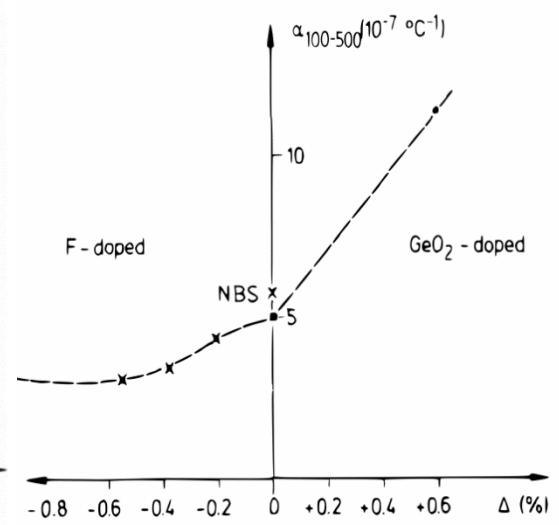


**Figure 10.** Averaged thermal expansion coefficient for Ge-doped and F-doped optical fibre with respect to dopant concentration[63].

### 2.2.2 High Temperature Impact on Optical Fibres

Fused silica glass ( $\text{SiO}_2$ ), has many characteristics making it reliable to withstand high temperatures. Nevertheless, as everything in the world likewise optical fibres have their limitations. Important issues rise when silica optical fibres are used at high temperatures. Fused silica glass is characterized by high viscosity, which allows the glass to be shaped, cooled, and annealed without any crystallization phenomena. Also, fused silica glass has very low thermal expansion coefficient which makes it extremely resistant to thermal shocks. This material exhibits inertia to chemicals except to hydrofluoric acid, which can dissolve fused silica. In addition, at temperatures above  $1100^\circ\text{C}$  and especially when contaminants such as sodium, phosphorus, and vanadium

are present, fused silica glass will devitrify forming cristobalite crystals where its properties will be destroyed [64].

### 2.2.2.1 Viscosity of Fused Silica ( $\text{SiO}_2$ )

In glasses, viscosity determines melting conditions, annealing temperatures, crystallisation rate, and maximum temperature of usage. Viscosity is highly connected with temperature, which defines a medium's resistance to flow and it is associated with structural diffusion, defined by an activation energy  $Q$ . **Figure 11** shows the relationship between viscosity and temperature of vitreous silica, which is very similar with fused silica ( $\text{SiO}_2$ ) as they are both amorphous materials. In the same figure the corresponding temperatures for strain and annealing point of vitreous silica are presented. The strain point indicates the temperature where glass molecules have reached to a state at which no more strain can be introduced, while annealing point is the temperature at which residual internal stresses are released. The viscosity of the fused silica decreases with temperature increase, obtaining its softening point above  $1600^\circ\text{C}$ . **Equation 11** shows the mathematical definition of viscosity, described in terms of activation energy ( $Q$ ) and temperature ( $T$ ) in Kelvin.

$$\eta(T) = A * \exp\left(\frac{Q}{RT}\right) \quad \text{Equation 11}$$

where  $R$  is the molar gas constant, and  $A$  is a constant [64, 65].

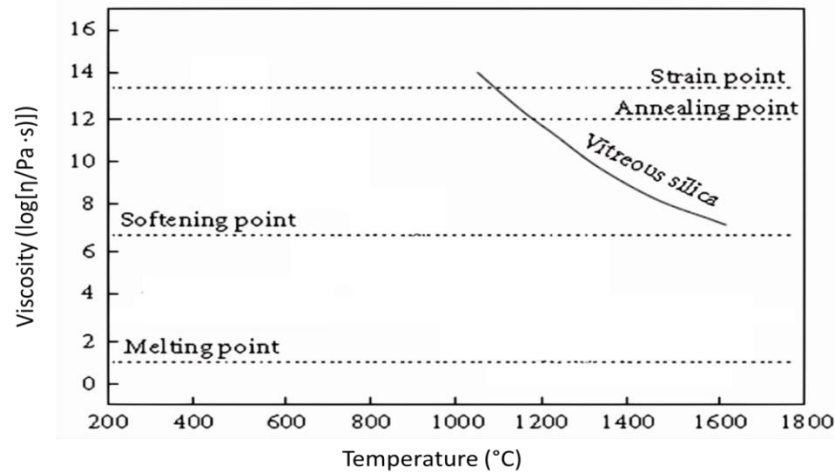


**Figure 11.** Viscosity (logarithmic scale) for vitreous silica with respect to temperature. Vitreous glass has strain and annealing point at  $1100^\circ\text{C}$  and  $1150^\circ\text{C}$ , respectively [65].

### 2.2.2.2 Phase Transition Point—Softening of Glass

The annealing process causes regrouping to an optical fibre's structure. Also it proved to be dependent on optical fibre's mechanical and thermal history [66]. Some



temperatures, such as the glass transition temperature and the softening-point temperature, characterize viscosity's gradual change with respect to temperature (**Figure 12**). In the same figure the density of glass and crystal, with respect to temperature, can be seen. Above the transition temperature, density of glass starts decreasing pushing glass to a malleable state. The transition temperature of fused silica is  $T_g \sim 1250^\circ\text{C}$ . Usually, the transition temperature of optical fibre's core is slightly lower than cladding's, due to the presence of dopants [67]. The softening point of fused silica glass is roughly  $1650^\circ\text{C}$ . At this temperature, a fast deformation will take place at the glass, as it doesn't have an accurate melting point. Glass tends to become increasingly softer with temperature increase, increasing in that way its viscosity [68]. Some of the parameters which significantly drop the lifetime of optical fibres are mechanical stress, temperature, chemical environment and relative humidity [69].

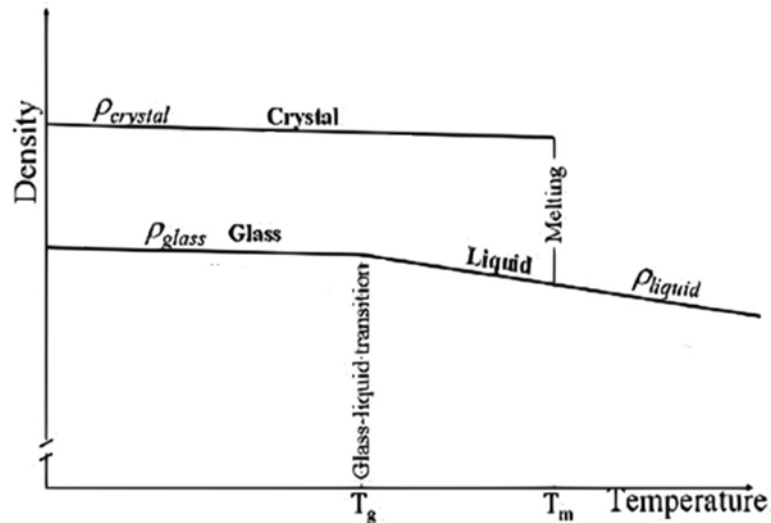


**Figure 12.** Density and phase changes of glass and crystal, above and under the transition temperature [70].

To avoid important surface alterations, glass elements should stay below  $150^\circ\text{C}$  to  $200^\circ\text{C}$  of the glass transition temperature. Due to the fact that glass transition temperature defines a second-order phase transition similar to melting, at such high temperatures the temperature dependence of various properties can change. For instance, significant changes take place to many properties such as static dielectric constant, the thermal expansion, the viscosity, shear modulus, heat capacity, and many other properties of glasses [70].

### **2.2.2.3 Dopant Diffusion in Optical Fibres**

Another essential effect which proved to be important for optical fibre's performance at high temperatures is dopant diffusion. As it was described in previous sections, optical fibres are normally being doped with various elements to increase or decrease the refractive index of the core or the cladding, respectively. According to literature review [7, 71-73] diffusion of dopants in the optical fibres proved be feasible at high temperatures.

Silica optical fibres have a high softening temperature which supports them to retain their mechanical principles even at 1000°C. Dopant diffusion influences the refractive index profile during manufacturing process of the optical fibre. Various processes such as fibre drawing, splicing, tapering, and testing of optical fibres at high temperatures can cause dopant diffusion effects at optical fibres. Thermally expanded core (TEC) fibres have an expanded mode field diameter attained by heating a step-index single-mode fibre locally at high temperature (of approximately 1300°C to 1650°C) and diffusing the germanium dopant out of the core. The heating temperature and its duration control the expansion rate of the core. As a result, long term exposure of optical fibres to high temperatures causes an irreversible change in the fibre properties, converting gradually the refractive-index core profile to a graded shape profile [73]. Almost certainly this effect is explained by the inwards/outwards diffusion of fluorine/germanium atoms to the core/cladding. This effect is significantly enhanced at temperatures higher than 1000°C [72, 74].

Moreover, the diffusion behaviour of fluorine and germanium dopants above 1000°C is of high concern. Due to the fact that fluorine can be diffused faster than other common dopants such as phosphorous and germanium, it should be attained an a priori knowledge of its impact on optical fibre's performance [7, 71].

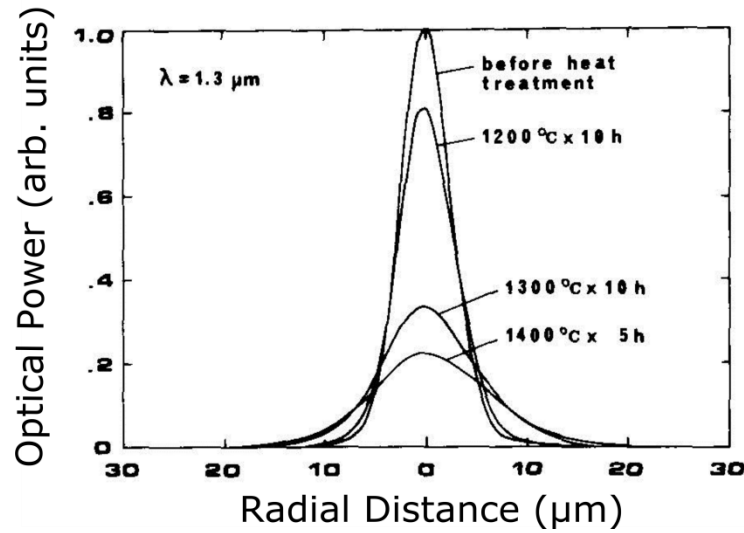


*Figure 13. Measured modal power distributions along the centre of cross section of a fibre for various heat-treatment conditions. The distributions are normalized by the modal power[73].*

Modal and germanium concentration distributions were measured, showing their broadening due to dopant diffusion after heating an optical fibre. **Figure 13** shows the measured near-field patterns of optical fibres after being heated at various temperatures and periods. At the latter figure, is presented the spot size which is proportionally related to germanium's profile width. For instance, there is a 2.5 times enlargement of the heated fibre's spot size at 1400°C for 5 hours, compared to the original size [73, 75]. **Figure 14** presents the germanium concentration distribution, in arbitrary units, of an optical fibre's cross sections before and after a 10 hours heat treatment. It was proven that germanium atoms are outwards diffused, from the core to the cladding, during heat treatment experiments [73].

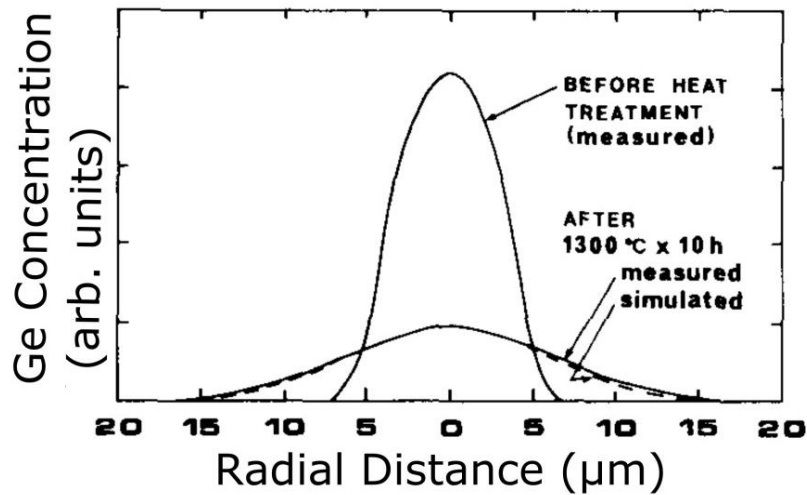


*Figure 14. Measured (dashed) and simulated (solid) germanium concentration distributions after the heat treatment. Ge distribution before the heat treatment is also shown [73].*

**Figure 15** portrays the relationship between the enlarged MFD of a thermally expanded core and its heating time. MFD's enlargement will have an impact on Fabry-Pérot sensor's performance due to tapering phenomena along the optical fibre by dopant's diffusion. Consequently, more modes will be introduced in the thermally expanded region of the optical fibre affecting the phase response of the Fabry-Pérot cavity. A micro burner with a propane/oxygen flame has been used to achieve a local expansion of an optical fibre's core diameter. The heating temperature of the micro burner is not measured during the dopant diffusion. After the dopant begins to diffuse, the MFD starts a rapid expansion following a nearly parabolic behaviour [76].

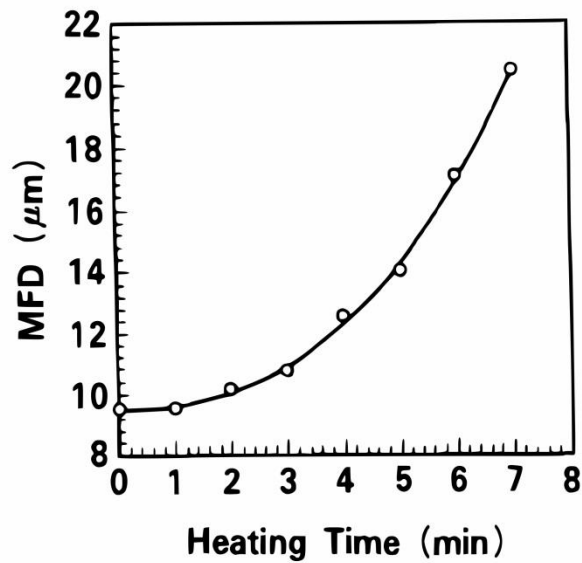


**Figure 15.** Mode field diameter (MFD) of an optical fibre with respect to heating time[75].

Normally, Energy-dispersive X-ray spectroscopy (EDS) technique is used to measure the element concentration before and after diffusion in optical fibres. The same technique has been used in our work. EDS technique records the X-ray spectrum, emitted by a solid sample bombarded with a focused beam of electrons, obtaining a localized quantitative chemical analysis. This determination of the sample's element concentrations, involves measuring line intensities for each element [77].

#### **2.2.2.4 Effects on Optical Fibres during Optical Fibre Drawing**

After the formation of a uniform composition fibre glass there can still be found frozen optical and mechanical changes. These frozen stresses and strains shown huge impact to both mechanical and optical properties of optical fibres [78]. An investigation of germanium (Ge) and fluorine (F) diffusion during silica optical fibres drawing proved that both elements can diffuse at high temperatures (2100°C) at low draw speeds

(10m/min). Theoretical work showed that the most diffusion occurs in the neck-down region [80]. The preform diameter does not significantly affects the diffusion, whereas the draw temperature (**Figure 16**) and preform drawing tension (**Figure 17**) have a significant impact on it causing excess loss at the optical fibre [79, 80]. Additionally, high temperatures and long process time affect the dopant profiles by broadening them [81]. Due to the difference at the viscosities of core and cladding, tension from drawing can induce high residual stress at the core. The residual stress reduces core's refractive index through photo elastic effects. The result is a shift of cut-off wavelength to shorter wavelengths [80].

**Table 1. Parameters of Preforms**

Preform	Core	Cladding	$\Delta(\%)$
1	SiO <sub>2</sub>	F-SiO <sub>2</sub>	0.27 ( $\Delta^-$ )
2	SiO <sub>2</sub>	F-SiO <sub>2</sub>	0.45 ( $\Delta^-$ )
3	GeO <sub>2</sub> -SiO <sub>2</sub>	SiO <sub>2</sub>	0.35

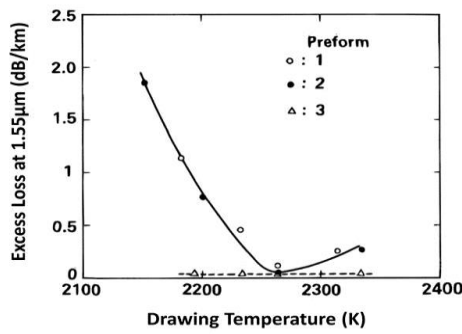


**Figure 16.** Preform types of optical fibres showing the relationship between the excess loss and the drawing temperature [79].

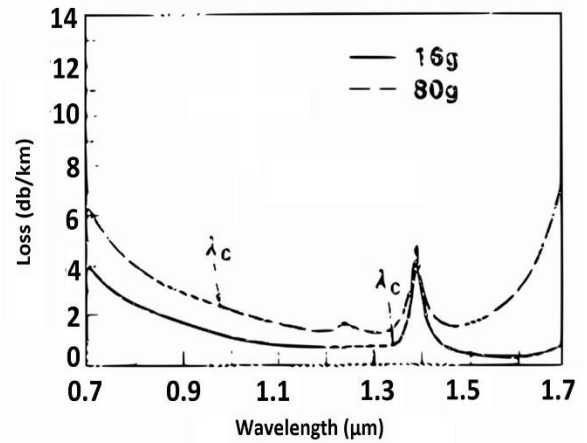


**Figure 17.** Optical loss spectra versus different drawing tensions of an optical fibre (preform 1 of Figure 16) [80].

During drawing, an optical fibre is cooled down from high temperature. Its regions, such as core and cladding, contain different dopant types and concentrations which subsequently will exhibit different thermal expansion coefficients. The different values of thermal expansion coefficient and viscosity between optical fibre's regions can raise thermal stress effects. This results to different thermal contraction to some regions of the optical fibre than to others. At room temperature, the unstrained dimensions of the core diameter of an optical fibre will be marginally inconsistent with the unstrained dimensions of fibre's cladding inner diameter. Strain is required to maintain geometric continuity between these fibre regions rising residual elastic stresses. Draw-induced mechanical effects and thermal stresses are the main reasons that cause the residual elastic stresses and strains [79].

### ***2.2.2.5 Summary of High Temperature Effect on Optical Fibres***

Optical fibre's material, fused silica ( $\text{SiO}_2$ ), proved to have a variety of advantages at high temperatures. On the other hand, especially above  $1100^\circ\text{C}$ , optical fibre starts showing several effects that affect its performance. Above that temperature the viscosity of fused silica decreases, going through its phase transition point which sits at  $1250^\circ\text{C}$  and reaching to its softening point at above  $1650^\circ\text{C}$ . Fused silica material will not liquify at that high temperatures but it will become softer. In addition, heating an optical fibre at temperatures above  $1100^\circ\text{C}$  showed diffusion of its dopant to other regions of the optical fibre, from core to cladding and vice versa depending on the type of the optical fibre. Optical fibre drawing is a common method of manufacturing an optical fibre at which fused silica glass is heated at  $2100^\circ\text{C}$  where uniform composition fibre glass can be formed. After its formation, frozen optical and mechanical changes, such as stresses and strains, in optical fibre's material can be found. Working with optical fibres at such high temperatures consideration of these phenomena must be taken as both mechanical and optical properties of optical fibres are highly affected. The impact of high temperatures, through these phenomena, could be errors and drifts at the measured travelling signal (phase, intensity, polarization) in the optical fibre or at the worst-case scenario mechanical corrosion of the optical fibre itself.

## **2.3 Optical Fibre Sensors (OFS)**

Established high temperature sensing techniques, often based on electrical sensors, are used extensively throughout many industries. Optical fibre sensors proved to be capable to detect and quantify a variety of quantities such as temperature [82], pressure [83], refractive indices [84], vibrations [85], displacements [86], rotations or concentration of chemical species. However, optical fibre sensors tend to be fused when the sensing requirements cannot be met by conventional sensing technologies. The advantages that make optical fibre sensors competitive with conventional sensors include: small physical size, electrical passivity, immunity to electromagnetic interference, potential of long distance remote operation, potential high bandwidth operation, a potentially high spatial sensing resolution, and also the potential of multiplexing an amount of sensors along a single optical fibre [32].

Intensity, phase, frequency, and polarization are some of the parameters that characterize light. Any one of these parameters can experience changes under environmental perturbations. Fibre optic sensors exploit the change of these

characteristics measuring their magnitudes or modulations and quantifying the environmental variation. A sensor can be characterized as phase, intensity, frequency, or a polarization sensor depending on the modulated parameter. Depending on the measurand's application of the optical fibre sensor, it can be categorized in physical sensor (temperature, strain), biomedical sensor (flow of organic contents), chemical sensor (pH content, gas analysis, spectroscopic study) [87].

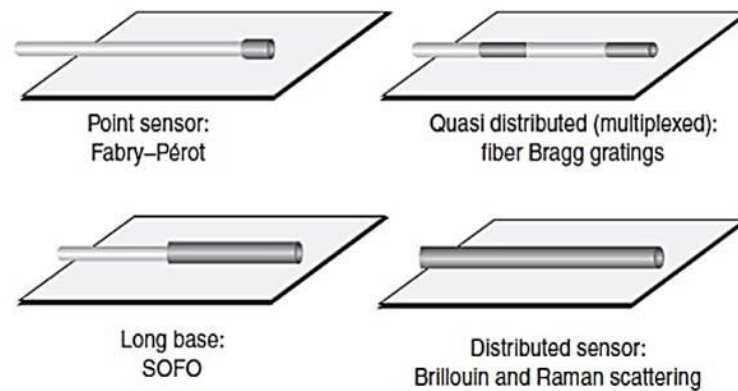


**Figure 18.** *Types of optical fibre sensors.*

Optical fibre sensors can be categorized according to their measurement points. **Figure 18** shows the most common categories which are the point sensors, distributed sensors, long base sensors, and multiplex sensors distributed sensors. At the point sensors, at which this thesis is focused on, a single measurement point at the end of the optical fibre is the sensing element. Multiplexed sensors can measure along numerous points using a only one optical fibre and distributed sensors can sense at any point on the same optical fibre, on a length scale up to kilometres [88]. For this thesis experiments, they have been extensively used Fabry-Pérot point sensors which have a single measurement point at the end of the fibre.

Optical fibre sensors are separated in two categories, shown in **Figure 19**, depending on the use of optical fibre itself. Fibre optic sensors which use the optical fibre as a transmitting medium of sensor's signal are called extrinsic sensors (**Figure 19(A)**). In specific, the optical fibre is used as information transporter leading up to a sensing device, which operates as a sensor, and the optical fibre waveguides the light beam that propagates to a distant receiver. In the sensing device are placed mechanisms such as mirrors, a gas cell or a cantilevered arm that can control or transform a light beam [87].

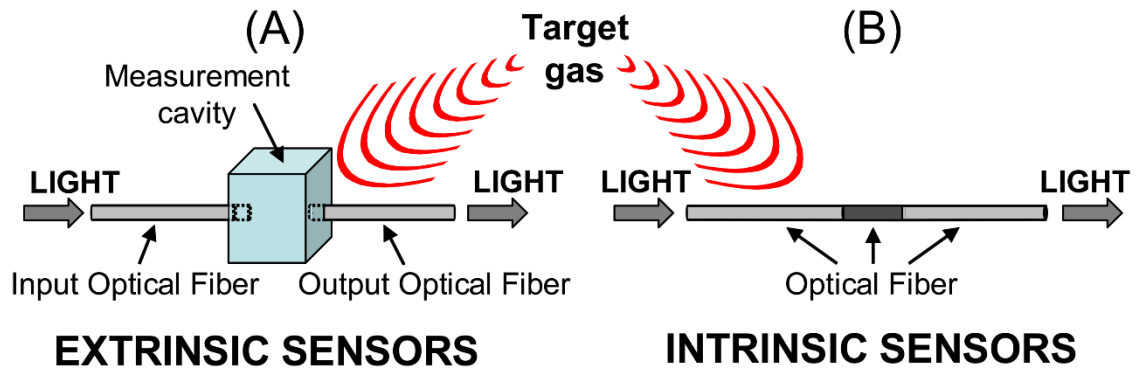


**Figure 19.** Extrinsic (A) and intrinsic (B) optical fibre sensor configurations for gas detection [89].

On the other hand, when the optical fibre itself is the sensing element of the sensor, then these sensors are called intrinsic (**Figure 19(B)**). In intrinsic sensing, the environmental perturbation is converted to a light signal modulation which travels through the optical fibre. This light modulation depends on the optical properties of the optical fibre and it can be as phase, intensity, or polarization. Special design of the optical fibre sensor with respect to the nature of the environmental measurands, is acquired. Hence, only the desired environmental effect is will be sensed [87].

### 2.3.1 Temperature Sensing with Optical Fibre Sensors (OFS)

Despite the various sensing abilities of Fabry-Pérot sensors, in this work is being examined the temperature sensing in harsh environments. Temperature measurement is characteristically useful for long-term health assessments of civil structures, geostructures, and aerospace structures [88, 90, 91]. Numerous different optical fibre sensor techniques have been demonstrated for temperature measurement, such as fibre Bragg grating (FBG) sensors [92], Rayleigh, Brillouin or Raman scattering based sensors [93, 94], and intrinsic or extrinsic Fabry-Pérot (F-P) fibre-optic sensors [31, 82, 86, 95-98].

Fibre optic temperature sensors are proved to be more advantageous than electrical based temperature sensors such as thermocouples, thermistors, as they proved to be immune to electromagnetic interference and suitable for remote controlling as the sensor head is located far away from the signal processing electronics [97, 98]. Temperature measurement is a well-established field of research with great interest in temperature sensing in ranges starting from a few degrees up to thousands degrees of Celsius (°C) [96].



In a recent publications, such as [29], is referred a fibre-optic temperature sensor made by sapphire fibre which was tested up to 1600°C and being perfectly reproducible. The turn of interesting to single crystal optical fibres, like sapphire fibre, was caused by fused silica fibre's mechanical strength degradation and germanium dopant's diffusion at temperatures above 1000°C [70, 83].

### **2.3.2 Interferometer Theory of Fabry-Pérot OFS**

In 1897, two physicists Alfred Pérot and Charles Fabry published an article which was describing their noteworthy invention, the Fabry-Pérot interferometer (F-PI) [85]. Fabry-Pérot (F-P) interferometric sensors are characterized by precision, simplicity, versatility, high responsivity, and immunity to ambient noise. The usual fabrication method of Fabry-Pérot type sensors is by using air to glass reflectors, inscribed Bragg gratings into the fibre, or through semi reflective splices. Interferometry is most commonly used for sensing on the optical fibres such as Mach-Zender and Sagnac sensors [99]. However, as it was abovementioned, this work is particularly focused in Fabry-Pérot interferometers (F-PIs) which became a versatile tool for monitoring various biological, physical, and chemical parameters due to their compact size and simple design as well as they proved to be highly sensitive [100].

In-fibre air-cavity-based F-P sensors have been used to make sensors insensitive to temperature for monitoring refractive index (RI) [18, 101, 102], liquid level [18, 103], strain [92, 104] and hydrogen exposure [105]. However, there are many difficulties in fabrication, due to the time consumable splicing and cleaving processes that have limited their commercial growth.

Fabry-Pérot optical fibre interferometers exhibit extreme sensitivity to ambient variations that can disturb the optical path length between the two mirrors. The sensing region can be very small comparable to a point transducer in some applications. Compared to other optical fibre sensor interferometers (Mach-Zehnder, Michelson, and Sagnac), the Fabry-Pérot does not consist of couplers which can complicate the deployment of the sensor and the interpretation of data. The in-fibre Fabry-Pérot sensor can be ideal for many smart structures sensing applications, even for those applications which need the sensor embedded in a composite or metal material [35, 82, 106].

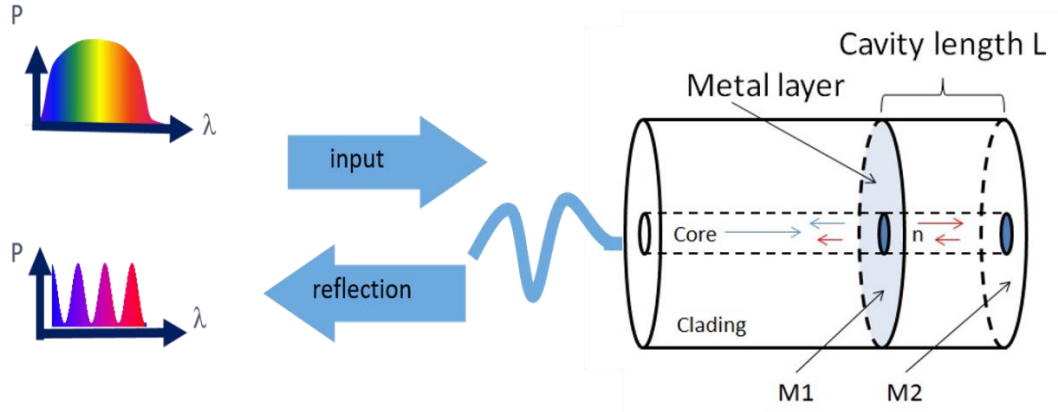


**Figure 20.** Schematic representation of an in-fibre Fabry-Pérot sensor. The input and output spectrum is presented. In addition, the mirrors  $M_1$  and  $M_2$  which create the sinusoidal signal are also displayed.

The reflectance of each interface is given by **Equation 12**:

$$R_1 = \left( \frac{n_1 - n_3}{n_1 + n_3} \right)^2, \quad R_2 = \left( \frac{n_1 - n_2}{n_1 + n_2} \right)^2 \quad \text{Equation 12}$$

where  $n_1$ ,  $n_2$  and  $n_3$  are the refractive indices of core fused silica, air, and chromium layer, respectively. When the cavity length changes, a phase shift is produced which causes an intensity change of the reflected (or transmitted) optical power at any given wavelength. Both the chromium metallic layer and fibre's end partially reflect the launched light. Consequently, a reflected sinusoidal spectrum (**Figure 20**) of the in-fibre F-P cavity is recorded and depended on cavity's optical path length. A characteristic of the sinusoidal interferogram is its fringe visibility given by **Equation 13**.

$$V = \frac{I_{max} - I_{min}}{I_{max} + I_{min}} \quad \text{Equation 13}$$

Fringe visibility depends on sensor's manufacturing, such as thickness of the chromium layer during sputtering, the perpendicular angle of the cleaved end-face and the coupling loss, of the recoupling light from the second mirror into the core, due to misalignment between the spliced fibres. In general, from a high fringe visibility a larger signal-to-noise-ratio (SNR) and better measurement accuracy is obtained [107].

The interference can be approximately explained as two-beam interference. For higher accuracy measurements, the two-beam interference technique includes errors such as fringe asymmetry of the cosine transfer function arising from optical losses due to intrinsic absorption or scattering at the internal thin chromium mirror. The phase recovery of in-fibre Fabry-Pérot sensor proved to be dependent on these systematic errors. Accurate non-linear least square fitting demodulation analysis can significantly

reduce these errors [108]. The reflectance's expression for a lossless Fabry-Pérot cavity is presented in **Equation 14**.

$$R_{FP}(\lambda) = \frac{P_r}{P_i} = \frac{R_1 + R_2 + 2\sqrt{R_1 R_2} \cos \varphi}{1 + R_1 R_2 + 2\sqrt{R_1 R_2} \cos \varphi} \quad \text{Equation 14}$$

In **Equation 14** the parameter  $R_1$  signifies thin metallic layer's ( $M_1$ ) reflectance,  $R_2$  signifies fibre end's ( $M_2$ ) reflectance and  $\varphi$  is the round-trip propagation phase shift in the F-P cavity. Both  $M_1$  and  $M_2$  mirrors are presented in **Figure 20**.

The output interference spectrum given by **Equation 14** shows maximum and minimum values at different wavelengths. **Equation 15** calculates the wavelengths at which interference maxima or minima occur, at which  $\lambda_{min}$  is the wavelength where  $R_{FP}(\lambda_{min})$  is minimum and  $m$  is the  $m^{\text{th}}$ -order interference fringe. A change at the temperature environment will cause a change at both optical fibre's cavity length and refractive index, and can be distinguished by a shift of  $\lambda_{min}$ .

$$\frac{4\pi nL}{\lambda_{min}} = 2m\pi \rightarrow \lambda_{min} = \frac{2nL}{m} \quad \text{Equation 15}$$

Both phase value  $\varphi$  and optical phase shift value  $\Delta\varphi$ , are presented with respect to temperature by **Equation 16** and **Equation 17**, respectively [109]. The optical cavity length is related to temperature change and light's wavelength ( $L \propto T \propto 1/\lambda$ ).

$$\varphi = \frac{4\pi nL}{\lambda} \quad \text{Equation 16}$$

$$\Delta\varphi = \frac{4\pi nL}{\lambda} \left[ \frac{1}{n} \frac{dn}{dT} + \frac{1}{L} \frac{dL}{dT} \right] \Delta T \quad \text{Equation 17}$$

Concerning **Equation 16** and **Equation 17**, it has to be noticed that  $n$  is the core refractive index of the cavity fibre,  $L$  is the cavity length,  $\frac{dn}{dT}$  is the thermo-optic coefficient with typical value for fused silica glass  $8.6 \cdot 10^{-6} \text{K}^{-1}$  and  $\frac{dL}{dT}$  is the thermal expansion coefficient with typical value for fused silica glass  $0.55 \cdot 10^{-6} \text{K}^{-1}$  of silica fibre, respectively [109]. In **Equation 17**, the factor  $\frac{4\pi nL}{\lambda} \left[ \frac{1}{n} \frac{dn}{dT} + \frac{1}{L} \frac{dL}{dT} \right]$  represents the sensitivity of the sensor. The output intensity of light that is launched in the fibre is given by **Equation 18** which is quoted below

$$I = I_1 + I_2 + 2\sqrt{I_1 I_2} \cos\left(\frac{4\pi n_{eff} L}{\lambda}\right)$$

Equation 18

In the latter equation,  $I_1$  and  $I_2$  represent the intensities of the two interfering beams,  $n_{eff}$  is the effective refractive index of the guided mode in the fibre (a typical value is 1.444 for pure silica at 1550nm), and  $\lambda$  is the free-space optical wavelength.

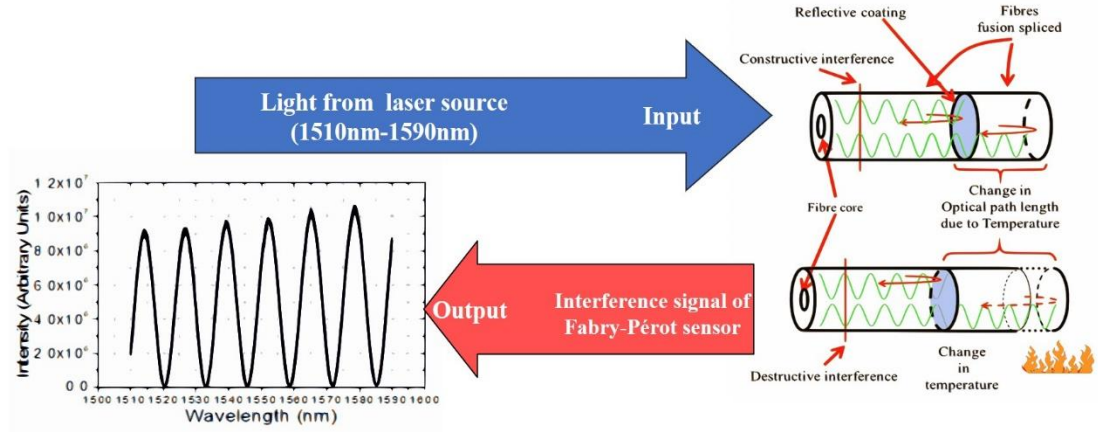


**Figure 21.** Schematic representation of Fabry-Pérot sensor functionality. On the right side of the graph it can be seen the optical path change (OPD) due to temperature increase. This change leads to a wavelength shift and periodicity change at the sinusoidal signal. The destructive and constructive interference is also displayed with a red vertical line. On the left, the laser light source input and the sinusoidal signal output are both presented.

**Figure 21** shows the input intensity of the launched signal traveling along the fibre and being partially reflected by the first and second mirror, creating a sinusoidal signal through constructive and destructive interference. Increasing the temperature by  $\Delta T$  at the surrounded environment of the sensor, is caused a change at both physical length and optical path length of the sensor. The parameter that suffers by the maximum change is the optical length, rather than the physical length, because of the higher value of the thermo-optic coefficient over the thermal-expansion coefficient. The difference between two paths in the optical fibre is called the optical path difference (OPD). Optical path length determines the phase of the light and rules the interference and diffraction of light as it propagates.

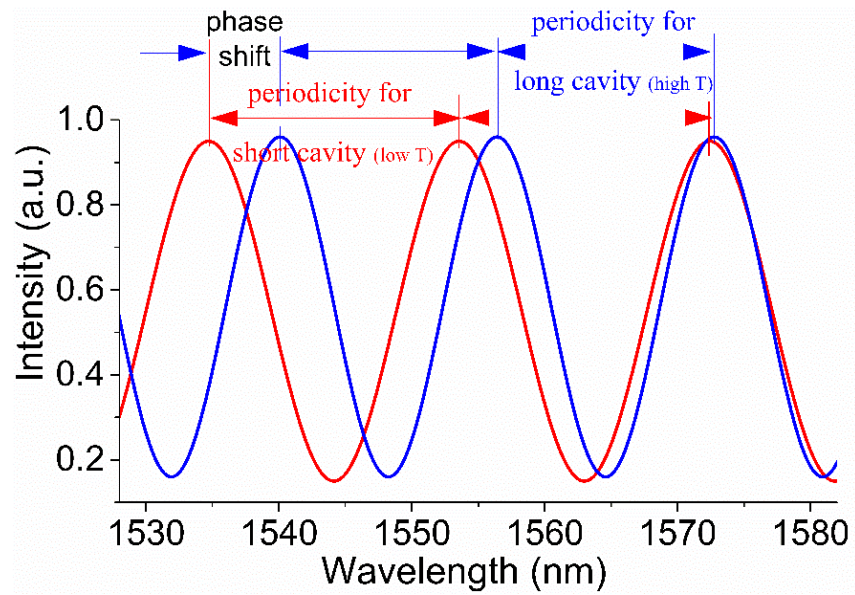


**Figure 22.** Phase shift and change of periodicity for low (red line data) and high (blue line data) temperature changes. It can be seen the phase shift for each wavelength peak/valley is not constant, due to periodicity change.

The increase of the environmental temperature of the sensor causes two most important changes which are a change at the periodicity of the fringes and a phase shift. Data analysis routine can record each peak/valley wavelength value of the sinusoidal spectrum. **Figure 22** demonstrates the effect of temperature increase to Fabry-Pérot sensor's spectrum. The rise of the environmental temperature increases the optical length. Hence, the periodicity of the spectrum tends to spread while the phase shifts to lower wavelengths. Also, when the temperature decreases the optical length shortens, the periodicity starts decreasing and the phase shifts to higher wavelengths. **Figure 23** depicts the spectra of a 70 $\mu$ m Fabry-Pérot sensor at room temperature and at 300°C. Both spectra emanate from the theoretical calculation model built on LabVIEW software. The temperature change caused a shift of approximately 4nm in wavelength and 1.755 radians in phase.

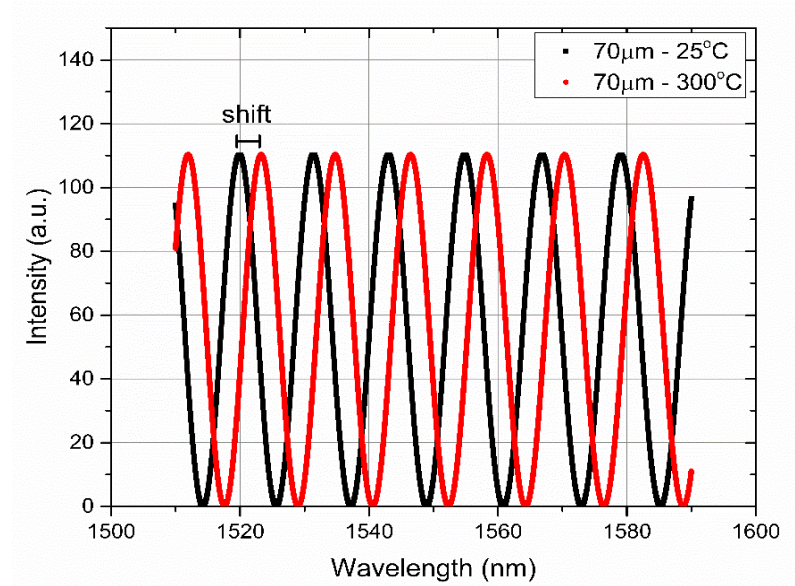


**Figure 23.** Spectra comparison of a 70 $\mu$ m Fabry-Pérot sensor at two different temperatures. The black data correspond to 25°C and the red data to 300°C. The shift of the spectrum due to temperature change is also indicated.

### 2.3.3 Interrogation Data Analysis Routine on LabVIEW Software

The data monitoring and extraction of the sensor temperature contains many stages of data manipulation. **Figure 24** and **Figure 25** demonstrate schematically the complete LabVIEW code for each step. During data analysis routine (**Figure 24**) an equal stepped spectrum in the wavelength domain is converted to an interpolated, equal stepped spectrum in the optical frequency domain. This is essential for an FFT transform.

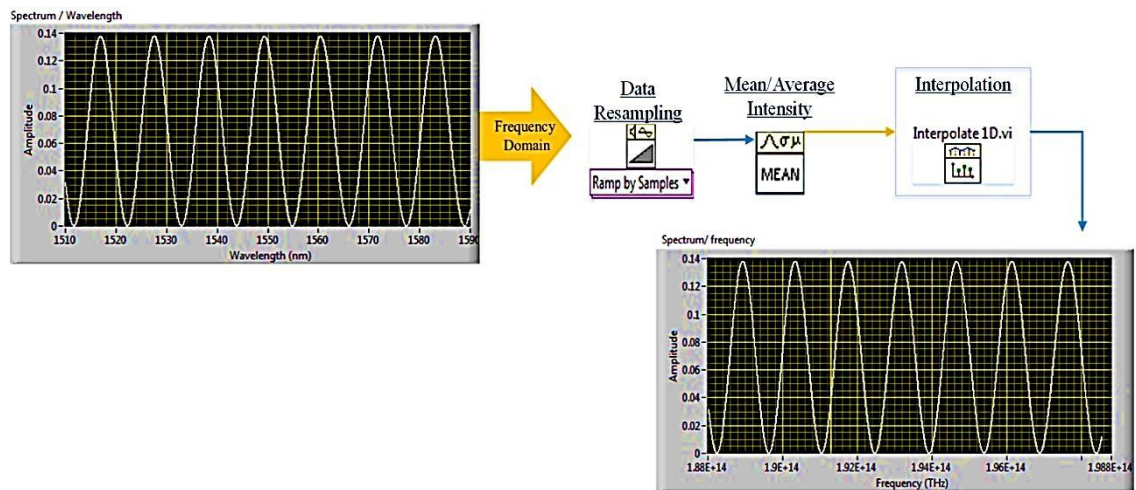


**Figure 24.** Transition from wavelength domain to frequency domain including data resampling, interpolation, and spectrum intensity averaging.

The original data are recorded in the wavelength domain with a 5pm wavelength interval. After their conversion to the frequency domain, the frequency interval between each data point is not uniformly spaced, due to the inverse proportional dependency between the wavelength and the frequency. Consequently, it's necessary to resample the signal with an appropriate sampling rate in order to reconstruct the interferogram in the frequency domain.

In more details, 16000 data points are distributed in a wavelength span of 80nm, from 1510nm to 1590nm with a sampling spacing of 5pm. After conversion from wavelength domain, the frequency domain spectrum will start from 188.548THz up to 199.548THz. The frequency span is 10THz in which are distributed not equally spaced 16000 data points. Reducing the sampling spacing, the error made by the spectrum's transition to frequency domain will be reduced and thus the original spectrum is well reconstructed. The data interpolation of the spectrum at the frequency domain is used to add necessary data points to extract the single tone with an improved accuracy. Interpolating with 80000 data points, the sampling spacing has been reduced by 5 times increasing the reconstruction accuracy of the sinusoidal spectrum. More than 80000 data points can be added during interpolation, but the memory space of the computer runs out above 160000 data points and limits the interpolation process. "Cubic spline" interpolation proved to minimize the interpolation error, and the associated interpolation error shows insignificant impact on the final output [110]. At this point the spectrum has been resampled and interpolated with 80000 data points which are distributed equally spaced in frequency domain for FFT single tone extraction.

Hence, the transpose from wavelength to frequency domain will retain the equally spacing between the data points through data resampling and interpolation. Nyquist frequency defines the maximum detectable frequency. To recover all Fourier components from the sinusoid signal, it is essential the sampling rate to be at least twice the highest waveform frequency. The highest frequency that can be coded at a specified sampling rate and can fully reconstruct the signal is called Nyquist frequency [111]. The lack of this condition's implementation will end up to aliasing, where an uneven sampling of data will detect low frequencies as well.



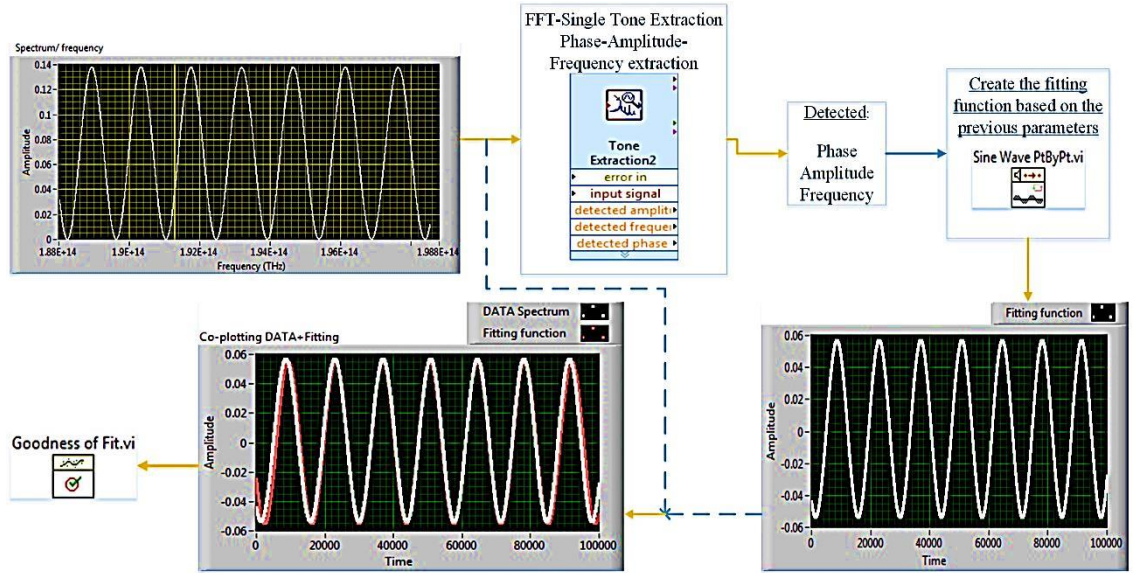


**Figure 25.** Single tone extraction and fitted sinusoidal reconstruction based on amplitude, phase, and frequency. At the bottom left of the graph, both fitting signal and data signal are co-plotted from which the goodness of fit ( $R^2$ ) can be estimated.

**Figure 25** demonstrates the data sequence after their conversion to frequency domain. The sequence consists of a FFT analysis to the frequency domain spectrum which determines the fundamental frequency of the optical periodicity. Additionally, the phase and the amplitude of the spectrum are extracted. From the extracted values of phase, amplitude, and frequency a non-linear least square fitting of a sinusoidal function is applied to the data of the spectrum. Consequently, the goodness of the fitting ( $R^2$ ) can be estimated. **Figure 26** presents the LabVIEW code from which the change of the periodicity calculates the Fabry-Pérot cavity length.

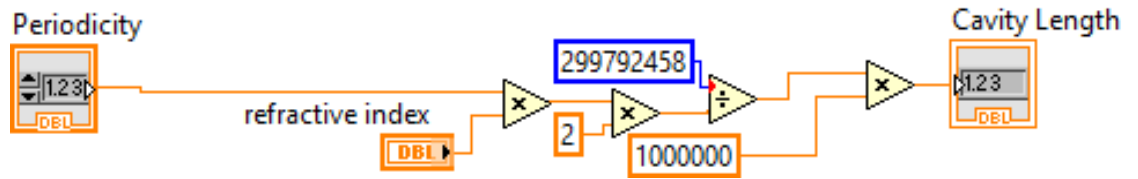


**Figure 26.** Cavity length determination through periodicity.

The wavelength shift of each peak/valley offers information on the temperature change of the environment. Its advantage is that intensity variations by the optical source instabilities cannot affect the wavelength peak detection. Additionally, wavelength detection doesn't need complicated mathematical demodulation analysis. However, due to the change at the periodicity of the spectrum, each peak/valley will have a different wavelength shift. Also, the actual peak/valley position of an interfered signal into the fundamental one, will diverge from the real peak/valley wavelength adding an error to wavelength detection. A FFT interrogation algorithm can eliminate the above-mentioned problems, improving the demodulation accuracy significantly. A



convoluted signal consisted of two or more sinusoidal signals can easily be demodulated with a FFT algorithm (**Figure 27**). The algorithm will extract the fundamental frequencies of the signals that construct the convoluted signal. Also, the application of a FFT on the sinusoid signal exploits the 16000 data points of the spectrum in total, while at the same time there is no signal distortion due to the spectrum fluctuation. The accuracy of the calculated FFT frequency peak can be enhanced by increasing the FFT sampling number [112].

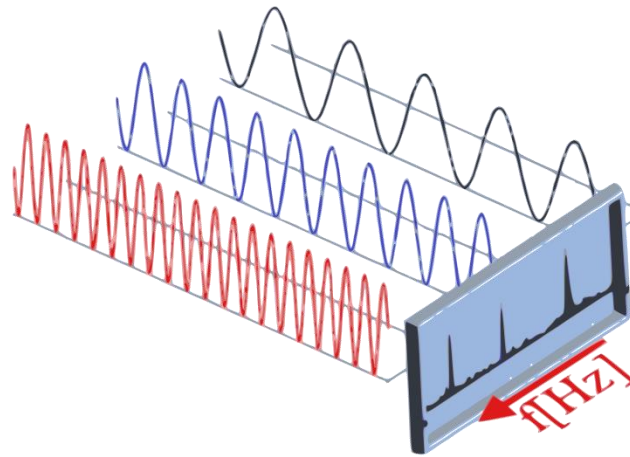


**Figure 27.** *Fundamental frequency detection after FFT is applied to multiple or convoluted signals.*

Wide temperature range and variable starting phase of the sensors is detected because of the high sensitivity, leading to phase ambiguity. More specifically, several phase values represent two or more different temperature values. For example, a Fabry-Pérot sensor with a  $60\mu\text{m}$  cavity has phase value of 0.54radians at  $50^\circ\text{C}$ , where the same phase value corresponds to  $974^\circ\text{C}$  as well. The phase must be unwrapped in order to distinguish the exact phase value for each temperature in a temperature range up to  $1000^\circ\text{C}$ . Counting on only the phase shift, the information for the correspondent temperature is inadequate. Including the unique optical periodicity (frequency extraction) of the spectrum, combined with the phase shift, at each temperature the accurate temperature extraction can be achieved. For longer cavities the same phase values can represent three temperature where a phase value of 0.51radians, for a  $150\mu\text{m}$  cavity length, corresponds to  $40^\circ\text{C}$ ,  $467^\circ\text{C}$  and  $820^\circ\text{C}$ . The optical periodicity of the sensor signal is unique for each temperature value and can be used to eliminate the  $2\pi$  phase uncertainty. Hence, a combination function of periodicity and phase is used for an unambiguous temperature determination.

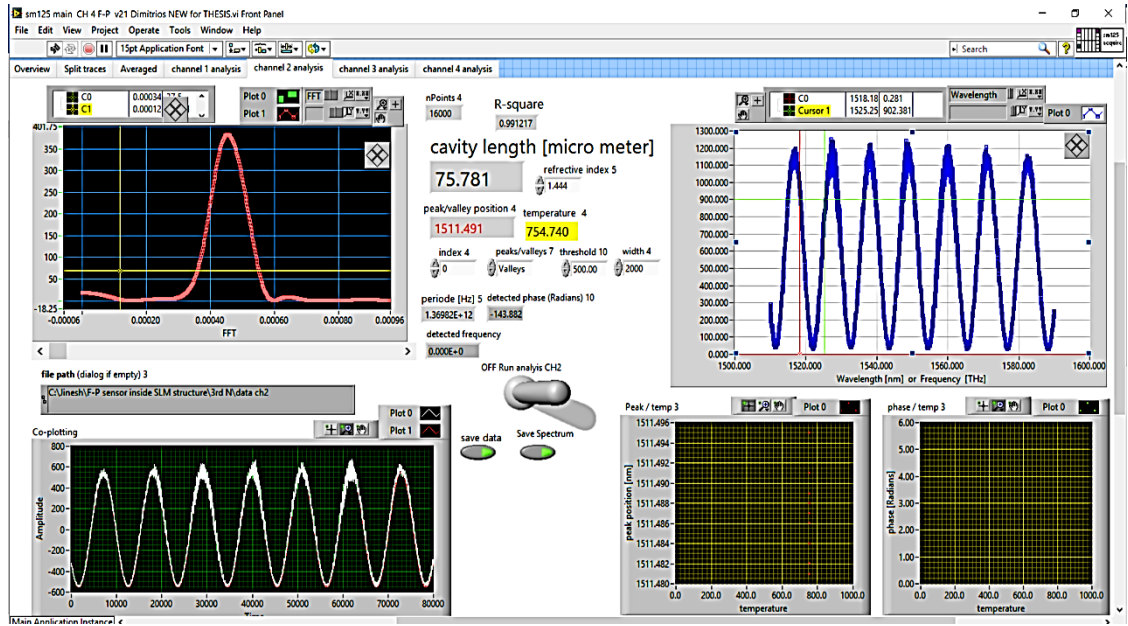


**Figure 28.** LabVIEW front panel for real-time interrogation of a Fabry-Pérot optical fibre sensor.

In addition, in **Figure 28** the LabVIEW interrogation software front panel for real-time interrogation is presented. At the top of the panel, both wavelength domain sinusoidal signal (right side) and the single tone frequency display (left side) are clearly shown. At the centre of the panel, cavity length ( $\mu\text{m}$ ), the valley wavelength of the sinusoid and the independent thermocouple temperature recording are displayed. Several adjustable parameters are added at the interface for practical view of useful information, as well. Spectra's fundamental frequency and phase shift of the sinusoidal fitting are extracted from data at real time. Due to the temperature variation of the furnace, a thermocouple is used for an independent temperature monitoring from the sensors.

## 2.4 Experimental Setup

**Figure 29** portrays the experimental setup that was used for conducting the phase stability experiments. The experiment setup consists of a high temperature furnace (Nabertherm RD 30/200/11), a type-N thermocouple, a high precision thermometer (PREMA Precision Thermometer 3040), a Micron Optics interrogation system, a LabVIEW software installed to our computer and finally a Fabry-Pérot (F-P) optical fibre sensor sitting in the furnace.

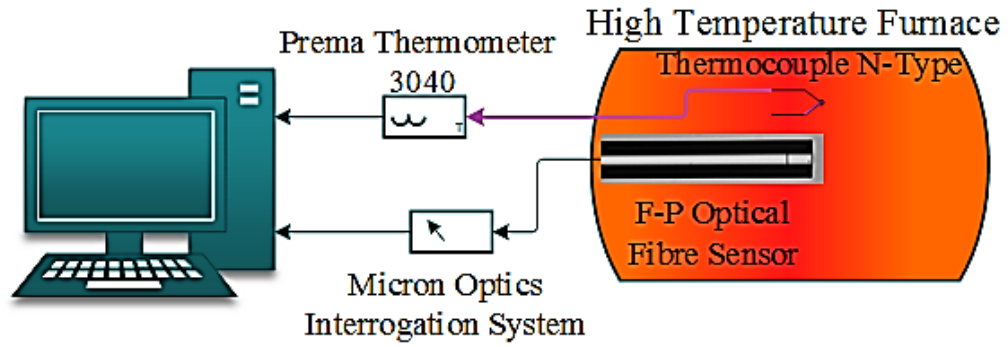


**Figure 29.** Experimental setup for thermal response investigation of the F-P sensors. The LabVIEW PC which is connected to the thermometer and the interrogation system is presented. In addition, the furnace with the optical fibre Fabry-Pérot (F-P) sensor and the thermocouple sitting in it are also displayed.

**Figure 30** shows four optical fibre Fabry-Pérot (F-P) sensors placed in small fused silica tubes, with a thermocouple sitting between them. This setup is ready for introduction in the furnace for stability tests. The sensors are connected, to the interrogation system which launches light from a swept laser source (1510nm-1590nm, sm125 Micron Optics). A LabVIEW software routine, installed on a Lab PC, collects the data, and analyses them. The thermocouple sits in the same longitudinal position with the sensors at a ~2mm transverse distance from the sensors' tip. The thermocouple is connected to a high precision thermometer (PREMA Precision Thermometer 3040) which consequently records the temperature of the furnace's environment, independently from the sensors, through LabVIEW software. In that way, it will record the environmental temperature at which the sensors are subjected to.



**Figure 30.** Experimental setup of four intrinsic Fabry-Pérot optical fibre sensors placed in fused silica tubes. A type N thermocouple sits at the centre. The setup is ready for introduction in furnace for long-term stability tests.

The thermometer, is connected to a resistance temperature detector (RTD). The RTD monitors the room temperature from which the thermometer uses as a cold junction and calculates the differential temperature. A resistance temperature thermometer (RTD) can measure temperature very accurately and effectively. An

accuracy better than  $0.01^{\circ}\text{C}$  can be achieved with a Pt100 RTD can, between temperature values of  $-200^{\circ}\text{C}$  and  $580^{\circ}\text{C}$ . The metallic elements of a RTD are characterized from a specific resistance, which is proportionally related to a temperature change. A change at the temperature environment causes a resistance variation the metallic elements. Moreover, this resistance change creates a small current, which passing across the metallic elements generates a small voltage [113].

## 2.5 Thermocouples (TCs)

Thermocouples are simple designed devices which, the most advanced of them, can measure temperatures up to  $2320^{\circ}\text{C}$  [114]. Some of their characteristics which make them preferable are that they there is a large variety of inexpensive and durable thermocouples for temperature measuring up to  $1400^{\circ}\text{C}$ . Thermocouples (TCs) consist of two different metals and can sense temperature changes in a variety of processes [115].

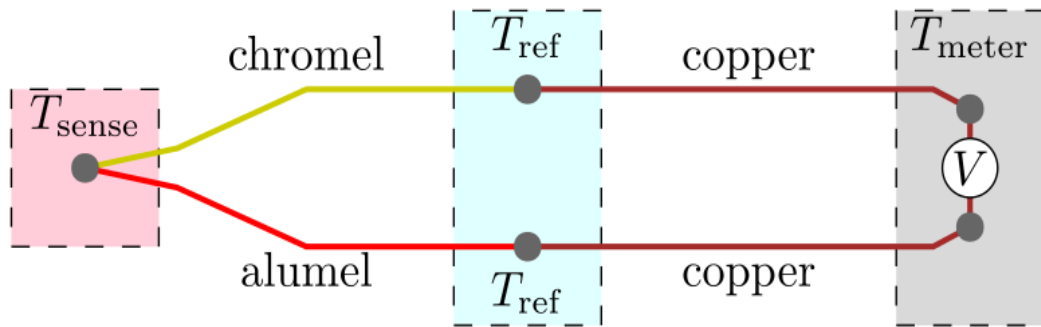


**Figure 31.** Thermocouple circuit type-K thermocouple including all three block temperatures. The block temperatures are the sensed, the reference and metered temperature[116].

**Figure 31** portrays a thermocouple which is formed by two wires of different electrically-conductive materials. A junction is created from the welding of these dissimilar metallic wires, playing the role of the sensing element [117]. When the thermocouple's junction experiences a change in temperature, a voltage is created (Seebeck voltage). This voltage can then be interpreted in temperature based on reference tables of each type of thermocouple. Nevertheless, a reference junction is necessary to make an absolute temperature measurements as thermocouples can indicate temperature difference between junctions [115, 117, 118].

### 2.5.1 Annealing of Thermocouples - Hysteresis

To establish stability over a temperature range, thermodynamic equilibrium should be maintained in the thermocouples. Annealing eliminates existing non-equilibrium states such as strains introduced by cold working. Suitable stabilization cycles can achieve improvement of the reproducibility, even though a sufficient heat treatment is given by the producer [119, 120].

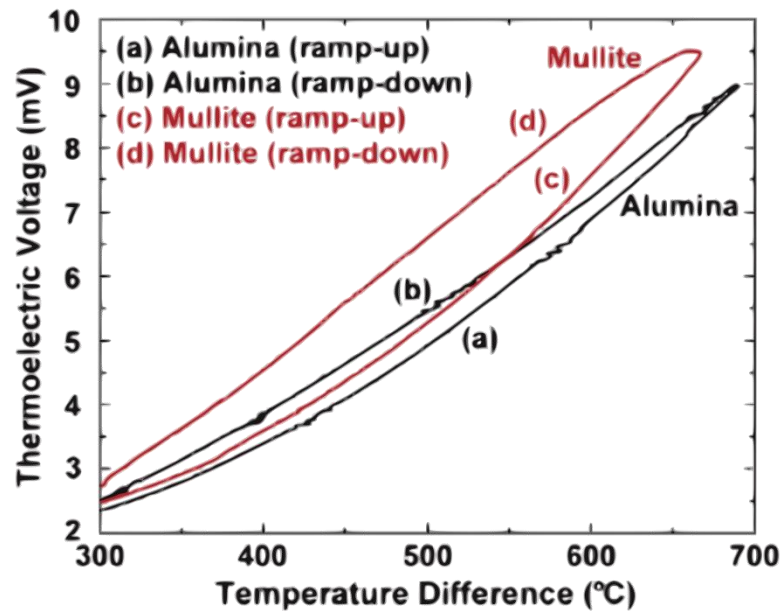


**Figure 32.** Hysteresis upon heating/cooling of Pt/Pd thermocouples on alumina and mullite [121].

Hysteresis is a condition where temperature reading appears to have a “memory” effect as the thermometer is moved through a sequence of temperatures. For metal based thermocouples, hysteresis exhibits a main problem which is the temperature indication during heating is different from the indication during cooling (**Figure 32**). Literature review suggests that the hysteresis effects in Type K alloys occur at temperatures between 200°C and 600°C and in Type N alloys this effect occurs at a temperature range of 200°C to 1000°C [120].

### 2.5.2 Type-K and Type-N Thermocouples

Type-K thermocouples are considered one of the most preferable thermocouples to use at temperature measuring for basic laboratory work. In the beginning of our experiments we used a type K thermocouple. Type K thermocouples are recommended for use in an oxidizing (should be used a protection tube) or completely inert

atmosphere for temperatures starting from  $-200^{\circ}\text{C}$  up to  $1300^{\circ}\text{C}$  [122, 123]. Type K thermocouples are suitable for use without rapid aging up to  $1260^{\circ}\text{C}$ , in a non-oxidizing atmosphere. In oxidizing high temperature environments, the chromium wire starts to corrode and becomes magnetic, especially between  $800^{\circ}\text{C}$  -  $1050^{\circ}\text{C}$ , causing a permanent degradation of the thermocouple and the outcome is a very low reading of the thermocouple when the corroded region is exposed to thermal gradient. Hence, type K thermocouple experiences a cumulative drift after a period at temperatures above  $900^{\circ}\text{C}$ . The type K thermocouple's inherent composition allows for internal oxidation as well as external oxidation. This internal oxidation will eventually cause the thermocouple to decalibrate [124].

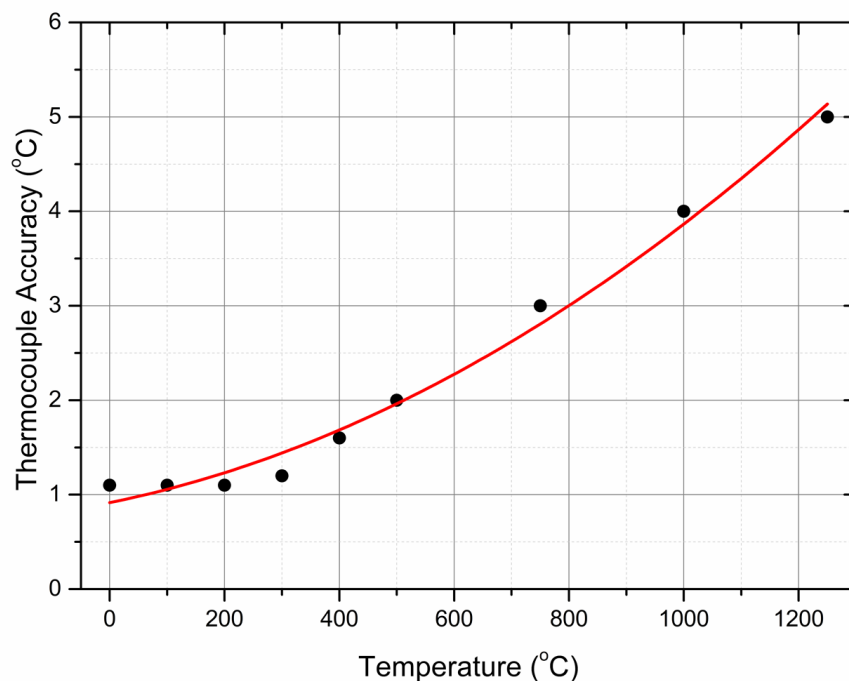


**Figure 33. Accuracy of N type thermocouple up to 1200 Celsius degrees. Each accuracy data point represents the  $\pm^{\circ}\text{C}$  at a given temperature. This figure was created from the accuracy datasheet of a type N thermocouple[115].**

The N-type thermocouple is slightly more expensive and it has better repeatability between  $300^{\circ}\text{C}$  to  $500^{\circ}\text{C}$  compared to the type K. In addition, it consists by Nicrosil and Nisil alloys, which show significantly improved thermoelectric stability compared to other standard base-metal thermocouple alloys. The composition of its alloys give at type N thermocouples the ability to practically eliminate or essentially reduce the causes of thermoelectric instability [125]. The type N thermocouple can be functional at a maximum continuous operating temperature of  $1260^{\circ}\text{C}$  [115], and can resist better to oxidation at high temperatures rather than type K.

## 2.6 Summary of Chapter 2

In this chapter the background of optical fibres and intrinsic Fabry-Pérot optical fibre sensors was presented. A brief description of their functionality principles and material optical properties was also demonstrated. Fabry-Pérot optical fibre sensor's sinusoidal signal is created by the constructive and destructive interference signals reflected by two reflective mirrors separated by a distance ( $L$ ). A change in the environmental temperature where the Fabry-Pérot sensor is placed can be detected by the change in the sinusoidal spectrum. The interrogation data analysis, using LabVIEW software, for data interpretation was described in this chapter. Using a data analysis routine, the phase and the fundamental frequency of the sinusoidal spectrum are extracted. The combination of phase and frequency correspond to a specific temperature at the surrounding of the sensor. The phase of Fabry-Pérot signal is correlated with the refractive index of the travelling mode in the optical fibre. A change on the surrounding temperature has an impact on the refractive index of the core, on which the signal is waveguided. Hence, a temperature change will alter the core refractive index and consequently the phase of the sinusoidal signal.

The low thermo-optic and thermal expansion coefficients of optical fibre's material (fused silica-SiO<sub>2</sub>) make optical fibres suitable for high temperature sensors. In addition, the high temperature annealing, softening, and melting point of fused silica (>1100°C) make them suitable candidates for temperature sensing up to 1100°C. High temperature optical fibre sensors are the main interest of this thesis, so temperature's impact on optical fibre's material has been reviewed. According to literature review, above that temperature optical fibre starts experiencing non-reversible phenomena such as dopant diffusion from core towards cladding or vice versa which affect the optical fibre sensor's performance. Dopant diffusion can occur at temperatures even lower than 1000°C but in slower diffusion rate. At 1250°C sits the phase transition point of fused silica, at which alterations on the density and viscosity of the material can occur affecting the performance of Fabry-Pérot sensor. These phenomena should be considered for optical fibre temperature sensing above 1100°C, as they proved to put limitations on optical fibre sensor's functionality.



## Chapter 3: Manufacturing process of Fabry-Pérot sensors

### 3.1 Introduction

This chapter will present step by step the manufacturing process of building an intrinsic optical fibre Fabry-Pérot sensor. A short description of the manufacturing process of an intrinsic Fabry-Pérot optical fibre sensor is given in the next paragraph. Following that, each step of the manufacturing process is detailed in the subsequent sections.

A low finesse intrinsic Fabry-Pérot optical fibre sensor is consisted of two mirrors of low reflectivities. One mirror is a thin film of chromium sandwiched between two optical fibres which are spliced together, while the second mirror is formed from a bare fibre end. A chromium thin film is deposited on the tip of the cleaved fibre by sputter coating. The reflectivity of the mirror as a function of thickness has been controlled and measured, during chromium deposition and after splicing, respectively. The second mirror's reflectivity corresponds to a Fresnel reflection of 3.4% (glass/air interface).

A second, uncoated, cleaved fibre is spliced onto the coated fibre, using a filament fusion splicing system. The spiced fibre is then cleaved with the high precision cleaving tool at a distance between 50  $\mu\text{m}$  – 100  $\mu\text{m}$  with the Fabry-Pérot optical cavity then formed between the chromium layer and the bare fibre end. The waveguiding fibre that was used for all the sensors was a SMF28 ultra optical fibre, while the sensing element fibre of each type of Fabry-Pérot sensor is presented in **Table 2**.

*Table 2. Types of Fabry-Pérot optical fibre sensors that were manufactured during this project.*

Fabry-Pérot sensor's type	Ge-doped	F-doped	Pure SiO <sub>2</sub>	Ge-doped (Stepped)
SMF28 ultra (9/125) – Cr – ...	SMF28 Ultra (9/125)	F-SM1500SC (9/125)	PCF ESM-12B (9/125)	SM1500 (7.8/80) – SM1500 (4.2/50) – Cr – SM1500 (4.2/50)

### 3.2 Cleaving

The purpose of the fibre cleaving is to obtain a flat plane surface of on the edge of the fibre without residual debris on its tip and most importantly avoiding any angle cut. A perfect flat cleave will give a good alignment at the splicing procedure omitting splicing faults. An optical fibre stripper (ST-500) has been used to remove the plastic



jacket and the buffer coating from the optical fibre. After removing the buffer coating from the fibre, isopropanol is used to clean the fibre, removing any residual debris and dust from its cladding. Then the stripped and cleaned optical fibre is placed to the fibre cleaver obtaining a cleaved edge. The accuracy of the angle at the cleaved end is less than  $0.5^\circ$  according to the company's technical specification data sheet [126].

A second cleaving tool (FK11 STD, PK Technology Ltd) that has been used for accurate cleaving of the optical fibre. The standard FK11 is designed for cleaving standard telecom fibres in preparation for fusion splicing and fibre testing and its cleave angle repeatability is less than  $0.6^\circ$  angle degrees [127]. Using a microscope, it is possible to identify the position of the splice and with the help of a calibrated length the fibre was positioned to allow a cleave at a measured distance from the splice, leading to a cavity length. Thus, a camera connected to a microscope was used to control the position at which a desirable cleaving of the fibre with an accuracy of  $\pm 5\mu\text{m}$  was achieved. The aim is to cleave at a specific position on the optical fibre, as this final cleave will define the cavity length of our sensor.

### **3.3 Coating of Fibre Tip**

Fibres tip coating was achieved by RF sputtering in a coating chamber. The coating chamber is capable of sputtering samples with various metals. Using sputtering, glass materials can be thin film metallised. In short, RF sputtering is a non-thermal vaporization process, with which surface atoms of a chosen material are ejected onto the sample for coating. These atoms are physically ejected from the target by momentum transfer, typically by gaseous-ions accelerated from a plasma [128, 129].

A bundle of cleaved fibres was placed 20 mm above the sputtering target inside a vacuum chamber. The metal of choice for coating the fibre tips is chromium. Chromium is used because of its high melting temperature of around  $1900^\circ\text{C}$  which guarantees survival of the thin coating during the fibre fusion splicing process. The metals of interest are restricted due to the high temperature sensing applications [130].

#### **3.3.1 Chromium Thickness – Thin Mirror Reflectivity**

A series of experiments were conducted to estimate the chromium thickness and reflectivity of a Fabry-Pérot sensor after its integration. The reflectivity experiments were carried out during each sensor's fabrication. A variety of chromium reflectivities

were achieved by stopping the sputtering process at different time periods. A theoretical analysis of chromium reflectivity was conducted to estimate the experimental chromium thickness of each manufactured optical fibre Fabry-Pérot sensor. Due to the lack of accurate experimental measurement of the chromium thickness it was used a theoretical model (Essential McLeod software) which calculates chromium thickness (nm) on a medium through chromium reflectance (%) values. The experimental reflectance during chromium deposition on the optical fibre has been measured (EXFO IQS-500 detector) and correlated with the theoretical reflectance from the theoretical model (Essential McLeod software), providing a rough estimation of the chromium thickness (nm) which is sandwiched between two spliced optical fibres and form the Fabry-Pérot sensor. The reflectivity between two media was analysed in Chapter 2 and it depends on their refractive indices.

#### **3.3.1.1    *Theoretical analysis of thin mirror reflectivity***

The Essential McLeod software [131] was used for theoretical simulations, in order to investigate how the chromium deposition will affect the reflectivity of our sensor. **Figure 34** and **Figure 35** depict the reflectance and transmittance respectively, of fibre's end with respect to chromium layer's thickness. Both the reflectance and transmittance versus thickness were calculated, for two formations which are fibre-Cr-air and fibre-Cr-fibre. On these theoretical calculations, it is estimated the final chromium thickness of the Fabry-Pérot sensors, as it was difficult to measure their accurate value due to their nanometre size.

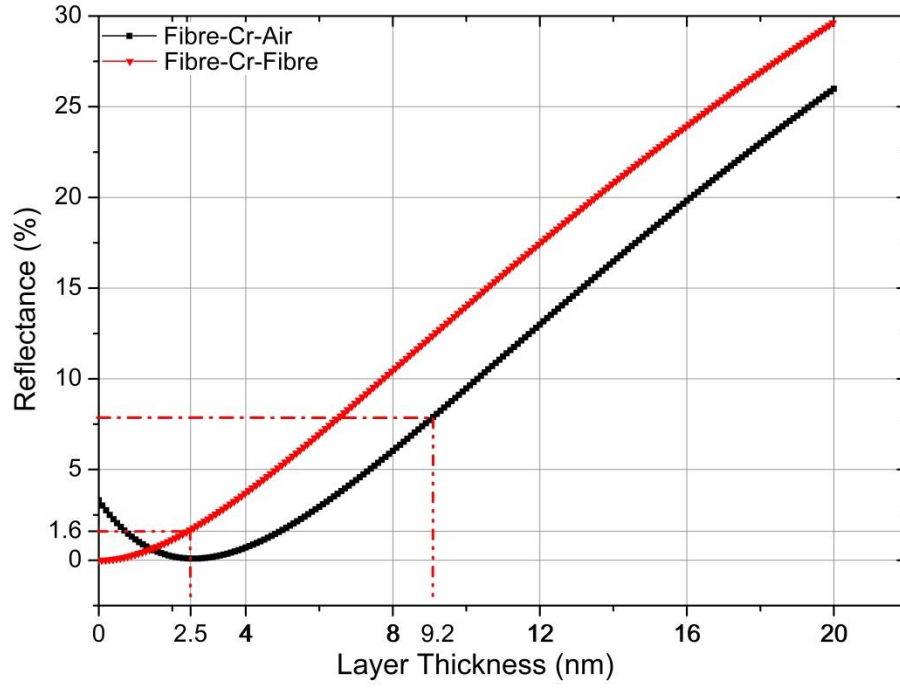


**Figure 34. Theoretical analysis of reflectance vs chromium thickness of the deposited thin film on the tip of the fibre (fibre-Cr-air →black data and fibre-Cr-fibre →red data).**

As it can be seen, for fibre-Cr-air formation the reflection starts from 3.4% corresponding to Fresnel reflection. At the beginning of the chromium thickness deposition the reflectance shows a slight down curve up to ~2 nm chromium layer. This is caused due to scattering of the waveguiding light after the first chromium particles start to be deposited on the tip of the fibre. After 2nm thickness the reflectance follows a linear behaviour.

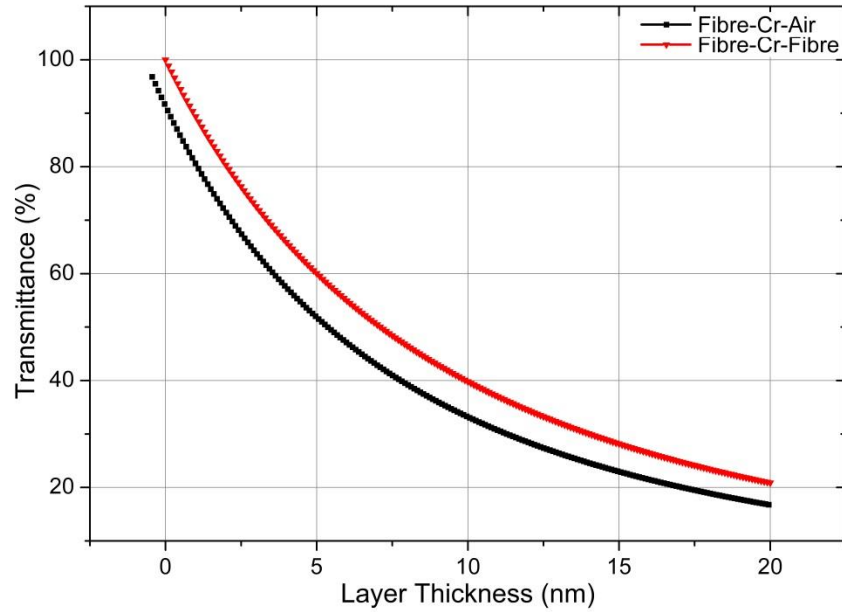


**Figure 35. Theoretical analysis of transmittance vs chromium thickness of the deposited thin film on fibre's tip (fibre-Cr-air →black data and fibre-Cr-fibre →red data).**

The same scattering effect is obvious in **Figure 35** as well, as the transmittance of the fibre-Cr-air formation starts from 96.6%. On the other hand, the fibre-Cr-fibre formation has a nonlinear behaviour from the beginning and throughout the chromium deposition starting from 0% reflectance and 100% transmittance. The red dotted lines in **Figure 34** show the correspondent chromium thicknesses for the reflectance values that have been measured before and after splicing.

### 3.3.1.2 *Experimental analysis of thin mirror reflectivity*

The reflectivity of each fibre's end face was measured experimentally during the chromium deposition procedure. The reflectivity of the fibre end face was measured by using a tuneable laser source, a 50 by 50 coupler and an EXFO IQS-500 detector. A reference fibre was positioned in a bundle of cleaved fibres in the coating chamber for chromium thin layer deposition. The reference fibre was connected to the EXFO interrogation system which recorded the back reflected power from the fibre's tip. By bending the reference fibre, the offset ( $\mu\text{W}$ ) of the back reflected power signal, can be detected and subtracted from the measured values. The loop stops the launched light in the optical fibre, hence the detected power represents the offset that should be considered during the back reflected power measurements. The received power to the detector corresponds to the Fresnel reflection which has a typical value of 3.4%. Hence, the reflectance of the chromium layer in accordance with its thickness can be calculated from the power in  $\mu\text{W}$ .

**Figure 34** and **Figure 35** show the relationship between reflectance, and transmittance respectively, with respect to chromium thickness based on the theoretical modelling (Essential McLeod software). Both graphs present data for two model formations which are fibre-Cr-air and fibre-Cr-fibre, shown by black and red colour, respectively. **Figure 36** shows the relationship of the experimentally measured reflectance versus time emanating during chromium deposition for a fibre-Cr-air formation. **Figure 34** and **Figure 36** can be directly correlated as both show the reflectance behaviour for theoretical and experimental analysis while chromium is deposited on the tip of the optical fibre.

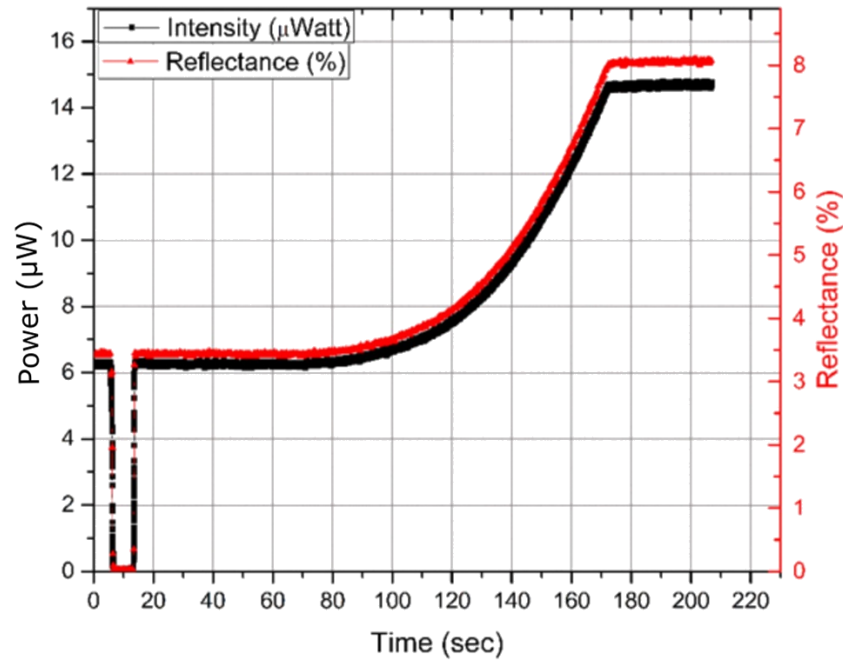


**Figure 36.** Experimental data of power ( $\mu\text{W}$ -left black axis) and reflectance (%-right blue axis) versus time (sec) of fibre-Cr-air formation during chromium deposition on the tip of a fibre.

**Figure 36** presents the experimental data of the reflected power of fibre's cleaved end during coating process with respect to the coating's time. By subtracting the power offset from the reflected power, which is  $7 \mu\text{W}$ , the value of Fresnel reflection power can be calculated. According to red dotted line of **Figure 34**, mirror's reflectance can be determined and consequently its thickness which is estimated roughly  $9.7 \text{ nm}$ . These data correspond to a series of sensors that was made with 8% reflectance for fibre-Cr-air formation. Nevertheless, this reflectance does not correspond to the final reflectance of our sensor, as after the chromium deposition another piece of SMF28 fibre is spliced on it to complete the final sensor. **Figure 37** exhibits the experimentally measured reflectance (%) of fibre-Cr-fibre formation. The step change in the middle of the graph is after making a loop in the fibre to extract the noise power offset from the measured reflected power. The power value after splice is  $3 \mu\text{W}$ , which corresponds to an experimental value of 1.6% reflectance (**Figure 37**) and a theoretical estimation of  $2.5 \text{ nm}$  (**Figure 34**) chromium thickness of the integrated Fabry-Pérot sensor. This chromium thickness is the final remaining thickness after splicing, for the same optical fibre sensor of 8% reflection fibre-Cr-air formation.

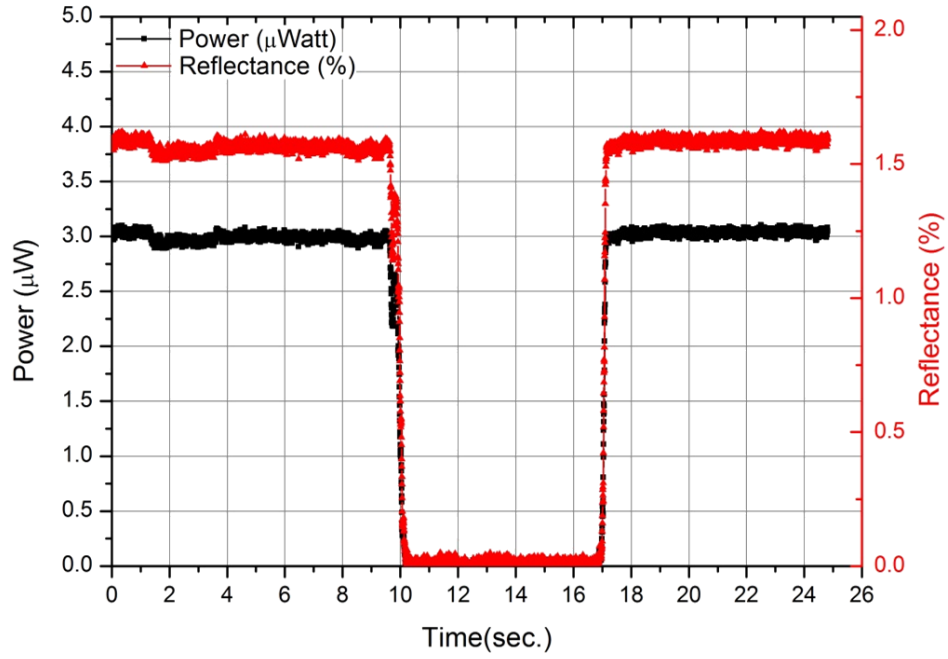


*Figure 37. Experimental data of power ( $\mu\text{W}$ -left black axis) and reflectance (%-right blue axis) versus time (sec) of a fibre-Cr-fibre formation after splicing.*

In summary, chromium's back reflected power ( $\mu\text{W}$ ) was measured experimentally which then was converted to reflectance (%) units. The experimental measured reflectance (%) was correlated with the theoretical reflectance (%) calculated with respect to chromium's thickness. Consequently, based on the match of the experimental and theoretical reflectance, chromium's thickness before and after splice has been theoretically estimated. **Table 3** summarizes the experimental and theoretical data of the reflectivity experiment leading to the chromium thickness theoretical estimation, as an experimental measurement of chromium's thickness couldn't be done. It can be seen, that after the splice of another fibre onto the chromium coated one, the reflectivity is decreased by roughly by 80%. This is caused by the refractive index difference between the air and the optical fibre that was spliced afterwards. Also, the chromium thickness is decreased by the high temperature heat generation at the splice region by the omega shaped tungsten filament of the Vytran fusion splicer. Despite the fact our sensor's spectrum intensity is decreased by chromium's thickness decrease, the sinusoidal signal remains low finesse.

**Table 3. Reflectivity and Chromium thickness during and after Fabry-Pérot sensor's fabrication.**

Initial	After Chromium Coating	After Splicing	McLEOD Theory	
Reflectivity (Fresnel)	Reflectivity (fibre-Cr-air)	Reflectivity (fibre-Cr-fibre)	Coating Thickness (fibre-Cr-air formation)	Coating Thickness (fibre-Cr-fibre formation)
3.4%	8%	1.6%	9.2 nm	2.5 nm

### 3.4 Splicing

After the chromium deposition, both the coated and uncoated fibres were cleaned in an ultrasonic bath before splicing. Alignment of both fibres is achieved, with a Vytran FFS-2000 fusion splicing workstation by placing them on the fibre holder jigs. While both cores of the fibre are aligned, suitable parameters (**Table 4**) for optimized splicing the coated fibre is spliced to another uncoated fibre are chosen.

**Table 4. Splice powers for splicing fibres with various diameters.**

Fibre diameter ( $\mu\text{m}$ )	Splice power (W)
125 – 125	20
125 – 80	19
80 – 50	15.5
50 – 50	13.5
125 – 125 (PCF fibre)	18.5

The splice parameters were adjusted to obtain splices of a vigorous tensile strength. Several different types of Fabry-Pérot sensors were made, by splicing fibres with different diameters. According to splicing data records, throughout the integration of the sensors, some indicative splicing powers for each type of fibre are given in **Table 4**. These splice powers parameters are valid for a new tungsten filament. Choosing a wrong splice power can lead to faulty splicing between the fibres, causing the failure of Fabry-Pérot sensor's integration.

#### 3.4.1 Splice Quality and Faulty Splices

A strong and well aligned splice eliminates signal loss thus maintaining the fringe visibility of the interferometric signal. **Figure 38** depicts a strong and well aligned splice between two SMF28 ultra fibres. The chromium mirror is visible and indicated by captions, as well. The red dotted lines represent the loss estimation of the splice which in this case is 0.01 db.

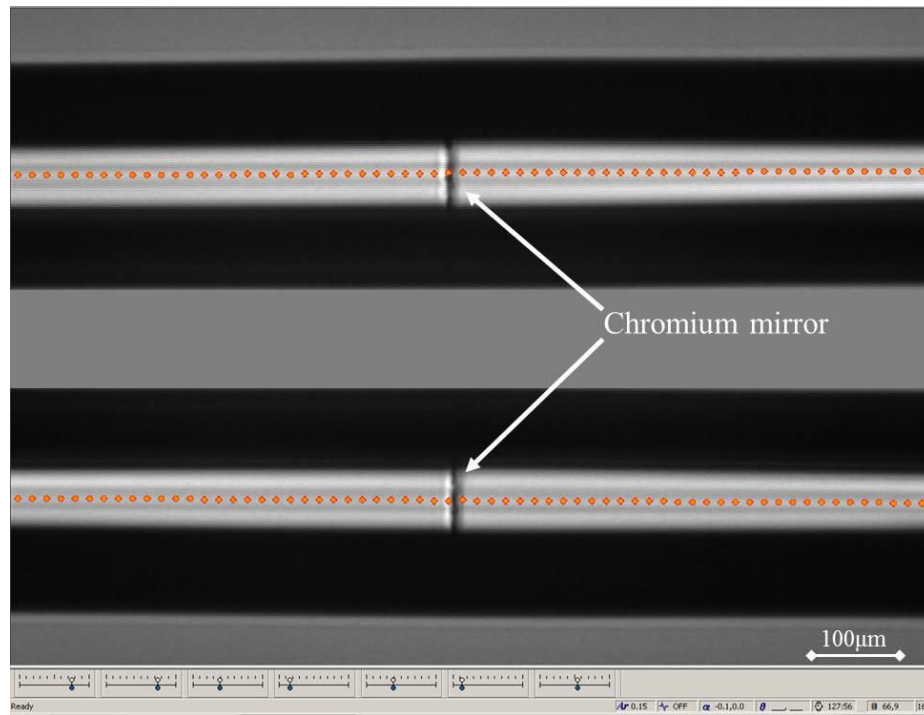


**Figure 38.** Screenshot of x-view and y-view alignment after a successful splicing of two optical fibres using the Vytran fusion splicing software. The dotted lines show the splice loss estimation which is 0.01 db.

Both the optical and mechanical properties of the reflective splice were found to be highly dependent on the quality of the fibre cleaved end, and successful splices required precise cleave angles (within  $1^\circ$  of perpendicular to the fibre axis). A small misalignment between the fibres during the splicing process can cause a significant loss in reflectivity. An example of a faulty splice (bubble phenomenon) which was caused by wrong splice power (18W) or a bad cleaved end (more than  $1^\circ$  angle) is presented in **Figure 39**. Despite the good alignment between the cores, its splice loss is estimated to 0.44 dB according to Vytran software.



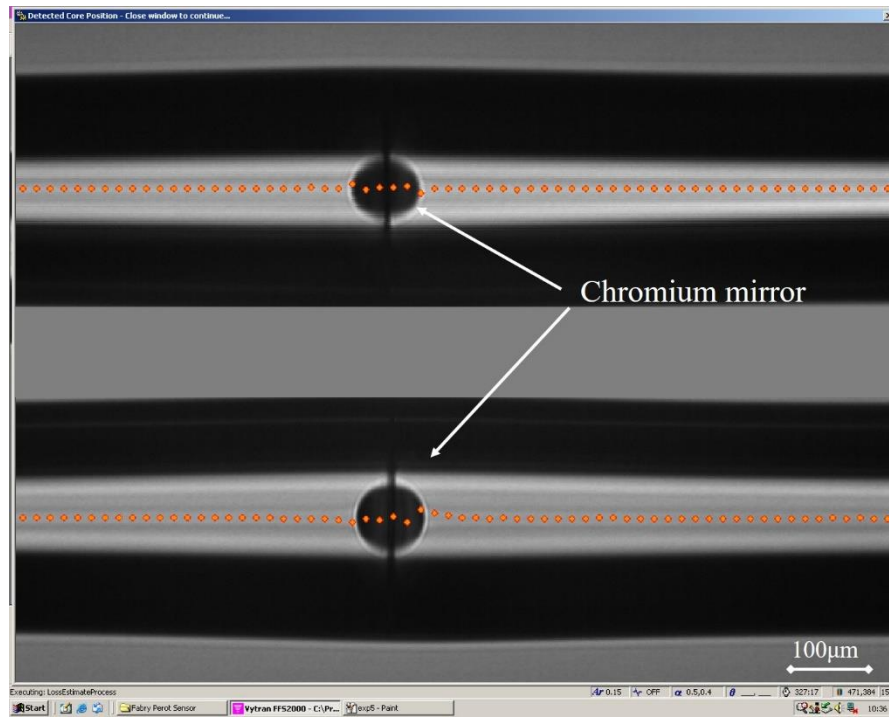


**Figure 39.** Screenshot of x-view and y-view alignment after a faulty splicing of two optical fibres using the Vytran fusion splicing software. The dotted lines show the splice loss estimation which is 0.44dB.

The result of a faulty splice, similar to the one presented in **Figure 39**, is obvious at the spectrum of a 97µm cavity Fabry-Pérot sensor and is depicted in **Figure 40**. Its fringe visibility is calculated to 0.1. On the other hand, **Figure 41** depicts a spectrum of a 65µm Fabry-Pérot sensor with a fringe visibility of 1.

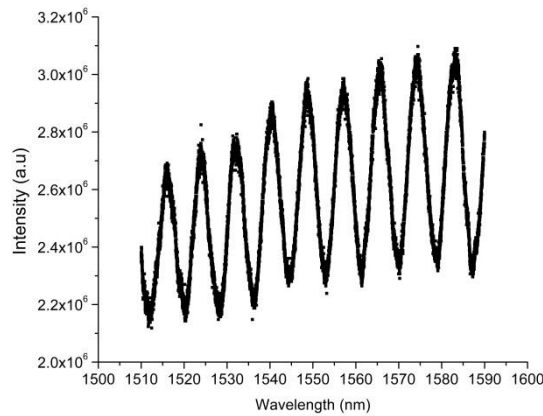


**Figure 40.** Spectrum of a Fabry-Pérot sensor with a 97µm cavity length caused by a faulty splice. Its fringe visibility is 0.1.

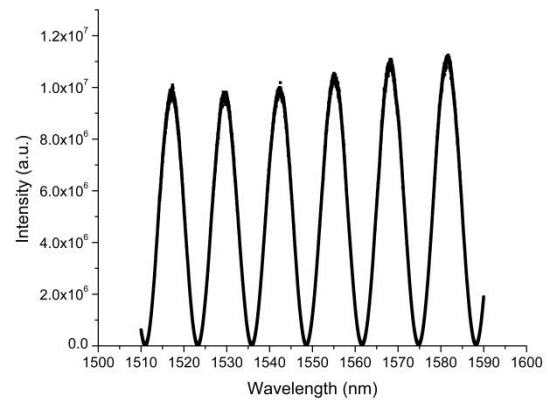


**Figure 41.** Spectrum of a Fabry-Pérot sensor with a 65µm cavity length. Its fringe visibility is 1.

### 3.4.2 Splice Strength Testing

A series of fibres were coated with different chromium thicknesses by measuring the reflected power during coating deposition process. The measured reflectivities of the fibres are 6%, 8%, 12%, 15% and 20% which correspond to theoretical chromium

thicknesses of 8nm, 9.2 nm, 11.5 nm, 13.2 nm, and 16.2 nm respectively. These chromium thicknesses are extracted from **Figure 34**, for a fibre-Cr-air formation.

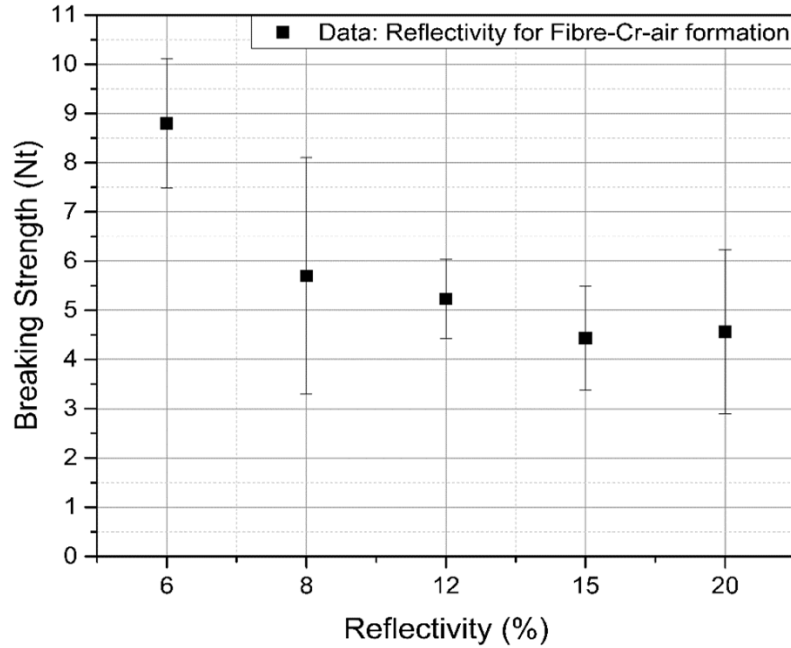


**Figure 42.** *Experimental data of splice breaking strength test for various chromium reflectivities. Each reflectivity corresponds to a specific value of thickness, calculated by McLeod software.*

The spliced fibres, of fibre-Cr-fibre formation, were subjected to strain tests evaluating the strength of the splice. Several fibres of the same chromium thickness were used obtaining a statistical estimation of the breaking strength. The results can be seen at **Figure 42**. As it can be seen, the strain strength is needed to break the splice joint of a 6% reflectivity is approximately 9 Nt, while for 8% reflectivity and above the breaking strength varies between 4 Nt and 6 Nt. There was no reason to increase sensors' mirror reflectivity above 8%, as the splice between the fibres becomes weak. Hence, considering that a measured reflectivity between 6% and 8%, for a fibre-Cr-air formation, gives a strong splice between the fibres, the sensors were built with reflectivities varying in this range.

### 3.5 Integration of Intrinsic Optical Fibre Fabry-Pérot sensor

During this project, it was manufactured and tested several Fabry-Pérot optical fibre sensors, of different formations and sensing elements. The two formations of Fabry-Pérot sensors were accomplished to build is a 125  $\mu\text{m}$ -Cr-125  $\mu\text{m}$  and a 125  $\mu\text{m}$ -Cr-80  $\mu\text{m}$ -50  $\mu\text{m}$ -Cr-50  $\mu\text{m}$ . Both a Ge-doped core characterizes sensors. However, several 125  $\mu\text{m}$ -Cr-125  $\mu\text{m}$  formation sensors were built with different types of sensing elements. The characteristic of each type is its different type of dopant, using Ge-doped

core, F-doped depressed cladding and pure coreless SiO<sub>2</sub> sensing element. In **Table 2**, is presented the formation and the type of sensing element of each sensor.

### 3.5.1 Sensor Type 1 formation: 125 $\mu$ m-Cr-125 $\mu$ m

An illustration of the manufacturing steps of a 125  $\mu$ m-Cr-125  $\mu$ m sensor type, is presented in **Figure 43**. **Figure 43(a)** demonstrates the splicing sequence starting by pushing them to positions with a specific gap. The gap should be between 4  $\mu$ m and 5  $\mu$ m.

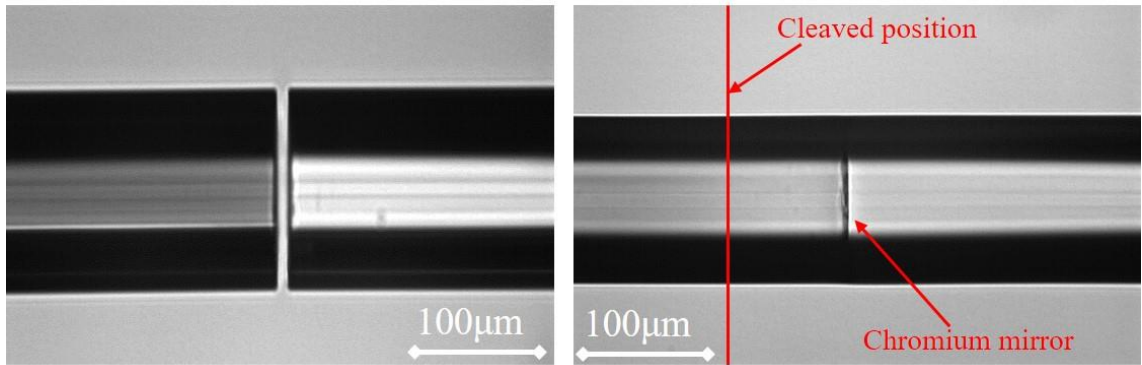


**Figure 43.** Manufacturing steps for 125  $\mu$ m-Cr-125  $\mu$ m type of a Fabry-Pérot sensor before and after splicing. Initially alignment of gap, cladding and cores is achieved. Then the fibres are spliced together with the chromium layer sandwiched between them. The cleaving position it's marked with a red vertical.

The cladding, gap, and core alignment of the two fibres according to their cladding diameter is presented at **Figure 43**. Splicing fibres with the same diameter is an easy process as the alignment is executed automatically. The red line in the latter photo of **Figure 43**, indicates the position where the fibre it is going to be cleaved. After that, the integration of a 125 $\mu$ m-Cr-125 $\mu$ m type Fabry-Pérot sensor is finished.

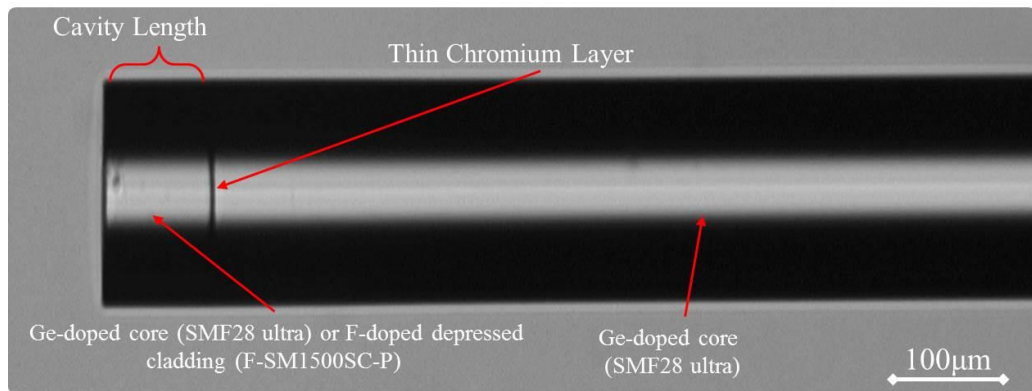


**Figure 44.** Microscope image of 60  $\mu$ m optical cavity length Ge-doped Fabry-Pérot optical fibre sensor.

The result, which is presented in **Figure 44**, is an integrated Ge-doped SMF28-Cr-SMF28 with a 60  $\mu\text{m}$  optical cavity. The same manufacturing process is executed for the integration of an F-doped depressed cladding Fabry-Pérot sensor. The only difference is the sensing element replacement by an F-SM1500SC (9/125) optical fibre. Both SMF28 ultra and F-SM1500SC fibres share the same characteristics, such as core and cladding diameters.

### 3.5.2 Sensor Type 2 formation: 125 $\mu\text{m}$ -80 $\mu\text{m}$ -50 $\mu\text{m}$ -Cr-50 $\mu\text{m}$

The basic motivation for making these stepped type sensors is their encapsulation in fused silica capillaries. After trying to encapsulate a Type 1 sensor, the results were not as satisfactory as it was expected, due to the great losses ( $\sim 40\%$ ) that took place after splicing a capillary on the sensor using an arc splicer. As it can be seen in **Figure 45**, due to the different fibre diameters this type of sensor needs many fabrication steps during its manufacturing, making its integration time consuming and complicated. Each manufacturing step is presented in order at **Figure 45**, and the splicing power for each fibre combination is given in **Table 4**.

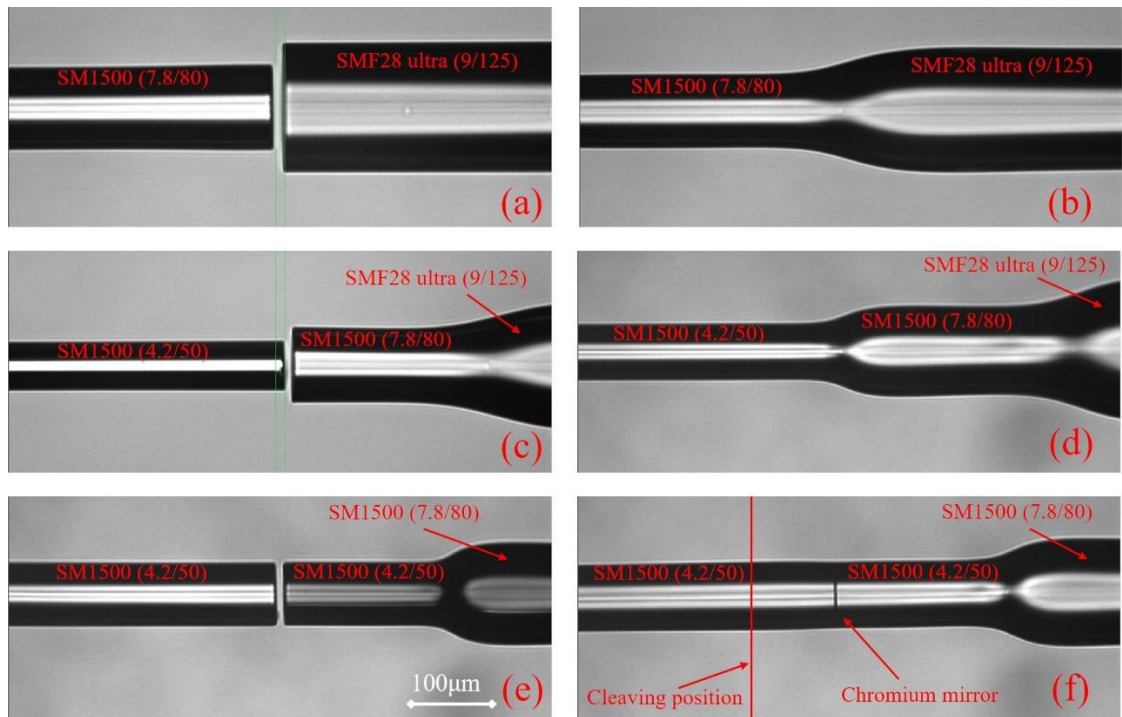


**Figure 45.** Manufacturing steps for 125  $\mu\text{m}$ -80  $\mu\text{m}$ -50  $\mu\text{m}$ -Cr-50  $\mu\text{m}$  type of a Fabry-Pérot sensor. For each photo, the core alignment is achieved manually due to the different cladding and core diameters of the fibres. Photo (f) depicts the 50 $\mu\text{m}$  fibres spliced together with the chromium layer sandwiched between them.

Following the photos of **Figure 45**, an alignment and splice between a 125 $\mu\text{m}$  and 80 $\mu\text{m}$  fibres is depicted in **Figure 45(a-b)**, respectively. The 80 $\mu\text{m}$  fibre is cleaved at an approximate length of 200 $\mu\text{m}$  and it is positioned again on splicer's jig holder to be aligned and spliced with a 50 $\mu\text{m}$  fibre (**Figure 45(c)**, **Figure 45(d)**). Finally, the 125 $\mu\text{m}$ -80 $\mu\text{m}$ -50 $\mu\text{m}$  formation is coated with chromium and is ready to be spliced to a 50 $\mu\text{m}$  fibre, as it can be seen in **Figure 45(f)**. The red vertical line in the latter photo is the position at which the 50 $\mu\text{m}$  fibre will be cleaved leading to the final integration of type 2 sensor. All photos of **Figure 45** show the fibres after the core alignment is achieved. The core alignment has been done manually due to different cladding and core diameter of the fibres. In **Figure 46**, is depicted the final integration of Type 2 Fabry-Pérot optical fibre sensor.

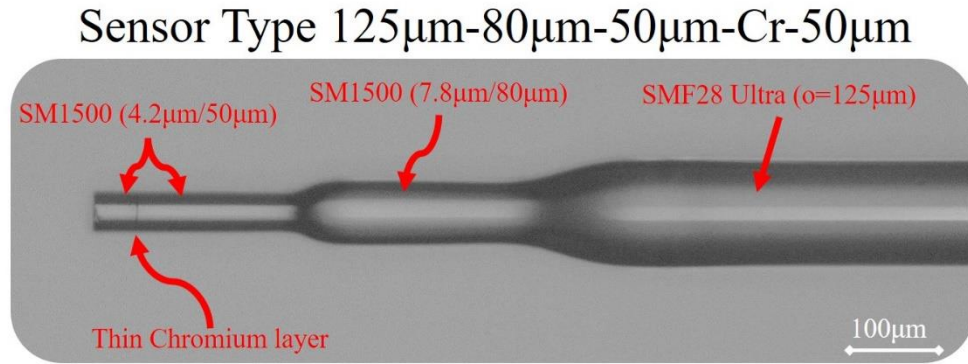


**Figure 46.** Microscope image of 52  $\mu\text{m}$  optical cavity length Ge-doped stepped Fabry-Pérot optical fibre sensor [95].

Normally, the stepped Fabry-Pérot optical fibre sensor is inserted in a silica capillary. Hence, the cleaved end of the sensor will be protected from possible contamination by surrounding powder during embedment in metallic components. A contamination would affect the reflectivity of the second mirror and thereby the reflected spectrum of the sensor. These encapsulated Fabry-Pérot sensors are made for another part of our group's research project, in order to be used for reliable high temperature sensing inside smart metallic components for the power generation industry. However, all the sensors that were subjected to long term stability tests at high temperatures, were not encapsulated but they were sitting freely in fused silica tubes in the furnace.

### 3.5.3 Sensor Type 3 formation: 125 $\mu$ m-Cr-125 $\mu$ m (PCF-ESM12)

The process of manufacturing a Type 3 pure SiO<sub>2</sub> sensor follows the same sequence as the previous type of sensors with small differences throughout its fabrication. This sensor's fabrication, presented at **Figure 47**, was designed with the scope to eliminate the dopant from the sensing cavity of the sensor.

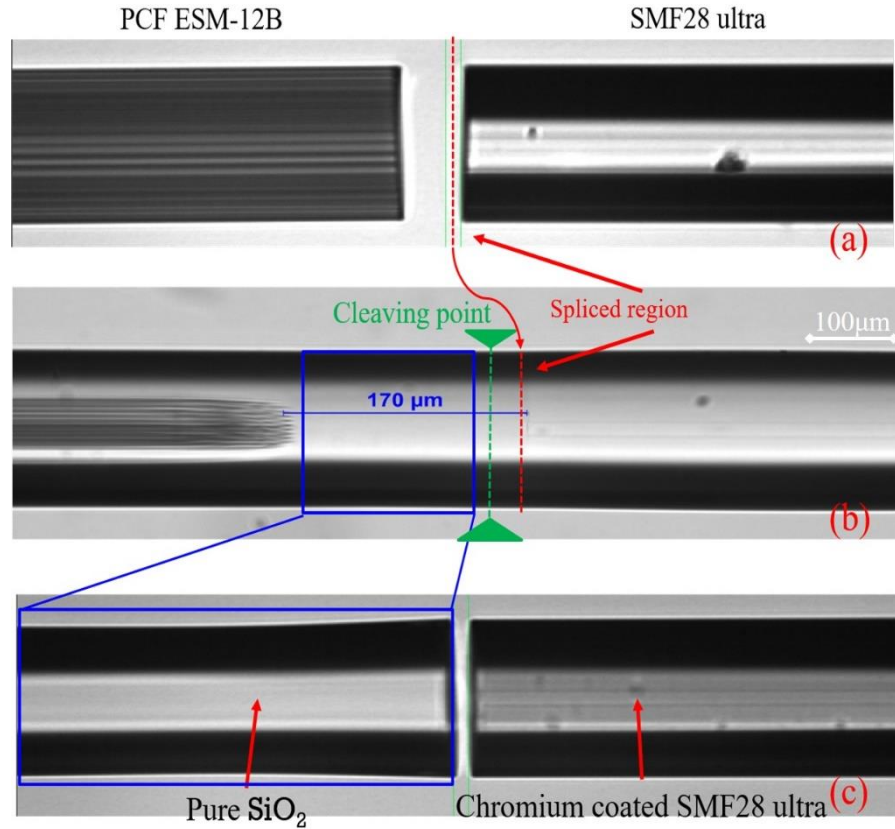


**Figure 47.** Manufacturing steps of an undoped pure SiO<sub>2</sub> cavity Fabry-Pérot sensor. At photo (b) it can be seen the still intact air holes which haven't collapsed from the splicing process, the pure SiO<sub>2</sub> piece and the SMF28 fibre. The green dashed line is the cleaving position from which the pure SiO<sub>2</sub> piece can be extracted. The red dashed line is the position of the PCF-SMF28 splice.

**Figure 48** depicts the cross section of the PCF fibre. The reason for choosing this type of optical fibre was to collapse the air holes through the splicing process and form a short piece of pure SiO<sub>2</sub> fibre. This can be seen at **Figure 47(b)**, where the PCF fibre is spliced to the SMF28 ultra fibre creating 170  $\mu$ m length of pure SiO<sub>2</sub> piece of fibre. The red dashed line indicates the splice point. Both the core of the SMF28 fibre and the coreless piece of SiO<sub>2</sub> are visibly clear, on the right and left side, respectively.



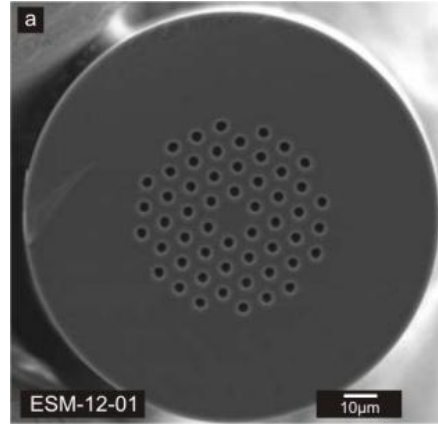


**Figure 48.** PCF ESM12 cross section showing the air holes which were collapsed during splicing with a filament fusion splicer. The outcome is a piece of pure SiO<sub>2</sub> piece of fibre from which several coreless pure SiO<sub>2</sub> FP sensors can be made [132].

The PCF-SMF28 formation is cleaved with a high precision cleaver at a position (green dashed line) close to the air holes ( $\sim 20 \mu\text{m}$  from the splicing joint). The pure SiO<sub>2</sub> piece is then spliced to a cleaved, chromium coated SMF28 fibre (**Figure 47(c)**) which eventually will form a pure SiO<sub>2</sub>-Cr-SMF28 sensor. A final cleaving of the pure SiO<sub>2</sub> region at  $60 \mu\text{m}$  leads to a pure SiO<sub>2</sub> intrinsic Fabry-Pérot sensor (pure SiO<sub>2</sub>-Cr-SMF28 ultra) with an optical cavity of  $60 \mu\text{m}$ , shown in **Figure 49**.

The splice power that was used to splice the SMF28 ultra fibre to the PCF fibre is  $18.5 \text{ W}$  (**Table 4**). The optimal splice intensity at the SMF28-Cr-PCF set-up is crucial, as the aim is to fully collapse the PCF's air holes while in the same time the maximum breaking splice strength is achieved. Any deviation from the correct splice power can cause partially air hole collapse leaving air holes in the sensing cavity. The result will be undesirable interference in the Fabry-Pérot sensor's sinusoidal spectrum.

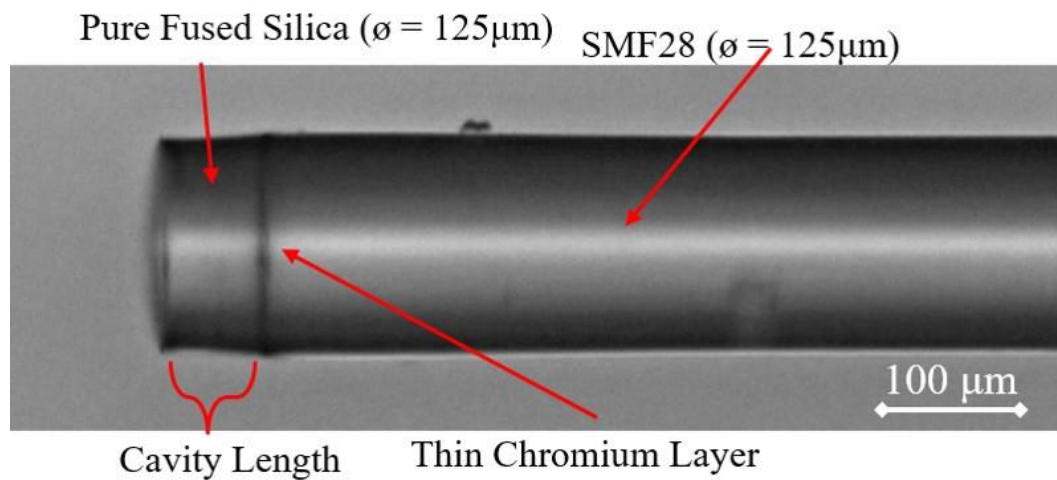


**Figure 49.** Microscope image of  $60 \mu\text{m}$  pure SiO<sub>2</sub> Fabry-Pérot sensor optical fibre sensor, made by a PCF ESM-12B optical fibre.

### 3.6 Conclusions of Chapter 3

In this chapter, a detailed description of the manufacturing process of several integrated intrinsic Fabry-Pérot sensors is presented. These sensors have been used for long term stability tests at high temperatures. Different type of sensing elements characterizes each type of intrinsic Fabry-Pérot sensor.

The cleaving, thin film deposition and splicing techniques during the fabrication of a sensor were analysed. The limitations and regimes of these techniques were highlighted as well, leading to a well-defined optical fibre sensor without losses and interferences at its sinusoidal spectrum. A theoretical and experimental analysis of thin mirror's reflectivity was obtained. Measuring the reflected intensity of fibre's cleaved end during the chromium deposition was theoretically quantified the thickness of the chromium mirror. In addition, breaking strength experiments were conducted, finding the optimum splice strength of the sensor.

Type 1 corresponds to a 125  $\mu\text{m}$ -Cr-125  $\mu\text{m}$  formation while type 2 to a 125  $\mu\text{m}$ -80  $\mu\text{m}$ -50  $\mu\text{m}$ -Cr-50  $\mu\text{m}$  formation. The latter type of sensor is referred as stepped sensor due to the different fibre diameters that were spliced together. Its sensing element is a 50 $\mu\text{m}$  diameter Ge-doped core. For type 1 formation were used two different sensing elements which are a SMF28 ultra (Ge-doped core) and an F-SM1500SC (F-doped depressed cladding) fibres. Finally, a type 3 with a 125  $\mu\text{m}$ -Cr-125  $\mu\text{m}$  formation sensor was fabricated with an undoped pure  $\text{SiO}_2$  sensing element made of a PCF ESM-12B fibre. Each sensor of the abovementioned were tested in a range of high temperatures between 850°C and 1150°C, whose stability response is investigated in Chapter 4.



## Chapter 4: Long-Term Stability Tests at High Temperatures

This chapter presents the long-term stability response of each type Fabry-Pérot (FP) sensor which has been manufactured. The long-term stability of the Fabry-Pérot sensors' phase response in a temperature range between 850°C and 1100°C, for periods of up to 4 months are investigated. Additionally, the use of a high precision thermometer (PREMA) for temperature recording, as well as the description of the errors that must be considered in the results, will be analysed. A series of experiments were conducted to estimate the accuracy of the thermometer under controllable temperature fluctuations.

An experimental and theoretical analysis of sensors with various cavity lengths is also presented. Each sensor was subjected to annealing and thermal cycles before the beginning and after the end of the long-term phase stability experiments. The term annealing cycle is used to refer that the sensor is subjected to temperatures up to 1000°C for the first time with a slope rate 3°C/min. The term thermal cycle represents the same process, with the same slope rate, after the sensor pre-existed up to temperatures of 1000°C. A comparison of the phase response versus temperature of the sensors before and after the phase stability tests is presented. Through this, an estimation of the sensor's phase response repeatability can be achieved. For each type of sensor that was described in **Chapter 3** were manufactured several of them, and were tested under the same circumstances for repeatability purposes.

In brief, Fabry-Pérot sensors' phase stability results, with Ge-doped core of type 1 and type 2 (see **Chapter 3**), F-doped depressed cladding and undoped pure SiO<sub>2</sub> are described in this chapter. Comparing the long-term stability tests of each sensor, it was found out that the dopant in the sensing element of each sensor plays an important role to its phase stability and robustness, especially for temperatures above 900°C. Many Fabry-Pérot sensors were fabricated and tested to establish repeatability.

### 4.1 High Precision Thermometer (PREMA) Error Analysis under Ambient Temperature Variations

Next pages analyse the use of high precision thermometer (PREMA) at temperature recording experiments, as well as the description of the errors that must be considered in the results. A series of experiments were conducted to estimate the accuracy of the thermometer (PREMA) and find out an optimized setup with the

minimum temperature error reading. After two breakdowns of type K thermocouples throughout the experiments, we decided to use thermocouples type N for our next experiments. The choice of N type thermocouple was based on their effective response without breakdowns up to 1300°C, and because they are well protected with a capillary from any oxidations of the environment. This conclusion came up due to our strong belief that oxidation of the surrounding environment caused the breakdown of type K thermocouples, as firstly were not protected and secondly the furnace tube was not supplied with noble gas throughout the experiments.

#### 4.1.1 High Precision Thermometer (PREMA) Stability Tests

The thermometer has been subjected to controllable temperature variations of its surrounding environment with the use of a foam box. The temperatures that were measured by thermocouples throughout the phase stability tests are not absolute but differential, using a RTD sensor as a cold junction. The RTD sensor is placed in a metallic block which records room's temperature. This experiment took place to evaluate the influence of the environmental temperature on the stability of the thermometer's temperature recording. Some possible reasons of overheating are the hot seasonal periods throughout a year and busy days where many people either work or walking around in the lab. Also, the thermometer was sitting above the furnace while the long term high temperature stability tests were conducting. That led to put a thermal insulation under the thermometer, avoiding the overheating due to furnace's high temperatures.

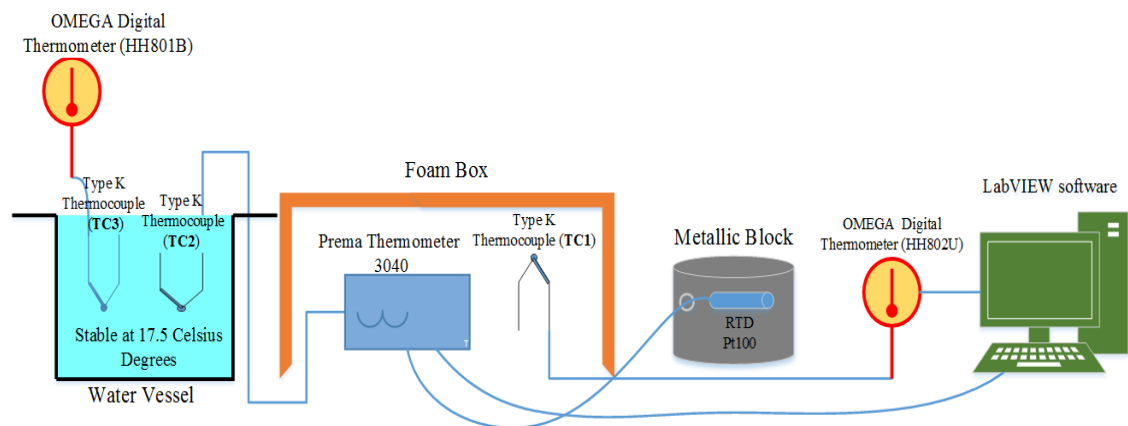


**Figure 50.** *Experimental setup of thermometer's temperature reading stability testing, without using a RTD Pt100 sensor as a cold junction calibration.*

The experimental setup is depicted in **Figure 50**. The thermometer was subjected to controllable temperature variations covering it with a foam box. Approximately after an hour the temperature inside the foam box has been increased by 5°C. In the meantime, the temperature reading of the thermometer was recorded, with a type K thermocouple (TC2) as well as the temperature of the environment (free space) in the foam box with a type K thermocouple (TC1). A third type K thermocouple (TC3) has been used to record vessel's water temperature throughout these experiments. After submerging TC3 and TC2 in the water, an interval of 30 minutes had to pass until their stabilization at 23°C, before the start of the experiment. The TC2 thermocouple, presupposes that the temperature reading of the Prema thermometer should stay unaffected from temperature variations. According to continuous observation of TC3, connected to a digital thermometer (OMEGA Thermometer HH801B), water's temperature was stable at 23°C throughout the experiment. It must be considered that throughout these experiments the temperature of the thermometer should stay the same.

#### ***4.1.1.1 Thermometer Stability Testing without the Use of a RTD sensor***

The stability behaviour of thermometer's temperature reading during the heating up/cooling down process is examined, without the use of a RTD sensor as a cold junction. **Figure 51** portrays the heating up process of the thermometer. Red data represent the temperature of the environment in the foam box measured by TC1, while blue data represent the temperature reading of vessel's temperature measured by TC2. During the heating up process the environmental temperature increased by 5°C, while the temperature reading of the thermometer has been decreased by the same temperature value. The conclusion is that the temperature reading has been affected by the environmental temperature increase.

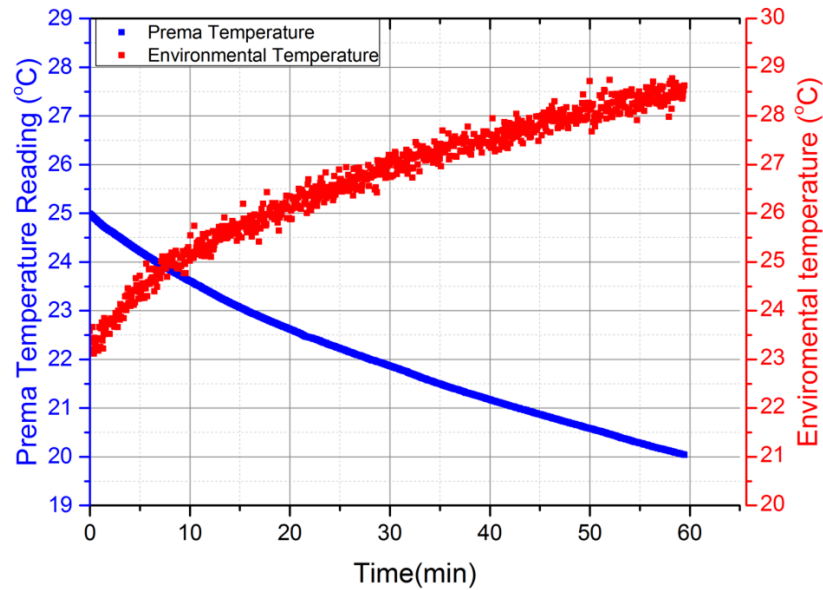


**Figure 51.** Experimental test of Prema thermometer temperature reading's stability (blue data) during the heating up of the environment temperature (red data) in the foam box.

In addition, the cooling down process of the environment was recorded, which is quoted in **Figure 52**. The environment temperature decreased rapidly, in less than 2 minutes. For 38 minutes, the environmental temperature exhibited some modulations ending up to 22°C. The variations of thermocouple TC1 were caused by possible temperature variations in the lab environment. For instance, my personal presence close to the thermometer and thermocouple during this experiment. In the meanwhile, the temperature reading of the thermometer didn't follow the fast drop down of the ambient temperature, which showed a slow rate lasted for 40 minutes.

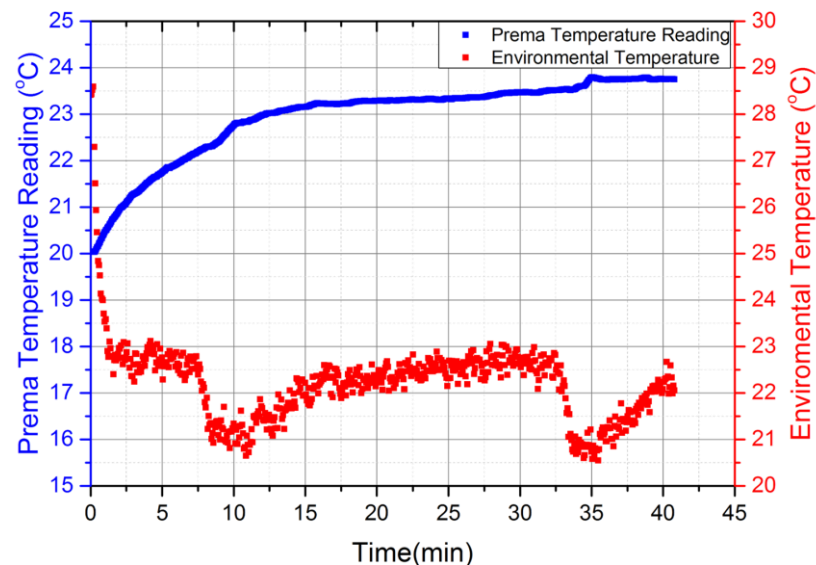


**Figure 52.** Experimental test of thermometer temperature reading's stability (blue data) during the cooling down of the environment temperature (red data) in the foam box.

As it was expected, the ambient temperature change affects the electronics of the thermometer. The heating of thermometer's electronics causes a change at its temperature reading, resulting to a temperature drop down when the ambient temperature is increased. The opposite happens when ambient temperature is decreased, then the temperature reading shows a temperature increase.

#### ***4.1.2 Prema Thermometer Stability Testing Using a RTD sensor***

The thermometer proved to be unstable to environment's temperature variations. In the same way, a RTD Pt100 sensor was introduced to experimental setup, placed in a metallic block. The RTD sensor, plays the role of cold junction calibration. Every 10 seconds the thermometer calibrates its temperature reading, according to the temperature of the cold junction (RTD sensor). The temperature of the RTD sensor measures the room temperature at a fixed point, and the metallic block ensures its robustness.

##### ***4.1.2.1 RTD Sensor Positioned out of The Foam Box***

In this situation, the metallic block with the RTD sensor were placed outside of the foam box, heating up the Prema thermometer separately. Only the Prema thermometer was heated and the RTD sensor was used as a cold junction calibration at room temperature. After connecting the RTD sensor to the thermometer, a temperature offset of roughly  $-3^{\circ}\text{C}$  was noticed at the thermometer reading. **Figure 53** presents thermometer's temperature reading which didn't stay stable despite the temperature increase of its surrounding. On the contrary, it has been decreased by roughly  $7^{\circ}\text{C}$ .

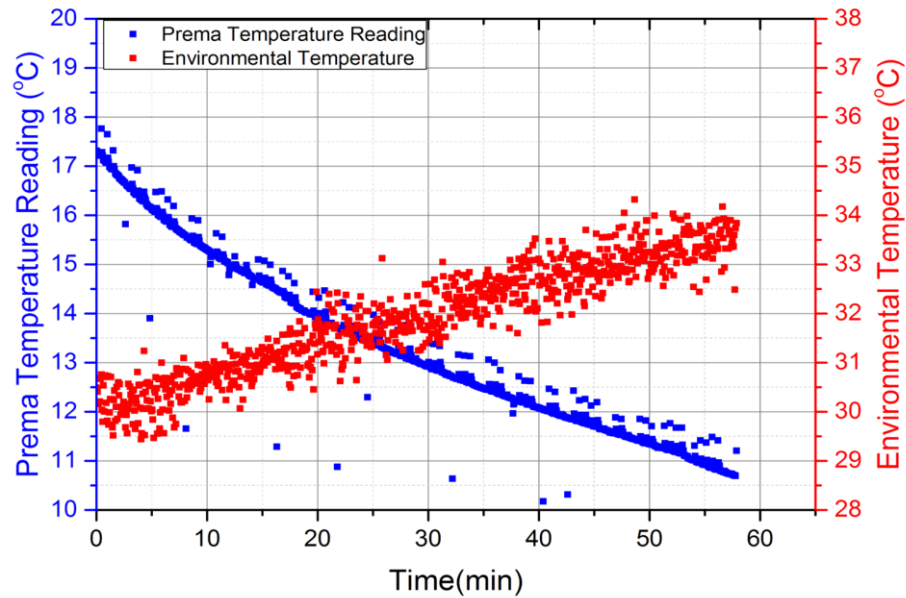


*Figure 53. Experimental test of thermometer stability (blue data) and the environment temperature (red data) while RTD is out of the foam box. Only heating up process is being displayed.*

In the case that RTD sensor sits outside the foam box while only the Prema thermometer is being heated, its temperature reading is utterly affected even though it is calibrated from the cold junction temperature of the RTD sensor. The cold junction RTD's temperature is kept stable throughout this experiment, but the Prema thermometer's electronics are affected and change the temperature indication.

#### **4.1.2.2 RTD Sensor Heated Separately**

The purpose of this experiment was to observe the thermometer's temperature reading in case the cold junction would be varying. Hence, an attempt to discover if a temperature variation on RTD sensor would affect the Prema thermometer's temperature reading was made, by placing the metallic block with the RTD sensor on a heat source. Afterwards, the metallic block was heated up to 14°C.

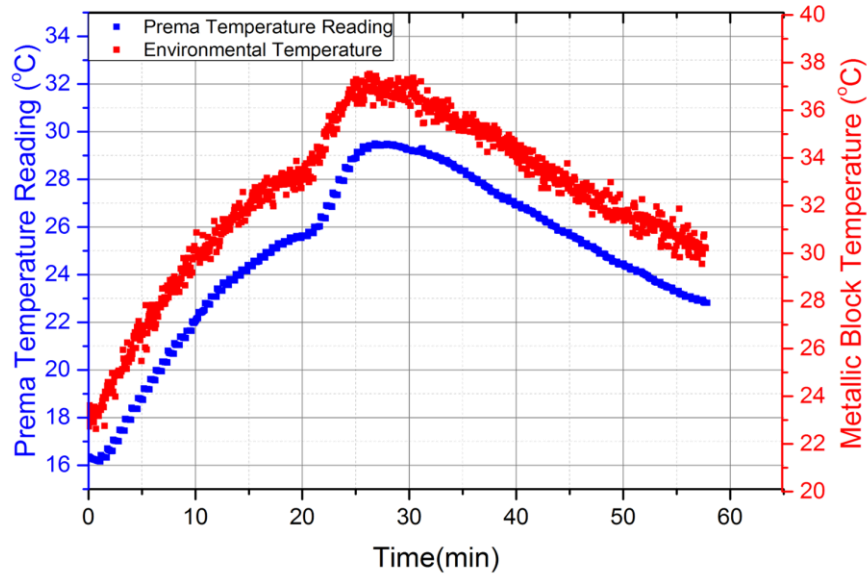


**Figure 54.** *Experimental test of thermometer stability (blue data) and the environment temperature (red data). RTD sensor was placed on a heat source separately from the Prema thermometer. Both heating up and cooling down processes are being displayed.*

In **Figure 54** is portrayed the temperature reading in accordance with the temperature of the metallic block. Apparently, the temperature variations of the metallic block directly affect thermometer, and consequently RTD sensor's variations as well. The temperature difference on both measurands seems to match, being roughly  $\sim 14^{\circ}\text{C}$ . In general, the temperature behaviours of both devices are identical. After all, this is expected as the temperature reading is calibrated every 10 seconds based on the cold junction temperature of the RTD sensor.

#### **4.1.2.3 RTD Sensor Positioned in the Foam Box**

Through this experiment, an estimation of the temperature reading stability of the thermometer while the cold junction calibration experiences the same temperature variations of the environment was made. According to previous experiments, it was realised that thermometer's electronics are affected by the temperature of its surrounding. Hence, the temperature of the environment wasn't increased more than  $5^{\circ}\text{C}$ , avoiding in this way any permanent damage to thermometer's electronics. **Figure 55** portrays the temperature reading of Prema thermometer (blue data), the environment temperature in the foam box (red data).

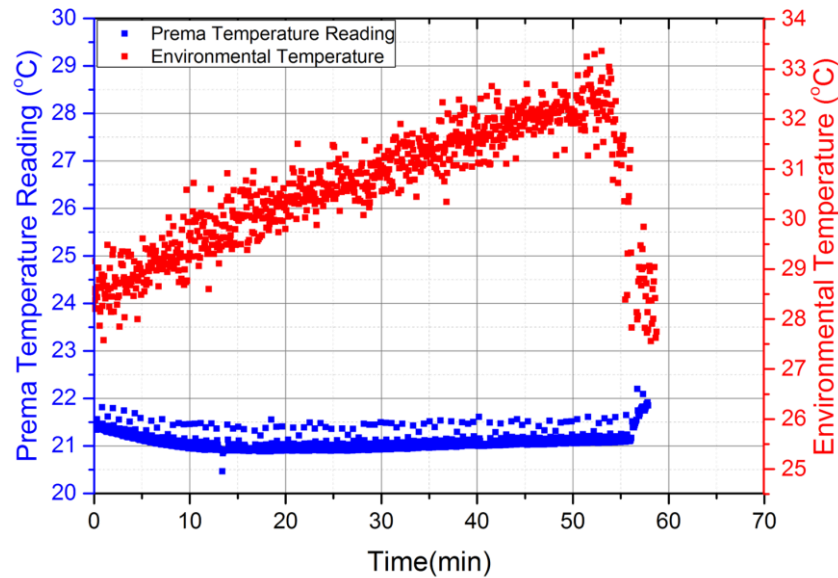


**Figure 55.** *Experimental test of thermometer stability (blue data) and the environment temperature (red data) while RTD is in the foam box. Both heating up and cooling down processes are being displayed.*

The result of this experiment, can be seen in **Figure 55**, showing that the temperature reading has been deviated by  $0.5^{\circ}\text{C}$ . The cold junction calibration of the RTD played an important role as it was changing in accordance to the temperature increase of the ambient, compensating the temperature reading. During the cooling down process, the thermometer's temperature reading delayed sensing the temperature difference of the environment. This is attributed to the fact that the metallic block prevents ambient temperature variations, especially if the variations are of small scale. When the RTD sensor is under the same circumstances with the thermometer its temperature reading is affected by the minimum, in comparison with previous experiments. Under those circumstances, the thermometer temperature reading stays unaffected when a RTD sensor is connected to it. Furthermore, while a RTD sensor is connected to it instabilities at the temperature reading still show up. Especially when each of the devices experience separately the temperature fluctuations. However, when both devices experience simultaneously environment temperature fluctuations, then the impact on the stability of the thermometer is kept to the minimum.

Concluding, it was proved that an environmental temperature fluctuation can affect the electronics of the thermometer, leading to reading errors. This effect can be minimized connecting a RTD sensor to the Prema, which functions as a cold junction temperature. Summarizing, it was noticed that a random or seasonal temperature fluctuation at the environment will interfere at the temperature reading of the Prema thermometer, especially when a RTD sensor cold junction calibration is not used.



## 4.2 Experimental and Theoretical Sensor Sensitivity Analysis

The sensitivity of a Fabry-Pérot sensor depends on its optical cavity length. The optical cavity length is defined by the effective refractive index ( $n_{\text{eff}}$ ) of the core and the physical length of Fabry-Pérot cavity. A series of sensors with different cavity lengths were subjected to several thermal cycles. Phase shift (2.3.2) corresponding to a temperature change increases with the increase of the cavity length. This result indicates a higher sensitivity for longer cavity lengths. A comparison of the experimental (lines) and theoretical (symbols) sensitivity data of these F-P sensors with different cavity lengths is shown in **Figure 56**. Comparing both experimental and theoretical phase responses in **Figure 56** it is apparent that the experimental phase response exhibits a very good match with the phase response of the theoretical modelling. By co-plotting the experimental and theoretical phase response, it can be seen that they are overlapping each other. Thus, it can be concluded that the theoretical model gives a very good estimation of the experimental performance of the sensors. The theoretical model of a Fabry-Pérot sensor performance was built on LabVIEW software.

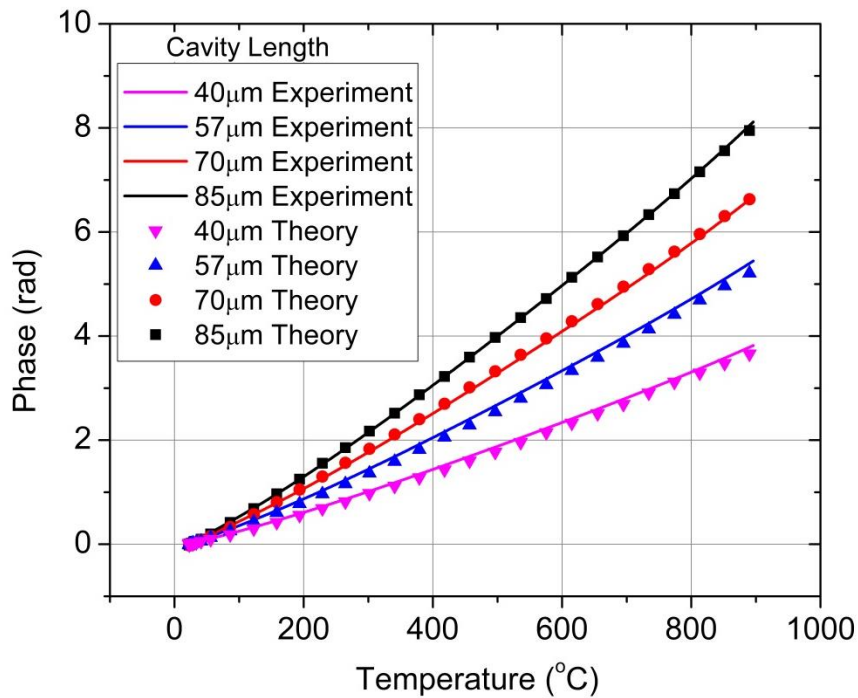


**Figure 56.** Experimental (lines) and theoretical (symbols) phase response of 4 Fabry-Pérot sensors from room temperature to 900°C. Each sensor has a different cavity length showing variation on its sensitivity. Phase values of the sensors are normalised to their phase value at 22°C.

As it can be seen in **Figure 56** the phase shift has a non-linear relationship. This nonlinearity is due to the thermo-optic property of the fibre material as explained in **Chapter 2**. The 2<sup>nd</sup> order polynomial behaviour comes from the 2<sup>nd</sup> order dependency

of fused silica (SiO<sub>2</sub>) thermo-optic coefficient on temperature [11, 55, 133-135]. In **Figure 56**, a sensor of 85μm cavity length (black data) exhibits a phase change of 8 radians over a temperature range of approximately 900°C. On the other hand, a 40μm cavity length (purple data) sensor, which has the half length of the sensor above, exhibits a phase change of 4 radians at the same temperature. The same values are applied for the theoretical phase response analysis. A 2<sup>nd</sup> order polynomial fitting was applied to both data sets. The 2<sup>nd</sup> order polynomial fitting function has the following form:

$$y = \text{intercept} + B_1 * x + B_2 * x^2 \quad \text{Equation 19}$$

The intercept, B<sub>1</sub> and B<sub>2</sub> of the theoretical and experimental fitting function of the 57μm cavity length sensor are -0.16307, 0.005, 1.4093e<sup>-6</sup> and -0.11576, 0.00432, 2.2186e<sup>-6</sup>, respectively. Despite the fact that there is slight deviation between the parameters they match correctly. The sensitivity for a given temperature is linearly proportional to its cavity length. **Figure 57** presents the experimental sensitivities for a variety of cavity lengths at 400°C, 700°C and 900°C. The sensitivities of the sensors were measured at three representative temperatures where according to the graph the longer cavities present higher sensitivities. Through phase sensitivity, a conversion of the phase units (radians) of the sensor to temperature units (Celsius degrees) can be achieved, which leads to an estimation of the sensor temperature drifts in units of Celsius degrees.

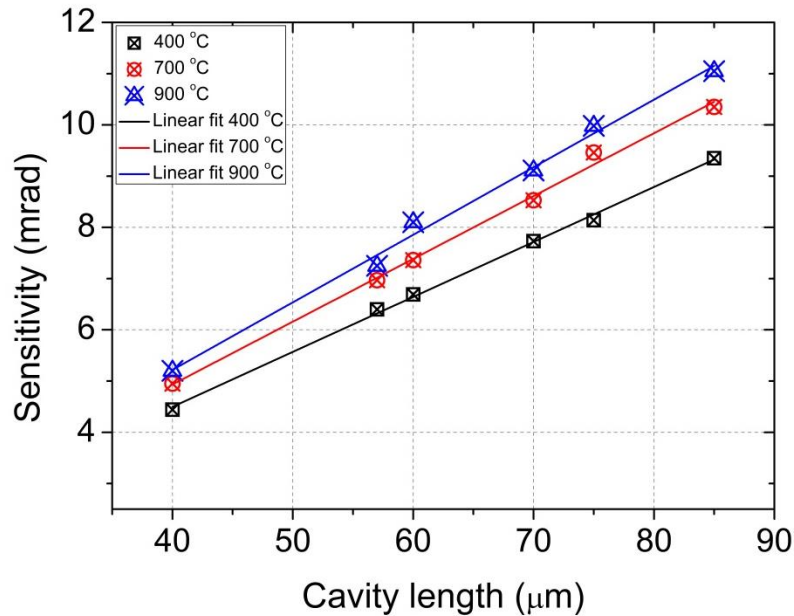


**Figure 57.** Experimental data of sensitivity versus various cavity lengths of Fabry-Pérot sensors. The sensitivity of each sensor was measured at different temperatures such as 400°C, 700°C and 900°C.

It is worth noting that the amount of data of interrogator system is the same (16000 data points, 2.3.3) for all sensors either short length or long length cavities.

Short cavities (spectrum consists of a few fringes) correspond to low frequencies after a FFT is applied on their interferometer spectrum, while long cavities (spectrum consists of many fringes) correspond to higher frequencies. An accurate detection of spectrum's fundamental frequency through single tone extraction is based on the sampling rate. Single tone extraction (2.3.3) uses an interpolation process to find the frequency, amplitude, and phase of the input signal. The interpolation is used due to the difference between the highest peak of the FFT output and the signal frequency, as the signal frequency and the sampling frequency are not precisely harmonically correlated. The sampling rate should be at least the highest frequency. As we cannot increase the data points of the FFT, and given that the interpolation of the FFT is not linear (a second order polynomial, quadratic, is fitted to the FFT output peak), low frequencies can be detected more accurately than the higher frequencies. Hence, short cavities are more accurate for our data analysis. On the other hand, the coherence of the interfering beams limits the maximum cavity length. While a longer cavity can give a higher sensitivity, the fringe visibility (and hence the signal-to-noise ratio) drops as the cavity becomes too long due to optical cavity losses. Light experiences optical losses while propagating through the FP cavity, including the optical absorption of cavity's material and the losses from recoupling into the lead-in fibre. Therefore, the signal to noise ratio decreases with cavity length increase. The decreasing of fringe visibility could result in a reduced signal-to-noise ratio (SNR), and thus, a limited maximum cavity length [107, 136].

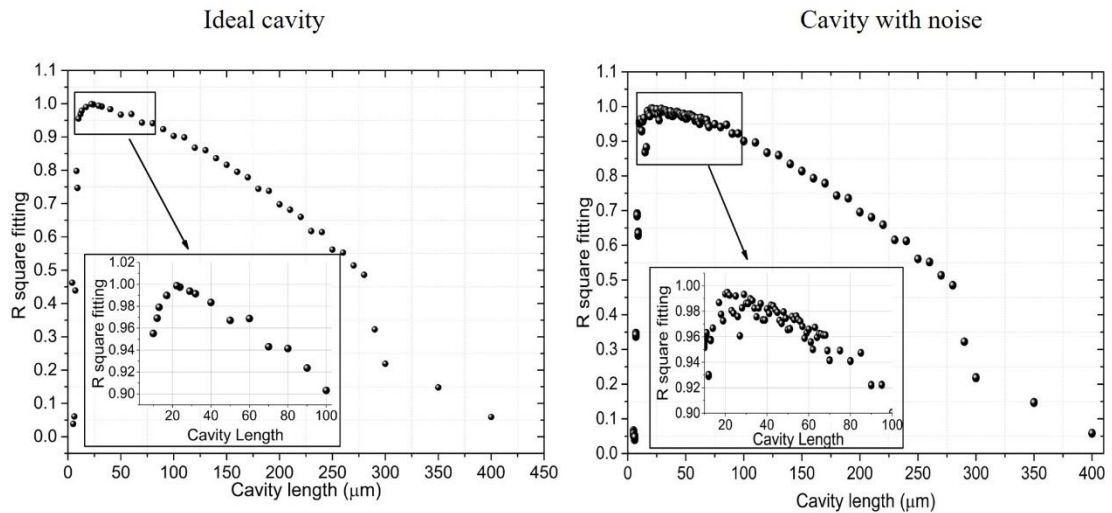


**Figure 58.**  $R^2$  fitting versus cavity length in micrometres. The left graph corresponds to an ideal no-noise cavity, while the right graph corresponds to a cavity where noise was introduced. The insets depict the cavity lengths which exhibited on a theoretical model fitting quality more than 0.9.

Through theoretical calculations we estimated the optimum cavity length of a Fabry-Pérot sensor, defined by investigating the quality of a sinusoidal fitting function to sensor's spectrum. The sinusoidal fitting function emanates from the analysis of the sensor's spectrum, according to the data analysis routine in **Chapter 2**. On the theoretical model, built on LabVIEW software, the sinusoidal fitting function is created by the extracted values of frequency, phase and amplitude after the single tone frequency detection is applied on the raw data sinusoidal spectrum. The raw data sinusoidal spectrum is co-plotted with the sinusoidal fitting function from which the quality of the fitting is calculated as  $R^2$ . The quality of the fitting ( $R^2$ ) for a variety of Fabry-Pérot cavity lengths, starting from  $2\mu\text{m}$  up to  $400\mu\text{m}$ , was calculated. The best fitting should have an  $R^2$  value of 1, however for  $R^2$  values above 0.9 the fitting is considered useful for our data analysis. The estimation of  $R^2$  has been investigated, with respect to cavity length, for an ideal cavity (a cavity without any noise introduced with a fringe visibility of 1) and a cavity where white noise has been introduced. The white noise which has been applied had a standard deviation of  $\pm 0.1$  on the raw data sinusoidal spectrum, which drops the fringe visibility to 0.9. **Figure 58** demonstrates the optimum cavity length of a Fabry-Pérot sensor in the insets, where the quality of the fitting is given by  $R^2$ . The left plot of **Figure 58** represents the  $R^2$  of an ideal cavity with fringe visibility 1. No white noise at the modelled sinusoidal spectrum of the sensor was introduced. The right plot of **Figure 58** corresponds to a cavity after introducing white noise in the sinusoidal spectrum. According to **Figure 58**, a Fabry-Pérot sensor with cavity length range between  $20\mu\text{m}$  and  $80\mu\text{m}$  gives very good quality fitting results, as the  $R^2$  sits above 0.94. For cavity length above  $100\mu\text{m}$  the quality of the fitting is dramatically reduced.

A longer cavity has shorter fringe spacing therefore the refractive index change of the fibre required to make a  $2\pi$  phase shift is smaller than that for a short cavity. **Figure 59** shows the theoretical simulated spectra for 4 different cavity FP sensors, where 4 fringes with  $20\text{nm}$  spacing between them consist a  $40\mu\text{m}$  sensor while 8 fringes with  $10\text{nm}$  spacing consist an  $85\mu\text{m}$  sensor. As a result, the phase shift corresponding to a temperature change increases for longer cavity lengths indicating higher sensitivity.

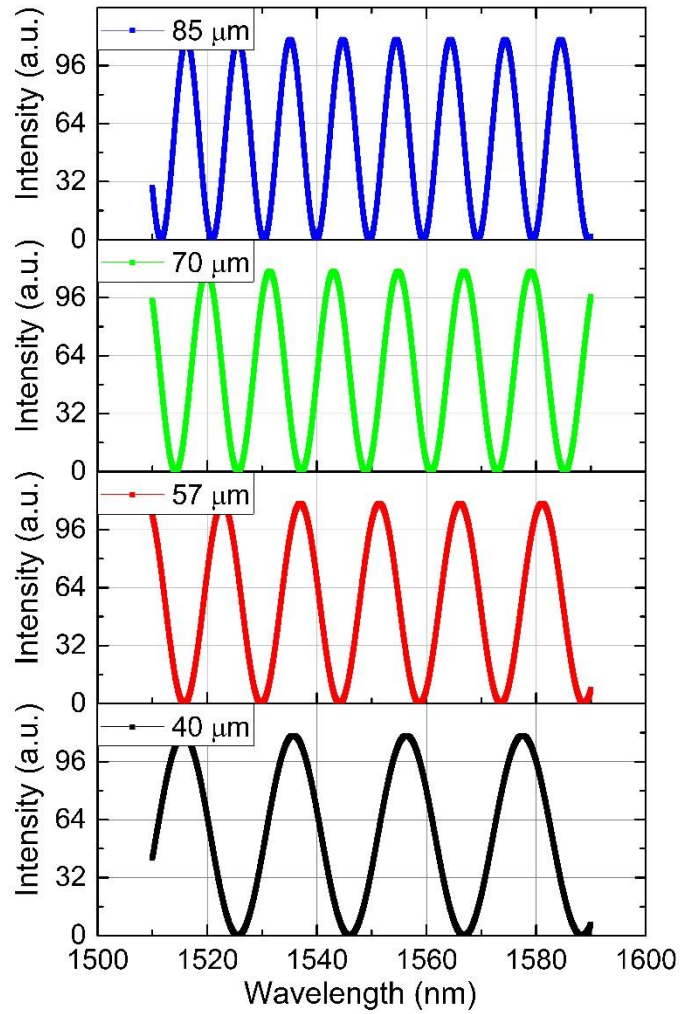


**Figure 59.** *Modelled spectra of different cavity sensors. Y-axis displays the intensity in arbitrary units while in the x-axis is displayed the wavelength in nanometres.*

### 4.3 Ge-doped (SMF28 ultra) Fabry-Pérot sensor

This section, will present the annealing cycles, thermal cycles, and high temperatures stability studies of sensors whose sensing element was manufactured by a Ge-doped core. Both type 1 and type 2 Fabry-Pérot sensors long-term thermal characterization studies are presented in the next sections investigating their phase response suitability for temperature measurements up to 1150°C.

#### 4.3.1 Annealing and Thermal Cycling of Ge-doped core Fabry-Pérot sensors

Each sensor is initially subjected to an annealing cycle and several thermal cycles, to relieve the optical fibre from residual internal stresses. The annealing process causes reduction of the local stresses, leading to more homogenous fibres which is critical to their durability. These local stresses are caused by the different materials of the core and the cladding during the optical fibre drawing of their manufacturing process. An inadequately annealed optical fibre is likely to crack or shatter when subjected to

relatively abrupt temperature change. For the annealing and thermal cycling section, there were chosen some representative sensors from each type and sensing element to present their phase response versus time and temperature.

**Figure 60** depicts the annealing cycles performed with the sensors before the phase stability tests. The annealing cycles (up photo-blue data) of the latter figure correspond to a 76 $\mu$ m Ge-doped cavity of type 1 Fabry-Pérot sensor. Starting from room temperature, the sensor is cycled twice up to 400°C with heating rate of 3°C/minute and cooling rate of 2°C/minute respectively. Afterwards, the same process of cycling for temperatures up to 600°C, 800°C, 900°C and finally 1000°C is repeated. In the same figure, the black data represent the phase response of the sensor which follows the temperature response changes in an identical performance.

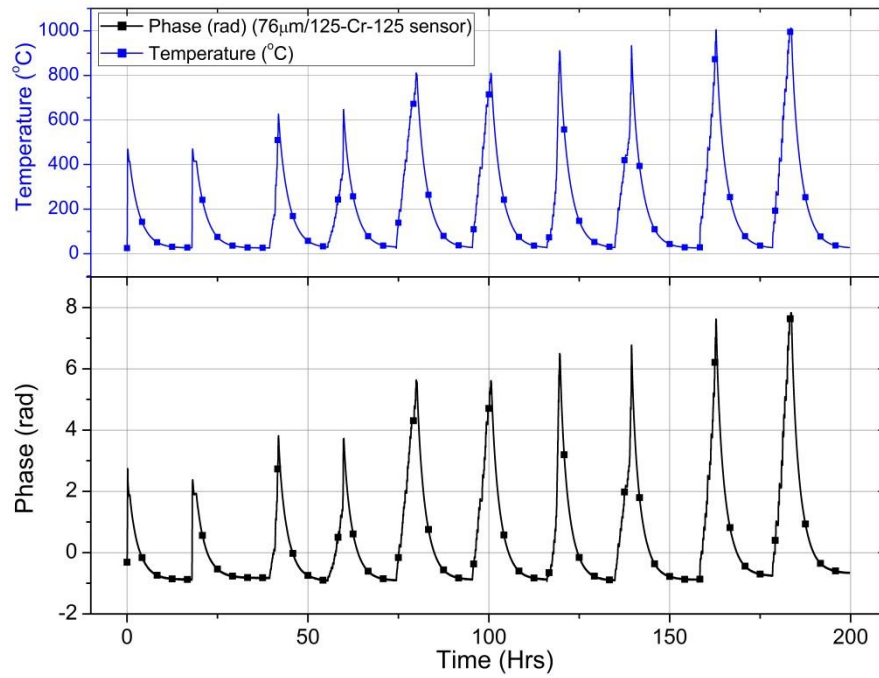


**Figure 60.** Data recorded during initial annealing process and after 9 subsequent thermal cycles of a type 1 (76 $\mu$ m) Ge-doped core Fabry-Pérot sensor with regards to time, before the stability test begins. The graphs present the temperature, recorded separately with an N-type thermocouple, and the phase response of the sensor.

Most of the sensors were also subjected to thermal cycles during the stability test and after the end of it. Through this an investigation of phase modulation phenomena and phase drifts that occurred during the stability tests was attempted. These phenomena made their appearance at the phase response cycles in the middle and the end of the stability test. An explanation of these phase modulations is that they are directly connected with dopant diffusion from core to cladding for Ge-doped sensors, and vice versa for F-doped sensors. Also, tapering phenomena that might occur along the optical



fibre especially at high temperatures. A thorough investigation of these phenomena is described in the long-term stability sections and in **Chapter 5**.

Thermal cycling of a 75 $\mu$ m Ge-doped core sensor was carried out with an initial cycle from  $\sim 26^{\circ}\text{C}$  to  $400^{\circ}\text{C}$  and back to  $\sim 26^{\circ}\text{C}$ . After each cycle, the upper temperature of the next cycle was increased, according to **Figure 60**, until it reached  $1000^{\circ}\text{C}$ . The sensor was kept at each upper temperature for approximately 20 minutes before the cooling process, to ascertain whether any drift occurs at these elevated temperatures and to ensure that a thermal equilibrium had been reached. The phase response during the thermal cycles is repeatable, as all 4 cycles are overlapping each other. This means that the annealing effects have been disappeared.

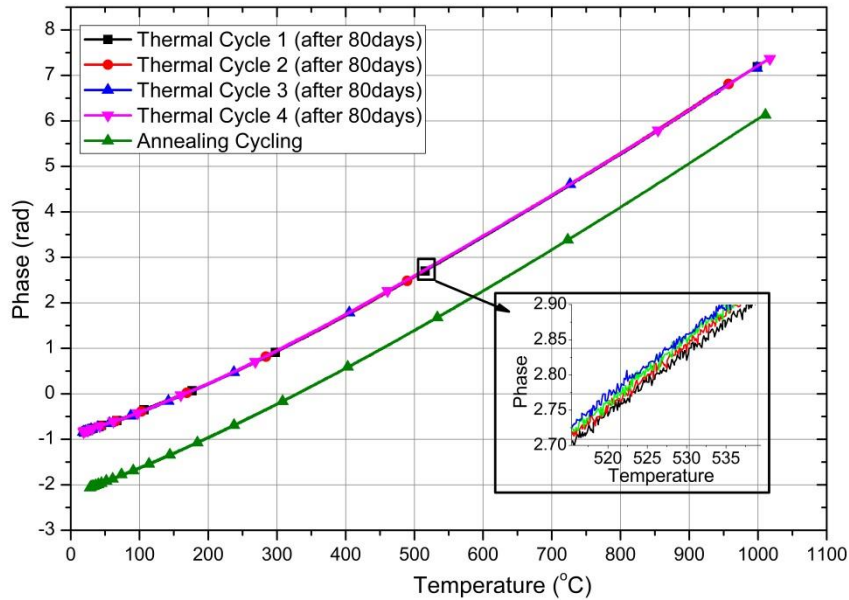


**Figure 61.** Comparison of phase data, with regards to temperature, recorded during initial annealing and after 4 subsequent thermal cycles between ambient and  $1000^{\circ}\text{C}$ , before and after the stability test. The green triangle data correspond to the annealing cycle from  $1000^{\circ}\text{C}$  to room temperature. The rest of the data, overlapping each other, are 4 thermal cycles after the sensor was tested for 80 days at temperatures above  $900^{\circ}\text{C}$ .

**Figure 61** shows the temperature calibration curve (green triangle data) obtained during the annealing cycling before the beginning of the stability test ( $\sim 80$  days) and after it. The calculated repeatability of the temperature cycling up to  $1000^{\circ}\text{C}$  is within  $\pm 4^{\circ}\text{C}$ . After approximately 80 days at temperatures above  $900^{\circ}\text{C}$ , the sensor was subjected to four thermal cycles from  $1000^{\circ}\text{C}$  to room temperature. It is obvious that the repeatability of the sensor after its stability test is robust, without any phase drifting. All cycles are overlapping each other indicating that the sensor even after 80 days has a repeatable phase response.

On the other hand, there is a phase difference, shown with a red vertical line in **Figure 61** and **Figure 62**, between the annealing cycle and the thermal cycle. The phase difference is caused by the change of the core refractive index of the sensor at temperatures up to 1100°C. The refractive index is directly connected with the phase response of sensor. In addition, the phase drift cannot be predictably quantified as it depends on the behaviour of the sensor during its stability tests as well as with the dopant of its sensing element. This phase shift effect between the annealing and thermal cycles has been noticed to Ge-doped core and F-doped depressed cladding sensors that were tested at high temperatures. It wasn't visible at pure SiO<sub>2</sub> cavity sensors though.

**Table 5. Ge-doped core SMF28 ultra sensor sensitivities**

Cavity length \ Temperature	400°C	700°C	900°C
88µm	9.35 mrad/°C	10.35 mrad/°C	11.05 mrad/ °C
75µm	8.14 mrad/°C	9.46 mrad/°C	9.98 mrad/ °C
60µm	6.69 mrad/°C	7.36 mrad/°C	8.1 mrad/°C
55µm	6.4 mrad/°C	6.97 mrad/°C	7.25mrad/°C
40µm	4.44 mrad/°C	4.95 mrad/°C	5.2 mrad/°C

**Table 5** presents the phase sensitivities of the Ge-doped core sensors that were used for the stability tests. Each sensor's sensitivity was calculated by the linear fitting slope at three indicative temperatures. The non-linearity of the phase response can be justified from this table as at higher temperatures the sensitivity becomes larger according to section **4.1**.



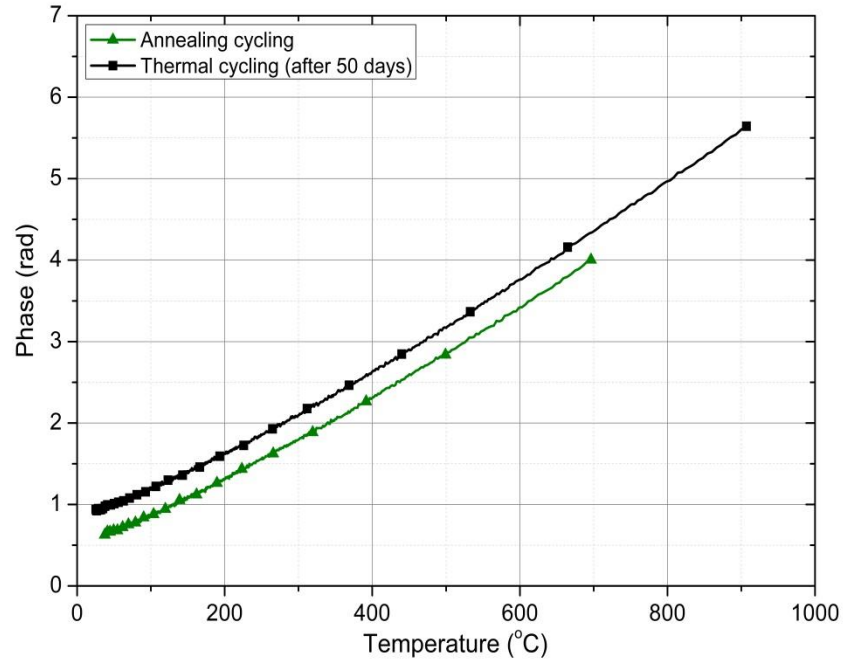


**Figure 62.** Data recorded during initial annealing process and after 1 subsequent thermal cycle with regards to temperature of a 55µm Ge-doped core Fabry-Pérot sensor. Annealing (green triangle data) occurred before the stability test while thermal cycle (black square data) after the stability test.

In **Figure 63** and **Figure 64** phase modulations make their appearance showing a periodic behaviour. During the thermal cycle only, the phase response has a modulated behaviour, which is repeatable at both cooling and heating process. Similarly, as with the previous sensors these figures present both annealing cycle and a thermal cycle, before and after the stability test.

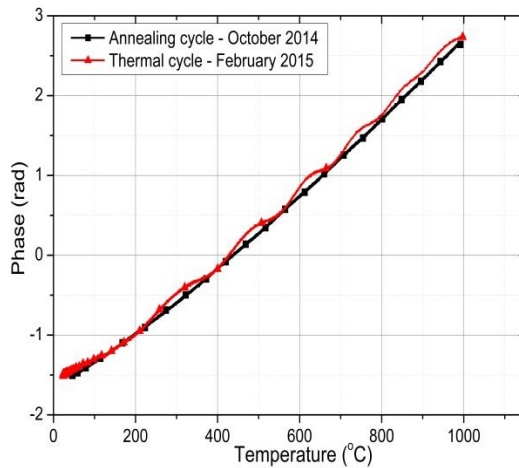


**Figure 63.** Annealing (black square data) and thermal cycle (red triangle data) comparison of a Ge-doped core 40µm cavity sensor. Phase modulations to the thermal cycle after the stability test end, made their appearance.

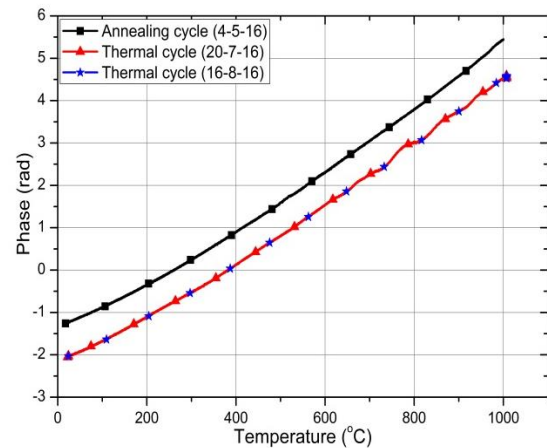


**Figure 64.** Annealing (black square data) and thermal cycle (blue star and red triangle data) comparison of a Ge-doped core 60µm cavity sensor. Phase modulations to the thermal cycle after the stability test end, made their appearance.

A 2<sup>nd</sup> order polynomial function was fitted to the phase response of annealing and thermal cycle of **Figure 63** and **Figure 64**. The residuals presented in **Figure 65** correspond to the sensor of **Figure 63**, while the residuals of **Figure 66** correspond to the sensor of **Figure 64**. The residuals of the annealing cycle (black square data in **Figure 65**, **Figure 66**) demonstrate a variation which is common to all the annealing cycles of the sensors. This variation would be eliminated if a higher order polynomial fit was used, but fused silica's thermo-optic coefficient is 2<sup>nd</sup> order dependent on temperature [55], which means that there is not a physical explanation for the use of a higher order fitting function. On the other hand, the residuals of the thermal cycles (red triangle data in **Figure 65**, **Figure 66**) present a uniform phase modulation of roughly  $\pm 0.05$  radians in 800°C range (**Figure 65**) and  $\pm 0.07$  radians in 400°C range (**Figure 66**).

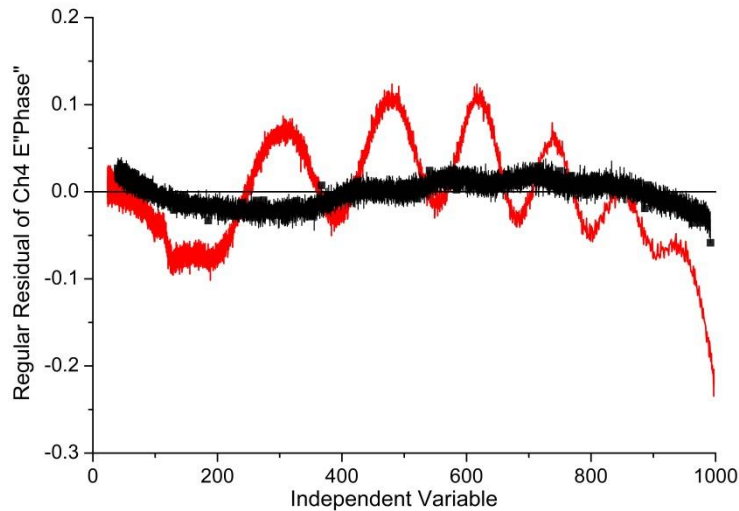


**Figure 65.** Residuals of annealing (black square data) and thermal (red triangle data) cycle after fitting a 2<sup>nd</sup> order polynomial to sensor of **Figure 63**.

These phase modulations come from a second order cavity that interferes with the signal of the fundamental FP cavity. Additionally, the second order cavity is correlated with expanding tapering phenomena of the core radius, caused by the germanium diffusion from the core to the cladding at elevated temperatures (described in details in **Chapter 5**). These tapering phenomena cause a thermal enlargement of the core radius, increasing the core diameter and consequently its mode field diameter (MFD) [76]. In this way, a second order mode makes its appearance causing this characteristic modulated phase performance. These modulations make their appearance during the thermal cycles, after the sensors have been heated at temperatures up to 1100°C for long periods of time.

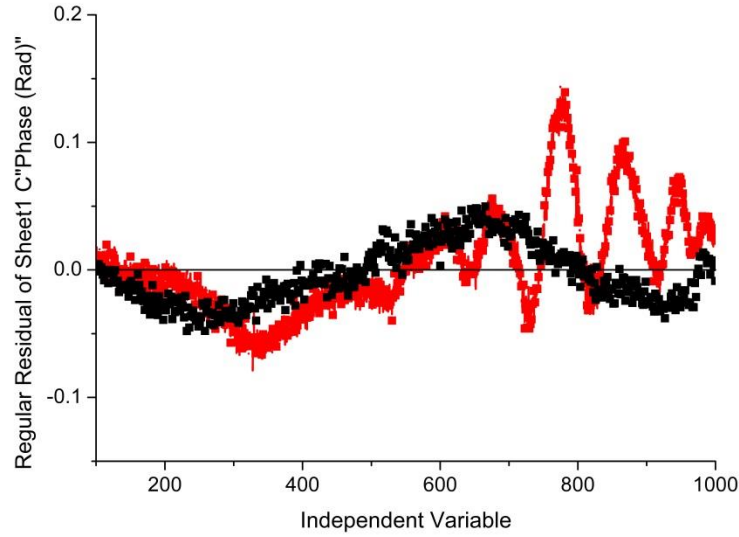


**Figure 66.** *Residuals of annealing (black square data) and thermal cycle (red triangle data) cycle after fitting a 2<sup>nd</sup> order polynomial to sensor of Figure 64.*

#### 4.3.2 Long-Term Stability Tests of Ge-doped core Fabry-Pérot sensors

The period of the stability tests varied from 50 days to 100 days. We normally categorize the long-term stability tests in stability cycles, starting and returning to i.e. 900°C after the maximum temperature is reached.

The temperature resolution of each sensor is calculated by analysing the slope and the peak to peak noise level in the calibration curve. All the Ge-doped sensors in this section showed a temperature resolution approximately <5°C for a 1 sec measurement time and <2°C for a 10-data points measurement average (~1Hz). The maximum temperature reached at these experiments was 1150°C due to temperature limitations of the furnace. In addition, at temperatures beyond 1200°C the sensor decays and crystallization phenomena might take place. The result would be optical fibre's signal degradation due to crystal growth. This degradation could be caused by crystallization of the fused silica changing permanently its structural phase [65, 67, 137].

##### 4.3.2.1 Sensor Type 1: 125µm-Cr-125µm

**Figure 67** depicts a long-term stability test of 85 days of the SMF28 sensor, with a noise level less than 3°C at 1050°C. The sensor has been subjected to two stability test cycles from 900°C up to 1100°C. Initially, at the first stability cycle, the sensor shows a drift (~4°C) at 1045°C, as it is portayed in **Figure 68(a)**. Then in the same cycle, in **Figure 68(b)**, it can be seen the large drift (~22°C) of the sensor during the cooling down process. At the second cycle, the sensor exhibits a negligible drift over 4 days

(**Figure 68(c)**), while at the cooling down process on the same cycle (**Figure 68(d)**) the sensor starts drifting again ( $\sim 7^\circ\text{C}$ ). These values can be compared with the furnace's temperature drift, measured by a N-type thermocouple, which is roughly  $1.5^\circ\text{C}$  at all the stability graphs below (blue data in **Figure 67**). The sensor's drift is caused by the change of the refractive index core of the fibre, apparently due to the fact that the germanium dopant is diffusing to the cladding [138].

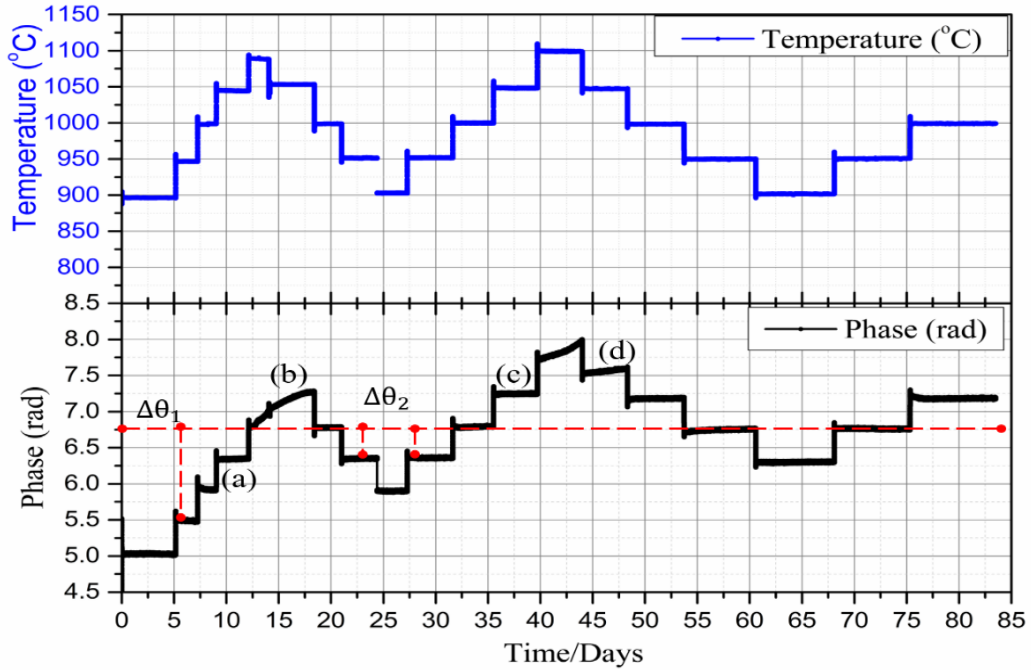


**Figure 67.** Long term stability test of the  $75\mu\text{m}$  Ge-doped SMF28 ultra FP sensor. Each letter is referred to the stability test of Figure 68. The red dashed horizontal line indicates the phase at  $900^\circ\text{C}$  of the third stability cycle, while the red vertical dashed lines indicate the phase difference at  $900^\circ\text{C}$ , between the stability cycles.

Throughout the long-term stability tests, it was noticed that the phase values of the sensor at  $1050^\circ\text{C}$  during heating (1<sup>st</sup> and 2<sup>nd</sup> cycles), cooling (1<sup>st</sup> and 2<sup>nd</sup> cycle) have an escalating variation. This happens due to annealing processes that took place at higher temperatures, as well as there is a relaxation time until the sensor will be stabilized. When the sensor is exposed to high temperatures such as  $1050^\circ\text{C}$  a permanent change of the refractive index, causes the phase difference before and after the heating. In conclusion, stability of the sensor can be observed during the heating up procedure of each cycle (**Figure 68(a)** and **Figure 68(c)**), by avoiding abrupt temperature changes.

A red dashed line in **Figure 67**, represents a baseline, showing the phase value at the end of 2<sup>nd</sup> stability cycle at  $950^\circ\text{C}$ .  $\Delta\theta_2$  is approximately 0.45 radians and is the phase difference of the 3<sup>rd</sup> and 2<sup>nd</sup> cycle while  $\Delta\theta_1$  is approximately 1.25 radians and represents the phase difference between the 3<sup>rd</sup> and 1<sup>st</sup> cycle. The same analysis can be applied at other temperatures such as  $900^\circ\text{C}$  and  $1000^\circ\text{C}$ . The phase difference from the

baseline indicates that the refractive index of sensing element's core is changing throughout the temperature variations of the stability test, justifying in this way the germanium diffusion which causes the phase drifting. The phase value at 950°C, at the end of 1<sup>st</sup> stability cycle (day 23) has no difference with the phase value at the beginning of the 2<sup>nd</sup> stability cycle (day 30). The same is applied for day 20 and day 33 which represent the phase response at 1000°C. It seems that when the sensor is subjected to the cooling process of the stability cycle, its phase response doesn't present unpredictable changes. A conclusion that can be made is that the phase difference becomes larger when the sensor was tested earlier at temperatures above 1000°C.

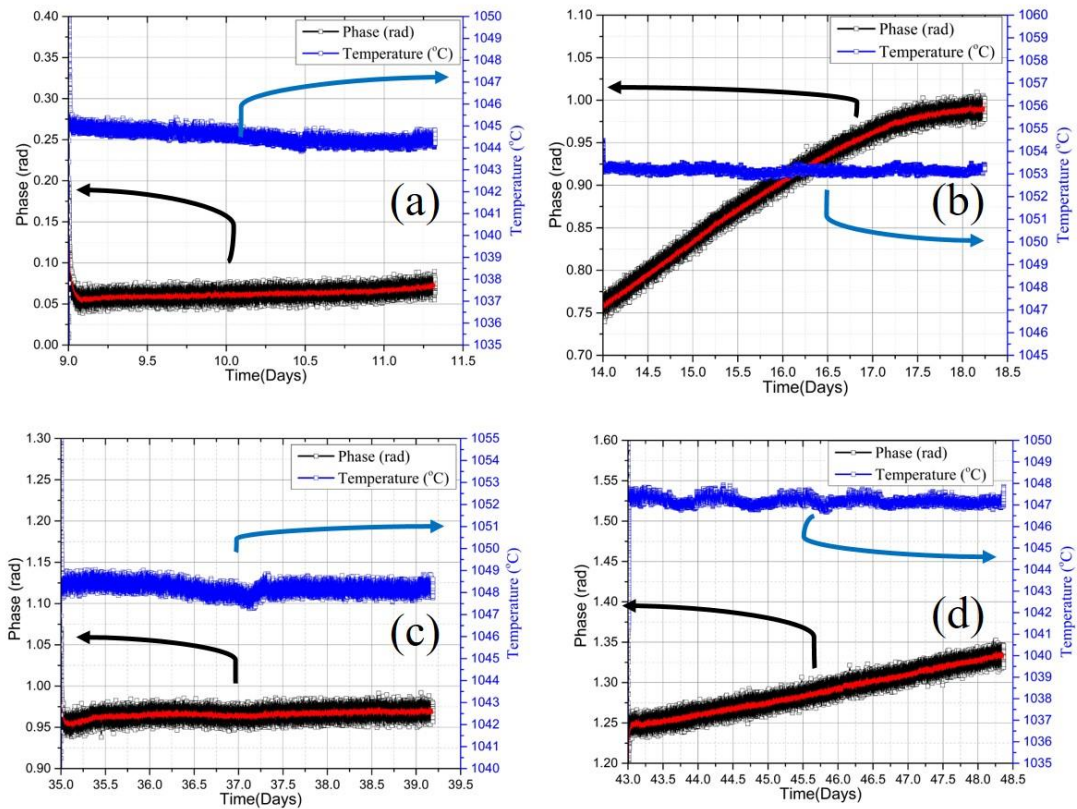


**Figure 68.** Expanded stability test views of the 75μm Ge-doped FP sensor at 1045°C (a), 1053°C (b), 1048°C (c) and 1048°C (d). Each letter corresponds to the same letter in Figure 67. The red lines represent a 10-floating point averaging.

**Figure 69** presents the stability test, lasted for 100 days, of a 60μm Ge-doped FP sensor at which both stability test cycles begin at 900°C and rise to 1050°C before returning to 900°C. The upper left corner of the same figure indicates the calculated temperature that corresponds to 0.5 radians. The temperature comes from the sensitivity of the sensor at 1000°C. This temperature indication, shows an estimation of the sensor's drift in Celsius degrees.



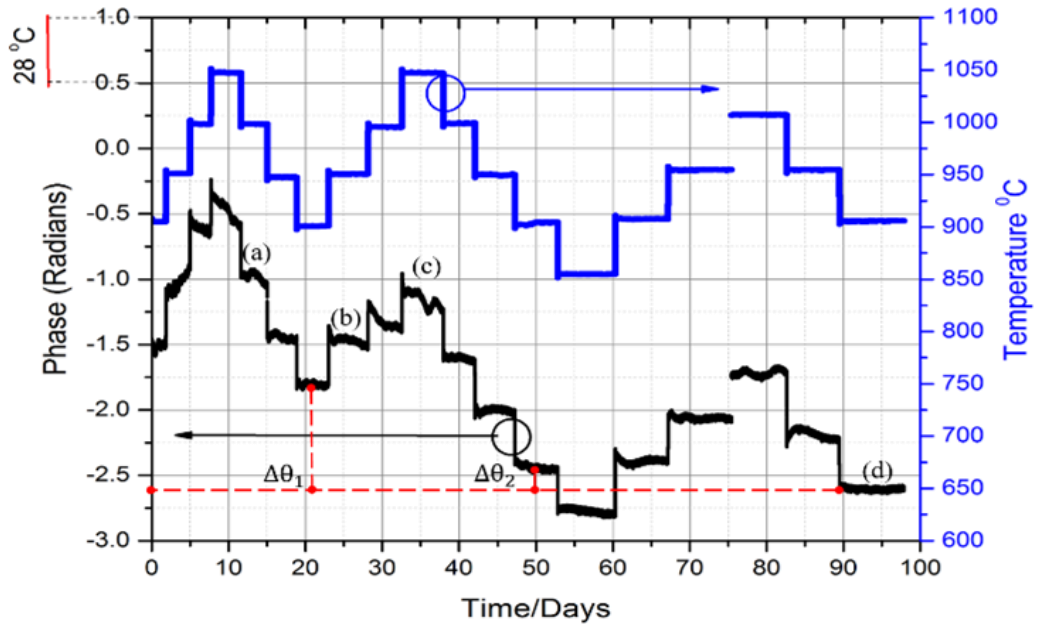


**Figure 69.** Long term stability test of Ge-doped SMF28 ultra FP sensor (60μm). Each letter is referred to the stability test of Figure 70. The red dashed horizontal line indicates the phase at 900°C of the third stability cycle, while the red vertical dashed lines indicate the phase difference at 900°C, between the stability cycles.

The phase value of the FP sensor in **Figure 69** (red dashed horizontal line) that the phase value of the sensor has a distinctive difference compared with the phase at the same temperature of the previous cycle. Again, to illustrate this example it was added a red dashed line at **Figure 69** showing the phase differences of Ge-doped FP sensor at 900°C at the end of the 1<sup>st</sup> cycle, the 2<sup>nd</sup> cycle and the 3<sup>rd</sup> cycle. The baseline corresponds to the 3<sup>rd</sup> cycle's phase value at 900°C.  $\Delta\theta_2$  is approximately 0.25radians and is the phase difference of the 3<sup>rd</sup> and 2<sup>nd</sup> cycle while  $\Delta\theta_1$  is approximately 0.85radians and represents the phase difference between the 3<sup>rd</sup> and 1<sup>st</sup> cycle. The same analysis can be applied at other temperatures such as 950°C and 1000°C. Its phase difference at 900°C and 950°C between the end of the 1<sup>st</sup> cycle and the beginning of the 2<sup>nd</sup> stability cycle is obviously negligible. Again, germanium diffusion has a large impact at the phase stability of the sensor. This sensor proved to be stable only at 900°C, after completing two stability cycles.

**Figure 70** demonstrates the expanded stability views of the sensor at various temperatures. The sensor exhibited a minimum temperature drift of less than 3°C, at 900°C (**Figure 70(d)**), at the end of the 3<sup>rd</sup> stability test cycle. For temperatures above 900°C showed significant drifting as it can be seen in at **Figure 70(a)**, **Figure 70(b)**, **Figure 70(c)** with temperature drifts 13°C, 7°C and 27°C, respectively.

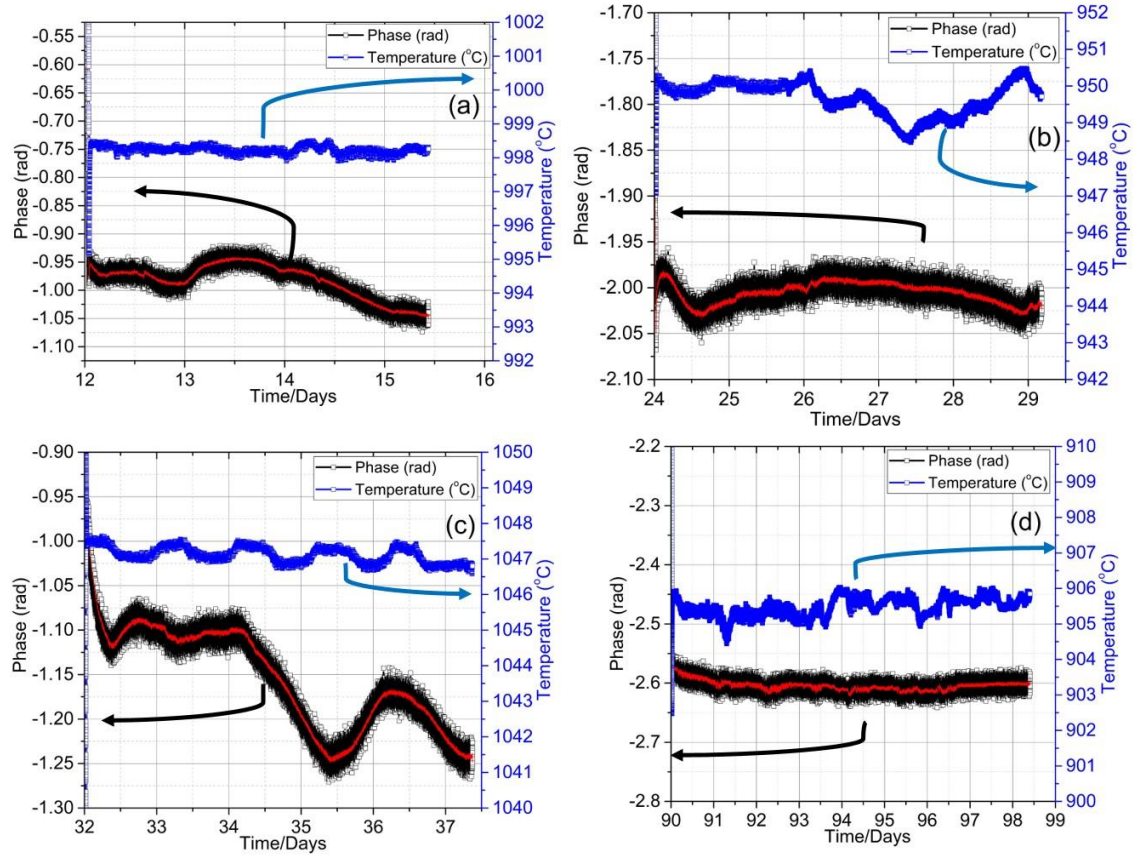


**Figure 70.** Expanded stability test views of the Ge-doped FP sensor at 1000°C (a), 950°C (b), 1050°C (c) and 900°C (d). Each letter corresponds to the same letter in Figure 69. The red lines represent a 10- floating point averaging.

**Figure 71** and **Figure 72** present the long-term stability test of two Ge-doped FP sensors with 55μm and 40μm cavity lengths, respectively. Both sensors didn't complete a full stability cycle, instead they stayed at temperatures above 950°C up to 50 days and 95 days, respectively. Over this long-term stability test it can be seen in temperature recording (blue data), perturbations of 5°C for both sensors due to environmental variations. The 55μm FP sensor proved to be stable at temperatures up to 1100°C, before start drifting at 1050°C. In **Figure 73** an expanded view of its stability at 1100°C, showing a temperature drift of 6°C over 14 days, is depicted.

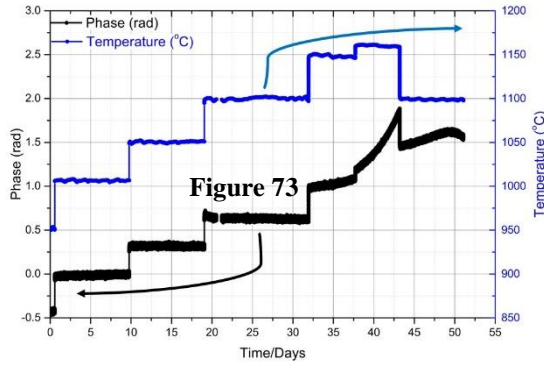


**Figure 71.** Long term stability test for 50 days of a 55μm Ge-doped SMF28 ultra FP sensor.

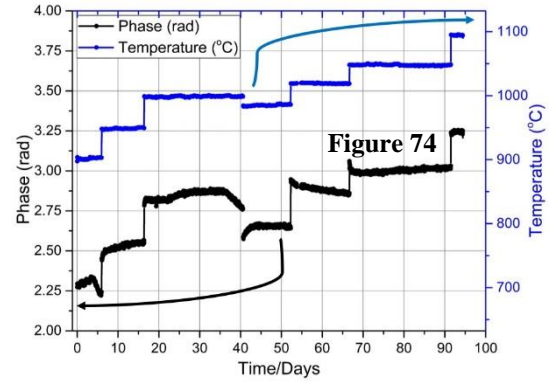


**Figure 72.** Long term stability test for 95 days of a 40μm Ge-doped SMF28 ultra FP sensor.

**Figure 73** shows an expanded phase stability view of the 55μm FP sensor in showed a peak to peak noise level which is 14°C without averaging and 5°C after a 10-point averaging. On the other hand, the 40μm sensor presented a peak to peak noise level of 10°C without averaging and 3°C after a 10-point averaging. **Figure 74** depicts the expanded phase stability view of the 40μm FP sensor which lasted 22 days. The response of the sensor at this temperature, exhibited a temperature drift of less than 4°C, while at the other temperatures of the stability test the sensor showed lack of stability.

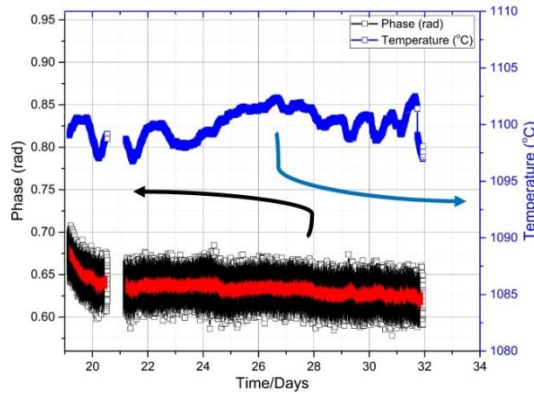


**Figure 73.** Expanded stability test view of the 55μm Ge-doped FP sensor for 14 days at 1100°C.

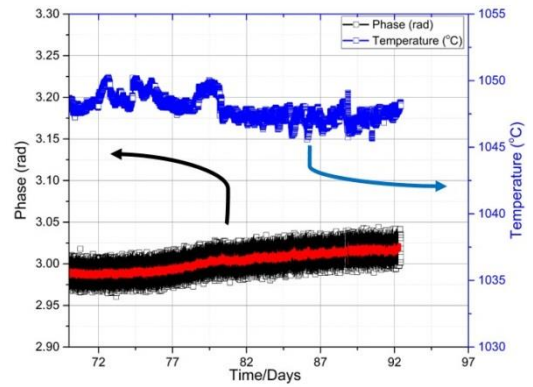


**Figure 74.** Expanded stability test views of the 40μm Ge-doped FP sensor for 22 days at 1050°C.

#### 4.3.2.2 Sensor Type 2: 125μm-80μm-50μm-Cr-50μm (Stepped)

A partial aim of this work was to encapsulate the sensors to avoid strain transfer effects from the surrounding metallic medium, and be embedded in metallic structures for temperature monitoring without any external strain influences. Therefore, in another approach we manufactured the type 2 stepped diameter Ge-doped Fabry-Pérot sensors which consist of Ge doped optical fibres with different diameters spliced together (3.5.2).



**Figure 75** presents the long-term stability test of type 2 (stepped) Ge-doped core Fabry-Pérot consisted by two stability test cycles. The first stability cycle starts at 950°C, reaches a maximum temperature of 1150°C before returning to 700°C. The second stability test cycle starts at 700°C continuing up to 1150 °C and then returning to 750°C, with step increments of 50°C. A significant drift of the sensor response above 1050°C, can be observed. After this annealing, the sensor response shows good long-term stability at high temperatures up to 1000°C, which is below the annealing temperature.

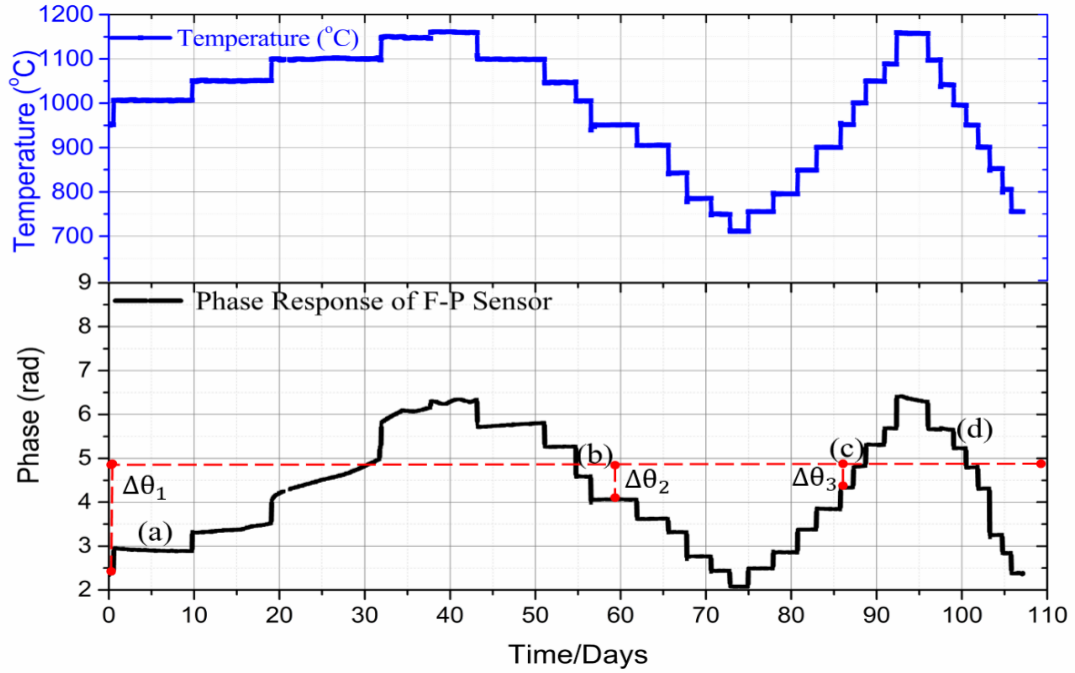


**Figure 75.** Long term stability test of type 2 (stepped) Ge-doped SMF28 ultra FP sensor (75μm). The red dashed horizontal line indicates the phase at 900°C of the third stability cycle, while the red vertical dashed lines indicate the phase difference at 900°C, between the stability cycles.

The sensor response improved its stability at high temperatures during the second thermal stability cycle. The red dashed line was inserted again as a baseline indicating the phase value of the sensor at 950°C after the end of 2<sup>nd</sup> cycle. Hence,  $\Delta\theta_1$ ,  $\Delta\theta_2$  and  $\Delta\theta_3$  with values 2.5 radians, 0.9 radians and 0.6 radians respectively, show the phase differences at the same temperature throughout the stability test of different stability cycles. The sensing element of this type 2 sensor has 50μm diameter, and as it is obvious from the phase differences  $\Delta\theta_1$ ,  $\Delta\theta_2$  and  $\Delta\theta_3$  the germanium dopant diffusion affects its stability.

**Figure 76** shows the stability improvement of the sensor at 1000°C during these two stability cycles where **Figure 76(a)** represents the phase and temperature at 1000°C over time during the temperature increase step of 1<sup>st</sup> cycle. Similarly, **Figure 76(b)**

represents 1<sup>st</sup> cycle decrease, **Figure 76(c)** represents 2<sup>nd</sup> cycle increase and **Figure 76(d)** represents 2<sup>nd</sup> cycle decrease. The inside red narrow curve at each graph represents the noise level of the sensor after a 10-point averaging where the noise is reduced to one third of the original noise. The peak to peak noise level of the sensor in **Figure 76** is <2°C after the 10-point averaging and over time of its operation. The sensor exhibited high stability at 1000°C especially after being annealed at temperatures above 1050°C, showing a temperature drift of 7°C in **Figure 76(a)** and without drifting in the other graphs of **Figure 76**.

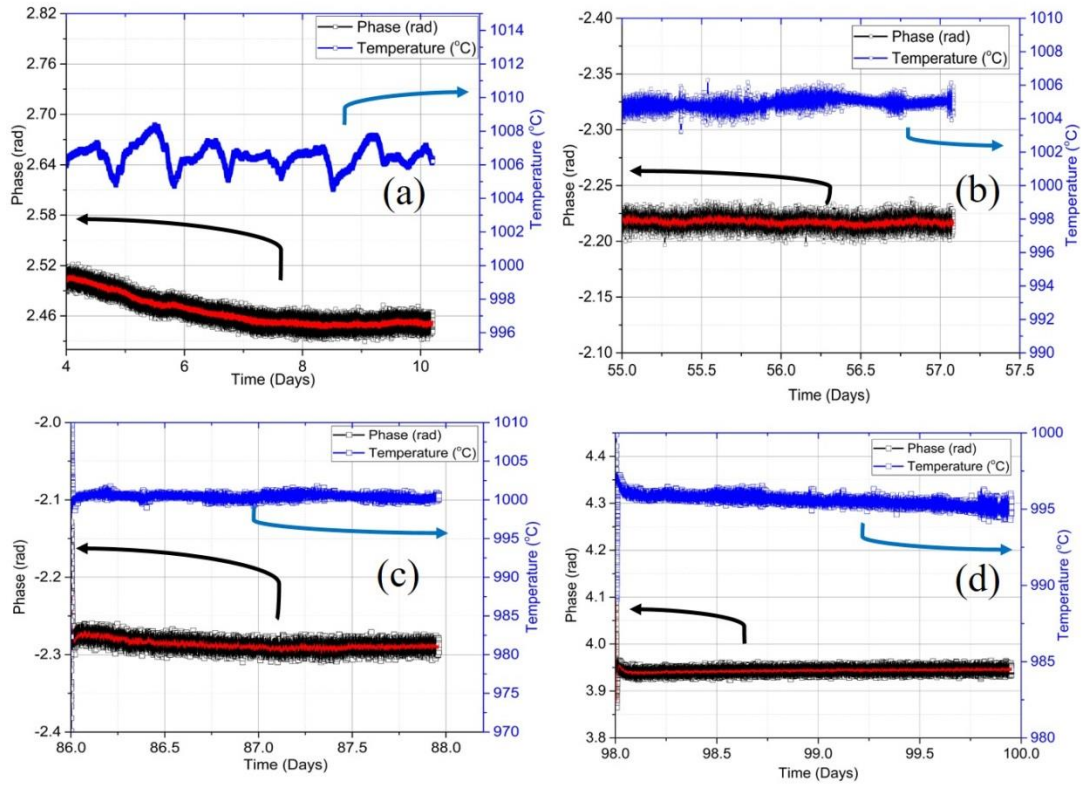


**Figure 76.** Expanded stability test views of the type 2 (stepped) 75 $\mu$ m Ge-doped FP sensor at 1000°C during different stages of the stability analysis routine followed, (a) 1<sup>st</sup> cycle increase, (b) 1<sup>st</sup> cycle decrease, (c) 2<sup>nd</sup> cycle increase and (d) 2<sup>nd</sup> cycle decrease. Each letter corresponds to the same letter in Figure 75. The inside red narrow curve represents a 10-floating point averaging.

In this section, long-term high temperature stability results of a series of Ge-doped core FP sensors were presented. At temperatures above 1050°C the sensors showed unpredictable phase drifts. Instead, the sensors exhibited in common some characteristics during their stability tests. The phase difference between the same temperatures of a different stability cycle was one of them and visible to all Ge-doped sensors. This phase difference can be seen at the phase response, with regards to temperature, between the annealing and thermal cycle of the sensor as well. A correlation of the phase difference with the permanent change of core's refractive index of the sensor due to dopant diffusion, from core to cladding, can be made.

Furthermore, the results show that the Ge-doped FP sensor can be used for reliable temperature measurements for 5 days up to 1050°C with an accuracy better than 5°C. The upper operation limit of a fused silica based sensor should be below its annealing point temperature, 1150°C, for reliable measurement. Normally, the higher stability is achieved when a stability test cycle was preceded reaching up to the annealing point of the sensor.

#### 4.4 F-doped depressed cladding (F-SM1500SC-P) Fabry-Pérot sensor

After investigating the phase stability behaviour of Ge-doped core sensing element sensors, an examination of the behaviour of the sensors made by an F-doped depressed cladding sensing element, was carried out. Their annealing cycles, thermal cycles and high temperatures stability are presented in this section.

##### 4.4.1 Annealing and Thermal Cycling of F-doped depressed cladding Fabry-Pérot sensor

The F-doped sensors were subjected to three annealing cycles up to 1000°C, where they stayed at this temperature for approximately 30 minutes before they cycle down to room temperature. The same process was followed for the thermal cycles after the end of the stability test which lasted for 47 days. Their annealing and thermal cycles are presented in **Figure 77** and **Figure 78**. The black data correspond to the cooling down process before the stability test begins, while the red data after the end of the stability test.

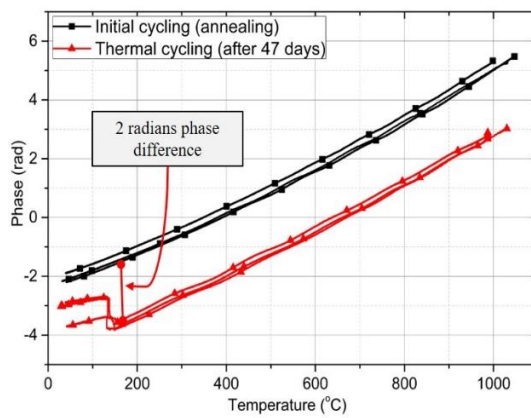


**Figure 77.** Phase response cycle comparison of the 69 $\mu$ m F-doped depressed cladding Fabry-Pérot sensor.

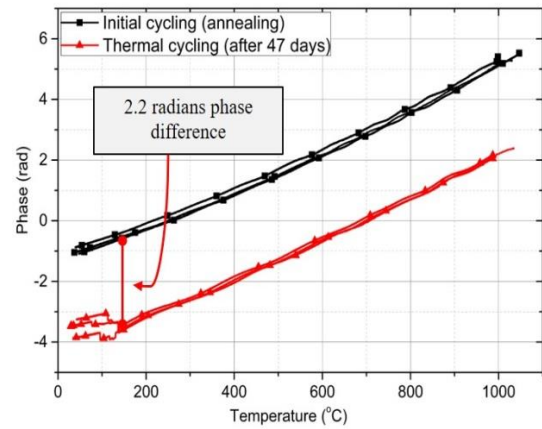


**Figure 78.** Phase response cycle comparison of the 59 $\mu$ m F-doped depressed cladding Fabry-Pérot sensor.

As it can be seen in both figures the phase difference is dominating with a phase value of approximately 2 radians to both sensors. The phase modulations were observed in both annealing and thermal cycles of F-doped sensors as well. Similarly, with the phase modulations at the thermal cycles of Ge-doped core sensors, a postulation that the fluorine dopant diffuses from the cladding towards the core in the sensing element causing these phase modulations, can be made. A second order cavity is again interfering with the fundamental cavity of the sensor through the fast fluorine dopant diffusion, increasing the radius and the mode field diameter of the core [75]. The interesting part is that these phase modulations made their appearance at both annealing and thermal cycles. This is expectable as fluorine element ( $Z=9$ ) is lighter than germanium ( $Z=32$ ) and diffusion of germanium from the core to the cladding occurs with a lower rate than the diffusion from cladding to the core of fluorine [139]. The outcome is a fast fluorine diffusion in the sensing element introducing a 2<sup>nd</sup> order mode cavity in the sensing element before the stability tests beginning.

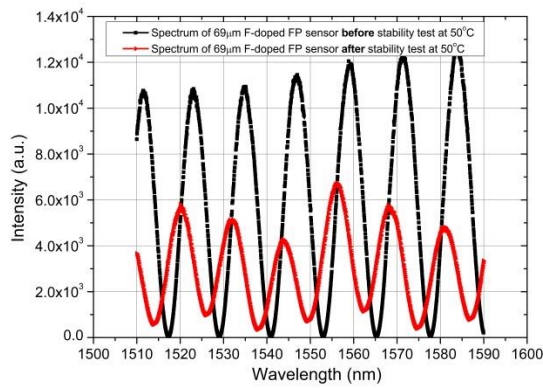


**Figure 79.** Co-plotted spectra of 69µm F-doped sensor at 50°C before (black square data) and after the stability test (red triangle data).

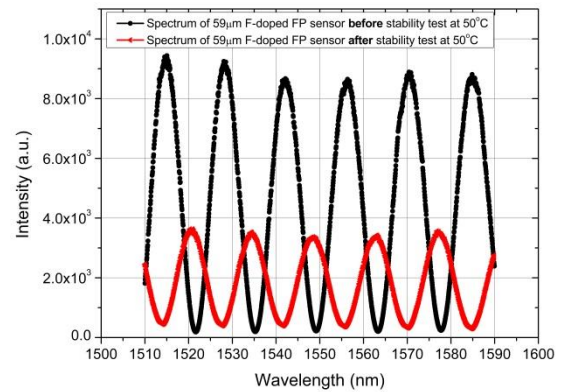


**Figure 80.** Co-plotted spectra of 59µm F-doped sensor at 50°C before (black square data) and after the stability test (red triangle data).

In addition, the thermal cycles (red data) for both **Figure 77** and **Figure 78** presented an abrupt phase shift for temperatures below 150°C. The spectra of the sensors at 50°C were recorded before and after the stability test temperature, presented in **Figure 79** and **Figure 80**. As it can be seen in the same figures, at both sensors there is a 20% loss at their spectra intensity. The diffusion of the fluorine takes place only in the sensing cavity length, as the rest of the sensor is the waveguiding fibre consisted by an SMF28 ultra. The sensor sits at 17cm length in the furnace meaning that the waveguiding fibre (Ge-doped core) experiences diffusion as well, but with a much lower rate than the sensing element. The fast fluorine diffusion creates a significant

difference at the diameters of the sensing element core and the waveguiding fibre's core, increasing consequently the cooling loss into the lead-in waveguiding fibre.

#### 4.4.2 Long-Term Phase Stability Tests of F-doped depressed cladding Fabry-Pérot sensors

Both F-doped FP sensors with cavity lengths  $69\mu\text{m}$  and  $59\mu\text{m}$ , were tested in a temperature range from  $850^\circ\text{C}$  up to  $1050^\circ\text{C}$  for approximately 60 days. Their stability tests, as portrayed in **Figure 81** and **Figure 82**, indicated inadequate stability at all temperatures due to the high rate of diffusion of the fluorine from the cladding into the core. However, their phase responses throughout the stability test are apparently identical. In these stability tests, it wasn't introduced a phase baseline, as it is obvious from **Figure 81** and **Figure 82** that there wasn't any phase stability at none of the temperatures the sensors were subjected.

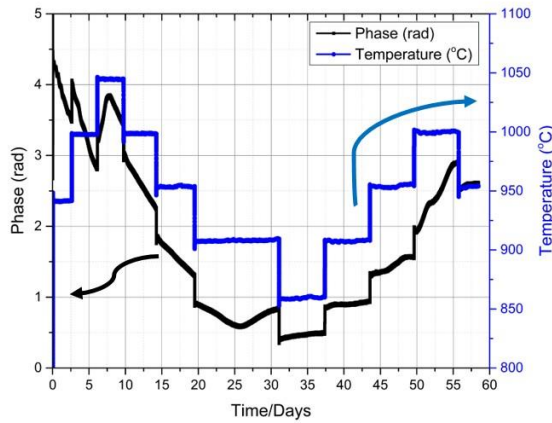


**Figure 81.** Long-term stability test (~60 days) of a  $69\mu\text{m}$  F-doped depressed cladding Fabry-Pérot sensor.

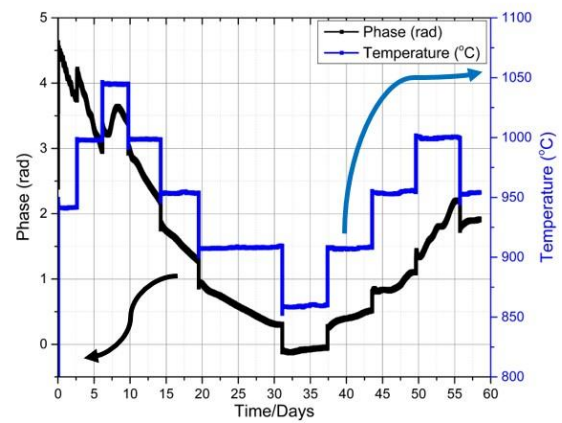


**Figure 82.** Long-term stability test (~60 days) of a  $59\mu\text{m}$  F-doped depressed cladding Fabry-Pérot sensor.

The sensors were subjected to two stability test cycles, from  $850^\circ\text{C}$  to  $1050^\circ\text{C}$ , before returning. Their temperature drift varied between  $100^\circ\text{C}$  and  $160^\circ\text{C}$  for both sensors, over the stability cycle range. The drift in temperature Celsius degrees is calculated from the phase drift and the sensitivity of the sensor at a specific temperature. After the first stability test cycle both sensors showed minimum temperature drift, less than  $10^\circ\text{C}$  at  $850^\circ\text{C}$ , but during the second stability cycle the phase drift escalated again.



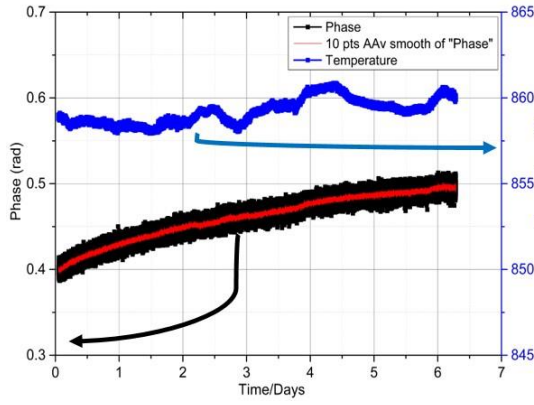


**Figure 83.** Stability test of 69 $\mu\text{m}$  F-doped sensor at 850°C. The temperature drift is roughly 10°C. The red lines represent a 10-floating point averaging.

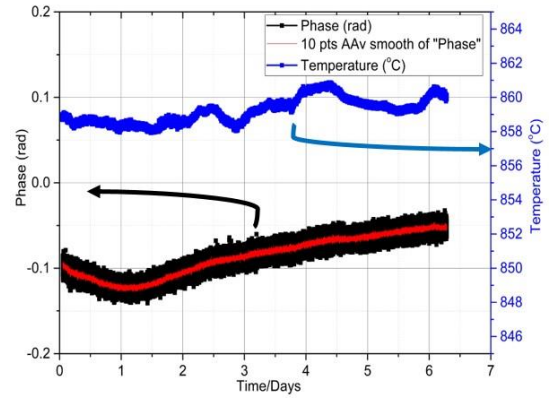


**Figure 84.** Stability test of 59 $\mu\text{m}$  F-doped sensor at 850°C. The temperature drift is roughly 7°C. The red lines represent a 10-floating point averaging.

It seems that for temperatures below 950°C, the fluorine diffusion slows down. In the stability tests of both sensors, it is noticeable that during the first stability cycle the phase decreases, probably due to the diffusion of fluorine into the core leading to decreases of its refractive index. As it was mentioned above, a potential reason is that the fluorine is diffused with a high rate, as a light element, from the cladding to the core, which leads to decrease of the refractive index and consequently to F-doped sensor's phase. Another possible reason of the anomalous behaviour of the F-doped sensor are crystallization effects that might occur at above 1000°C [140], affecting the effectiveness of the sensor. In conclusion, the presence of dopant in the sensing element of the FP sensor showed a huge impact to the sensor's functionality during its phase stability test. The F-doped depressed cladding FP sensors proved to be highly unstable at temperatures above 900°C, with a minimum temperature drift of 7°C at 850°C over 7 days.

#### 4.5 Pure SiO<sub>2</sub> (ESM-12B) Fabry-Pérot sensor

After finding out that the dopant in the sensing element of the Fabry-Pérot sensors has a huge impact at their phase stability, the next rational step was to build Fabry-Pérot sensors with an undoped sensing element consisted of pure SiO<sub>2</sub>. Ge-doped and F-doped Fabry-Pérot sensors showed a variety of phase drifts at high temperatures, with Ge-doped showing minimum drifts compared to the large phase drifts of the F-doped Fabry-Pérot sensors. A series of 4 undoped pure SiO<sub>2</sub> Fabry-Pérot sensors of different cavity lengths were manufactured and tested at high temperatures. The annealing cycles,

thermal cycles, and phase stability tests of the undoped pure SiO<sub>2</sub> FP sensors are presented in the next sections.

#### ***4.5.1 Annealing and Thermal Cycling of pure SiO<sub>2</sub> Fabry-Pérot sensors***

All graphs represent a single cooling down process from 1000°C to 25°C at a rate of 1°C min<sup>-1</sup>. Each sensor was subjected to two annealing cycles up to 1000°C where they stayed for approximately 30 minutes before returning to room temperature. **Figure 85** illustrates the annealing process and testing cycles of a 55µm pure SiO<sub>2</sub> sensor for three different dates during the stability test. **Figure 85(a)** portrays the annealing process phase response of the sensor before starting the stability test. **Figure 85(b)** portrays a testing cycle phase response of the sensor two months into the stability test. **Figure 85(c)** portrays a test cycle phase response of the sensor at the end of its stability test, having been exposed to temperatures above 850°C for three months. **Figure 85(d)** displays these three phase responses co-plotted all together. The phase response with respect to temperature is not linear for either sensor, instead it follows a 2<sup>nd</sup> order polynomial behaviour, as the phase is directly correlated with the thermo-optic coefficient.

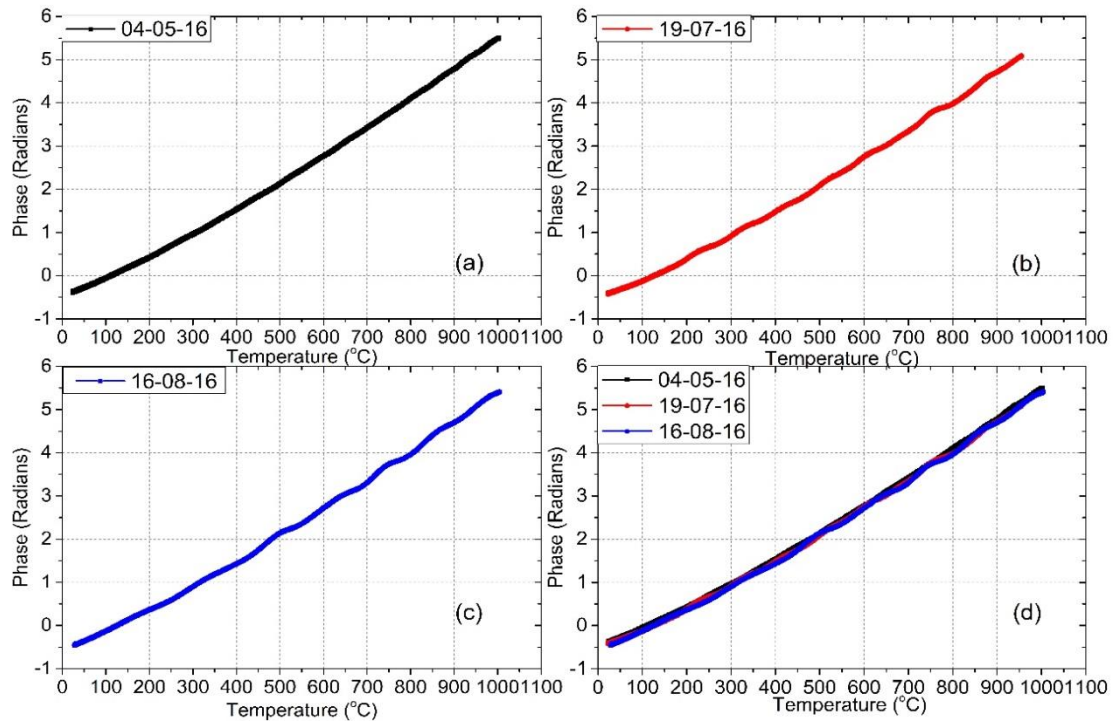


**Figure 85.** Phase response versus temperature of pure SiO<sub>2</sub> FP sensor (55μm) of three different time periods during stability test. Graph (a) corresponds to the annealing cycle, Graph (b) corresponds to the thermal cycle after two months have passed, Graph (c) corresponds to the thermal cycle after the end of the stability test and Graph (d) presents these three graphs together co-plotted.

As can be seen in **Figure 85(d)** the phase response of the sensor is stable over the three months of stability tests, confirmed by the fact that the three phase responses overlap each other. This can be a proof of no dopant diffusion in the sensing element of the sensor, as the sensor was made by pure SiO<sub>2</sub>. Nevertheless, within **Figure 85(b)** and **Figure 85(c)** modulations make an appearance, especially for temperatures above 200°C. These modulations come from a second order cavity that interferes with the signal of the fundamental cavity. This second order cavity is presumably correlated with expanding tapering phenomena of the core radius, caused by the germanium diffusion from the core to the cladding at elevated temperatures. These modulations make their appearance always during the annealing cycling up to 1000°C. At this point it should be mentioned that these sensors' sensing element is made from pure SiO<sub>2</sub> meaning that there is no waveguiding of the launched light in the cavity length. However, the cavity length of the sensors is short enough (less than 100μm) to keep the interference sinusoidal signal without losses due to beam divergence from the 2<sup>nd</sup> mirror of the FP cavity (fibre's cleaved end face).

In **Figure 85(d)** a comparison between the annealing cycle and thermal cycles versus temperature of a pure SiO<sub>2</sub> FP sensor with 63μm cavity length is demonstrated.



In the latter figure each cycle is co-plotted on the same graph, and each phase response of the sensor is overlapping each other, proving that there is no any distinctive phase difference between the annealing cycle and the thermal cycles. The phase response with regards to temperature proved to be robust. On the other hand, the phase modulations made their appearance again after two months at high temperature testing.

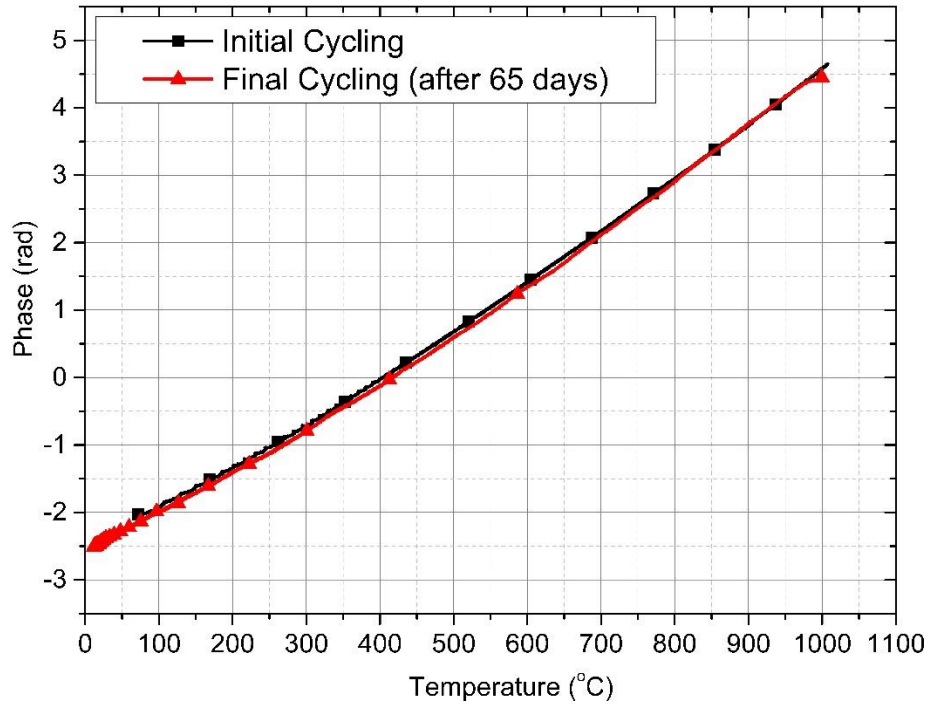


**Figure 86.** Annealing cycling and thermal cycle testing of a 65µm pure SiO<sub>2</sub> FP sensor. The sensor was at high temperature testing for 65 days.

The annealing cycle and thermal cycle of a pure SiO<sub>2</sub> FP sensor with 65µm cavity length is presented in **Figure 86**. The sensor was tested at temperatures between 900°C and 1050°C for a period of 65 days, with a step increment of 50°C. On the other hand, in **Figure 86** there is no any intense evidence of modulation at the phase response. Instead, after fitting with a 2<sup>nd</sup> order polynomial the phase response, there is an evidence of phase modulation throughout all the temperature range. **Figure 87** shows the residuals after the 2<sup>nd</sup> order polynomial fitting. The phase modulations at the residuals prove that a 2<sup>nd</sup> cavity interferes with the fundamental cavity signal.

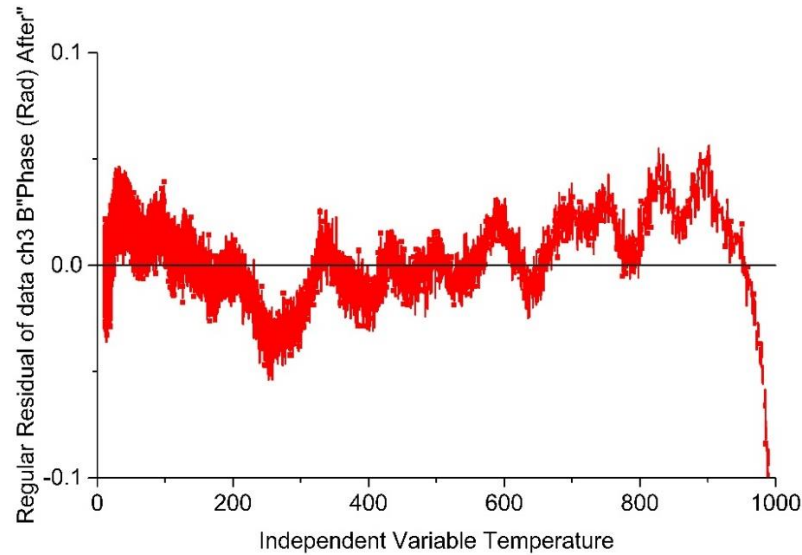


**Figure 87.** *Residuals of final cycling (red triangle data in Figure 86) after fitting a 2<sup>nd</sup> order polynomial to sensor.*

A conclusion that can be made from the annealing and thermal cycles of these sensors is that the undoped sensing element of a Fabry-Pérot sensor can eliminate the phase difference between the annealing and thermal cycles. On the contrary, the lack of dopant doesn't allow to the sensing element cavity to function as a waveguide. This can be a problem as the rest of the sensor is an SMF28 ultra fibre which operates as a waveguide of the interference signal created by the sensing element. High temperatures, especially above 1050°C, can affect the waveguiding fibre provoking tapered germanium diffusion along the fibre [75, 76]. The impact of this phenomenon is that the core diameter expands causing increase of the mode field diameter of the waveguiding fibre at the splice region. Hence, a second order mode cavity is introduced in the sensing element interfering with the fundamental cavity of the sensor.

#### **4.5.2 Long-Term Phase Stability Tests of pure SiO<sub>2</sub> Fabry-Pérot sensors**

The long-term stability phase response of pure SiO<sub>2</sub> sensors are presented in this section. The temperatures at which the sensors were subjected varied from 850°C up to 1050°C. It wasn't exceeded the temperature of 1050°C, as closing to the phase transition point of fused silica as it was done with the previous sensors. The sensors stayed at these high temperatures for a period ranging from 65 days to 100 days.

In **Figure 88** is demonstrated the long-term stability test of a 55µm pure SiO<sub>2</sub> sensor for 100 days. Its fringe visibility is 1 and its noise level is peak to peak <6°C, whilst after a 10-point averaging the noise is reduced to approximately one third of the

original noise  $<1.5^{\circ}\text{C}$ . A red dashed line was introduced as a baseline, showing the phase response at  $950^{\circ}\text{C}$ . With this sensor were completed three stability test cycles, investigating its phase response stability at different temperatures. As it is expected and can be seen in **Figure 88** is not detected any significant phase difference for the same temperatures between the cycles. This suggests that the lack of dopant diffusion in the pure  $\text{SiO}_2$  sensing element leads to higher stability while the sensing element of the Ge-doped FP sensor experiences an effective refractive index shift because of dopant diffusion. This then influences the effective cavity length of the fibre, giving an absolute change to the recovered phase. The upper temperature which can be seen in **Figure 88** indicates the temperature drift of 0.25 radians calculated from the sensitivity of the sensor at  $1000^{\circ}\text{C}$ .

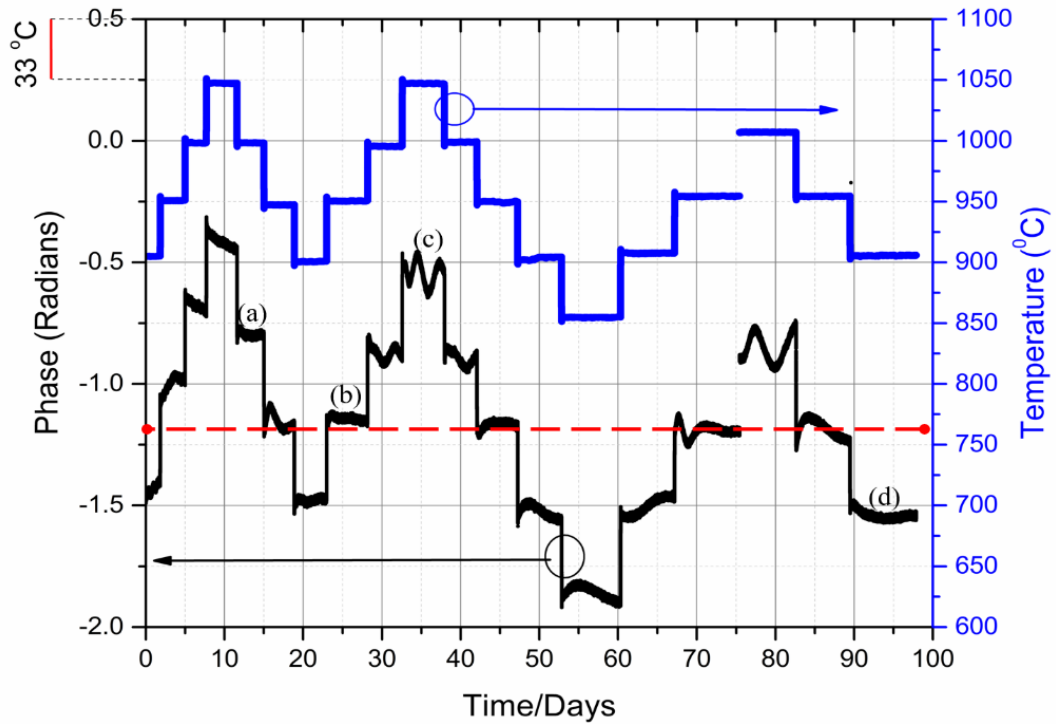


**Figure 88.** Long term stability test of pure  $\text{SiO}_2$  FP sensor ( $55\mu\text{m}$ ). Each letter is referred to the stability test of Figure 89. The red dashed horizontal line indicates the phase at  $950^{\circ}\text{C}$  of the third stability cycle.

Usually sensors don't exhibit large drifts after they have been subjected to a stability test throughout the cooling process. This is happening due to thermal relaxation of the optical fibre at temperatures above  $1000^{\circ}\text{C}$ . Expanded views of the stability test for some representative temperatures are presented at **Figure 89**. The sensor's drift at each temperature vary. For instance, during 1<sup>st</sup> and 3<sup>rd</sup> stability cycle's cooling process, the sensor exhibited a temperature drift of less than  $6^{\circ}\text{C}$ , after being exposed to  $1000^{\circ}\text{C}$  for 3.5 days **Figure 89(a)** and 8 days at  $900^{\circ}\text{C}$  **Figure 89(d)**. Also, at the heating process of 2<sup>nd</sup> stability cycle the sensor showed a temperature drift of only  $4^{\circ}\text{C}$  after a

period of 5 days at 950°C (**Figure 89(b)**). However, throughout a period of 5.5 days the phase behaviour follows a modulated behaviour instead of constant drifting upwards or downwards, especially above 1000°C. This can be seen in **Figure 89(c)** where the sensor's phase response is modulated with a 25°C temperature drift amplitude at 1050°C of the 2<sup>nd</sup> stability cycle. At this temperature, it is difficult to predict the phase behaviour of the sensors, as it sometimes has a periodic modulation and others it is constantly drifting. The modulated phase response is visible at various temperatures during the stability test as well. The 10-point averaged plot is the narrow red line that can be found in **Figure 89**.

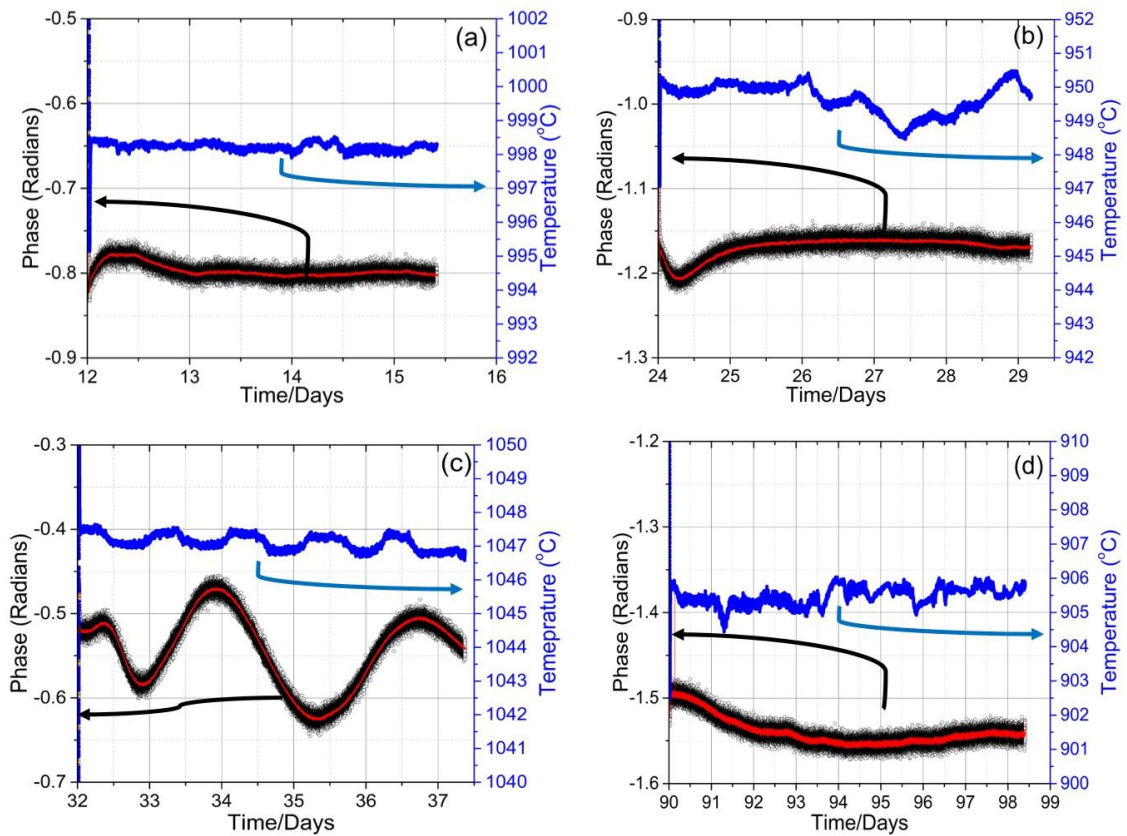


**Figure 89.** Expanded stability test views of the 55µm pure SiO<sub>2</sub> FP sensor at 1000°C (a), 950°C (b), 1050°C (c) and 900°C (d). The red lines represent a 10-floating point averaging.

As it was mentioned above, the 2<sup>nd</sup> cavity introduction for the pure SiO<sub>2</sub> is more likely to happen as there is no dopant diffusion in the sensing element. The pure SiO<sub>2</sub> sensing element doesn't operate as a waveguide due to its lack of core. Thus, the sinusoidal signal is not wave guided in the pure SiO<sub>2</sub> cavity. However, due to the short cavity of the sensing element the signal losses are negligible. At high temperatures, the waveguiding fibre experiences dopant diffusion as it was analysed in section 4.3. Then, in combination with the temperature profile of the furnace is created an adiabatic tapered core profile which leads to a possible introduction of a 2<sup>nd</sup> order mode cavity in

the sensing element. A more detailed tapering and diffusion analysis is investigated in **Chapter 5**.

**Figure 90** demonstrates the stability tests of a 65 $\mu\text{m}$  pure  $\text{SiO}_2$  FP sensor. The sensor completed two stability cycles between 900°C and 1050°C, over 65 days. Its fringe visibility is 0.65 and its peak to peak noise level is <12°C, whilst after a 10-point averaging is reduced to <4°C. In the same figure it is obvious, from the red dashed baseline, that there is not a significant phase difference at 950°C, between the stability cycles. This proves the impact of sensing element's dopant on the phase stability of the FP sensor. Throughout the long-term stability test of the 65 $\mu\text{m}$  pure  $\text{SiO}_2$  FP sensor, it was noticed an identical phase behavior presented in **Figure 90**. The sensor exhibited a stable phase behavior for temperatures below 1000°C. The phase response of the sensor seems to be the same, with small deviations, at 950°C between the 1<sup>st</sup> and 2<sup>nd</sup> stability cycle. Establishing again that the lack of dopant at this type of FP sensor affects its phase stability. The deviations come from possible temperature difference that was set manually on the furnace. The phase similarity between the cycles can be seen not only at 950°C, but at other temperatures as well.

A phase modulated behaviour is also present at temperatures such as 950°C, 1000°C and 1050°C of the 1<sup>st</sup> stability cycle. A 2<sup>nd</sup> order mode cavity is presumably makes its appearance, even though is not such distinctive as with the sensors presented in **Figure 88**. This happens due to the low fringe visibility of the last two sensors and their low signal to noise ratio.

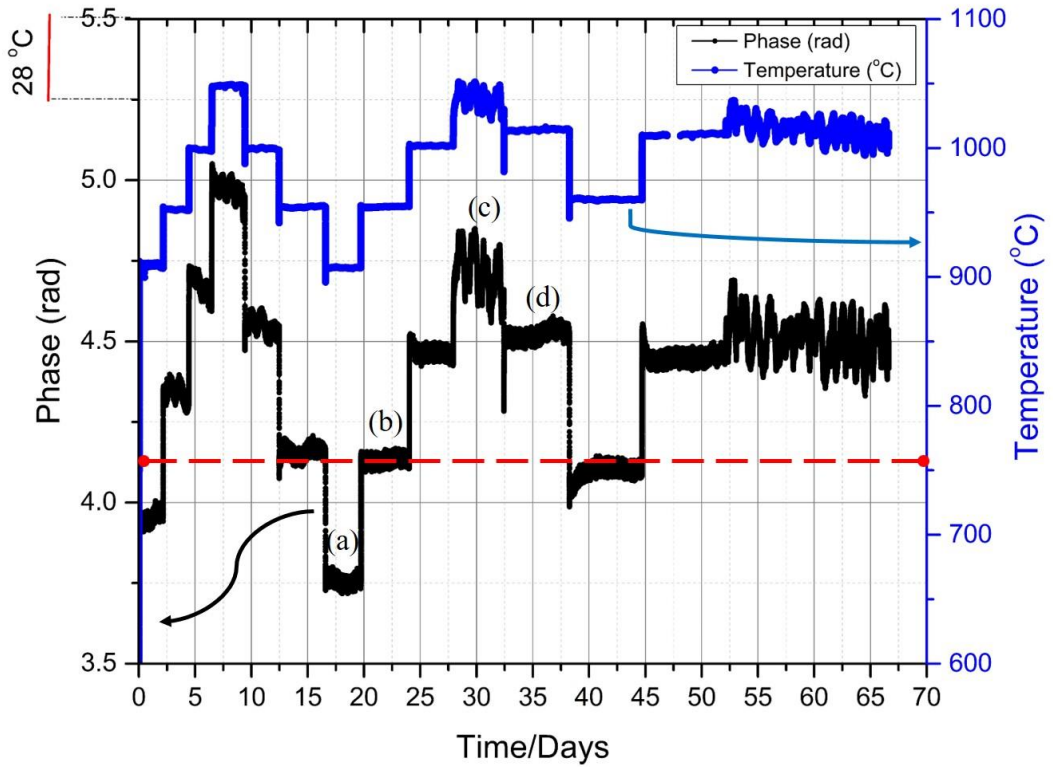


**Figure 90.** Long term stability test of pure  $\text{SiO}_2$  FP sensor ( $65\mu\text{m}$ ). Each letter is referred to the stability test Figure 91. The red dashed horizontal line indicates the phase at  $950^\circ\text{C}$  of the 3<sup>rd</sup> stability cycle.

In **Figure 91** the expanded views of the stability tests are presented. Each graph of the latter figure can be found at the correspondent letter in **Figure 90**. The sensor proved to be stable at  $900^\circ\text{C}$ ,  $950^\circ\text{C}$  and  $1000^\circ\text{C}$  presented in **Figure 91(a)**, **Figure 91(b)** and **Figure 91(d)**, respectively. Its temperature drift does not exceed  $10^\circ\text{C}$  for a period of up to 7 days. On the other hand, the temperature variation of the thermocouple due to furnace's instability (**Figure 91(c)**), matches the temperature drift of the sensor. The temperature drift of the sensor over 1 day is  $26^\circ\text{C}$ , whilst the temperature variation of the thermocouple for the same period is  $25^\circ\text{C}$ . The temperature response of the N-type thermocouple (blue data) can be seen in **Figure 91(a)**, where it exhibited a strange temperature variation recording of roughly  $2.5^\circ\text{C}$ , for up to 2 days. Nevertheless, this variation did not affect the phase response of the sensor. On the other hand, the temperature recording in **Figure 91(c)**, exhibits an interesting behaviour. The instability of the furnace to keep its temperature constant at  $1050^\circ\text{C}$  causes these variations at the temperature recording. The temperature variation measured by a thermocouple is  $25^\circ\text{C}$  and the sensor follows the same phase behaviour with a temperature drift of approximately  $27^\circ\text{C}$  over 1 day. The same effect can be seen at the end of the 2<sup>nd</sup> stability cycle.



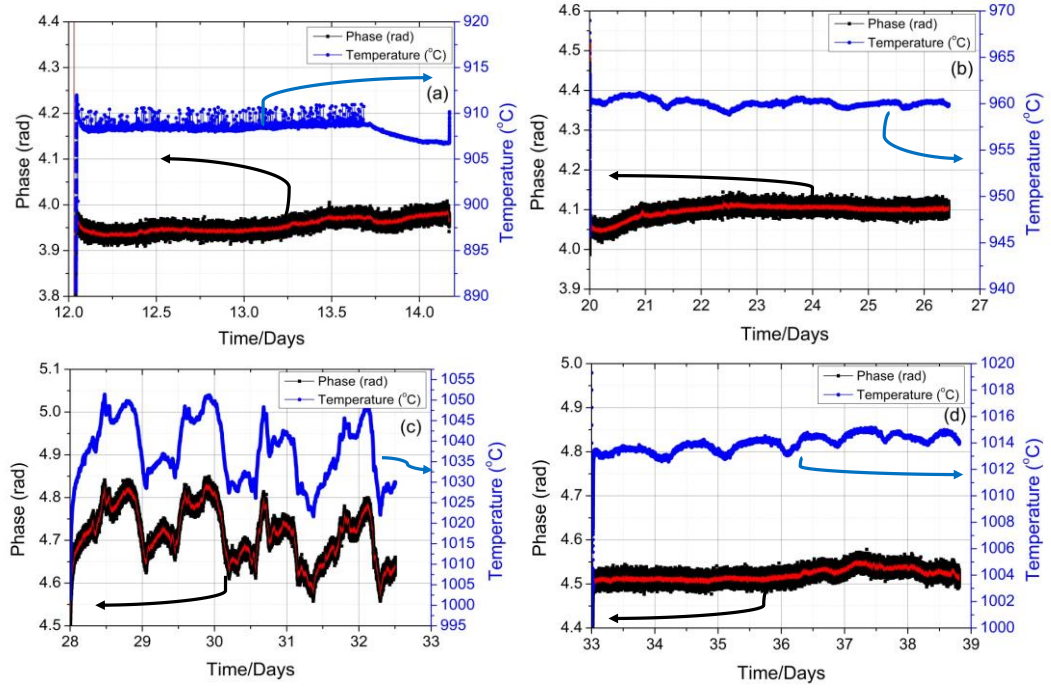


**Figure 91.** Expanded stability test views of the 65 $\mu\text{m}$  pure  $\text{SiO}_2$  FP sensor at 900°C (a), 950°C (b), 1050°C (c) and 1000°C (d). The red lines represent a 10-floating point averaging.

In conclusion, the lack of dopant in the sensing element of the Fabry-Pérot sensor improved sensor's functionality during its phase stability test. This improvement comes from the fact that there is no dopant in the sensing element to be diffused neither towards the outer cladding, as Ge-doped core FP sensors, either to the inner core, as F-doped depressed cladding FP sensors. However, the undoped pure  $\text{SiO}_2$  FP sensors exhibited a modulated phase behaviour over time instead of a constant drifting. This can be an evidence of a 2<sup>nd</sup> order mode cavity introduction interfering with the fundamental cavity. Thus, the undoped pure  $\text{SiO}_2$  Fabry-Pérot sensor presents a good stability response while operating below 1000°C.

#### 4.6 Conclusions of Chapter 4

The phase response during long-term stability tests of intrinsic optical Fabry-Pérot optical fibre sensors was investigated in this chapter. The annealing cycle, thermal cycles, and long-term stability tests for different types of Fabry-Pérot sensors were presented.

The phase response with regards to temperature of a Fabry-Pérot sensor, proved to have a nonlinear behaviour. This is attributed to the 2<sup>nd</sup> order dependency of fused silica on temperature. The sensitivity of FP sensors with various cavity lengths between 40 $\mu\text{m}$  and 100 $\mu\text{m}$ , has been calculated and presented for different temperature ranges. At

higher temperatures, the sensor exhibited higher sensitivities. The theoretical phase response results showed a good match with the experimental as well. An analysis of Fabry-Pérot sensors' sensitivity proved that sensors with longer cavity exhibit higher sensitivity. However, as the resolution of the interrogation system is constant, the signal to noise ratio decreases with cavity length. Thus, based on theoretical calculations it was estimated an optimum cavity length for the Fabry-Pérot sensor. A cavity length between the range of 30µm and 100µm proved to be satisfactory for our data analysis routine.

Three different types of Fabry-Pérot sensors with different sensing elements were tested at high temperatures for a period up to 100 days. There were manufactured FP sensors with Ge-doped core, F-doped depressed cladding and pure SiO<sub>2</sub> sensing elements. A phase difference between the annealing and thermal cycles was present for all the Ge-doped core and F-doped depressed cladding FP sensors. On the contrary, the phase difference was eliminated or negligible at the comparison of annealing and thermal cycles, for the pure SiO<sub>2</sub> FP sensors. The phase difference emanates from the permanent change of the sensing element's core refractive index due to dopant diffusion, when it is subjected to high temperatures. A detailed summary of each Fabry-Pérot sensor's performance at numerous temperatures is presented at **Table 6**.

**Table 6. Summary of temperature drift for each type of Fabry-Pérot sensor for various stability periods and temperatures.**

Type of sensor Temperature	Ge-doped core SMF28 ultra (60µm cavity)	Pure fused silica – PCF (55µm cavity)	F-doped depressed cladding F-SM1500SC-P (69 µm cavity)
1050°C (over 5 days)	18.1°C	11.4°C	>100°C
1000°C (over 5 days)	9°C	<1°C	>100°C
950°C (over 5 days)	2.5°C	<2°C	>100°C
900°C (over 8 days)	4°C	<1°C	<10°C
850°C (over 7 days)	3°C	<2°C	<7°C

In addition, modulated phase behaviour has been observed at the phase response at all the sensors. The phase modulations made their appearance after different periods of time for each type of sensor. These phase modulations emanate from a 2<sup>nd</sup> order mode cavity introduction into the fundamental one, while the core diameter is increased in a tapered formation by dopant diffusion. The Ge-doped sensors exhibited these modulations to the minimum as germanium diffuses with a slow rate compared to fluorine of the F-doped sensors. On the other hand, pure SiO<sub>2</sub> sensors showed a more intense modulated behaviour due to the lack of core in their sensing element. The



diffusion that takes place at the waveguiding fibre of the FP sensor creates a tapered core diameter enlargement leading to the introduction of the 2<sup>nd</sup> order mode cavity into the fundamental cavity.

Ge-doped core FP sensors proved to be stable at temperatures up to 1050°C. However, the sensors present better stability when a stability test cycle was preceded reaching up to 1100°C. Above this temperature, the sensors proved to be highly unstable, with large discrepancies and drifts in response. Furthermore, the results show that the Ge-doped FP sensor can be used for reliable temperature measurements for 5 days up to 1050°C with accuracy better than 5°C. F-doped depressed cladding FP sensors proved to be highly unstable at temperatures above 900°C, achieving a minimum temperature drift of 7°C at 850°C over 7 days. The presence of fluorine dopant in their sensing element proved to have a huge impact to the sensor's stability even in the beginning of the stability test. Fluorine is a light element and its diffusion rate is much faster than germanium's leading high temperatures to have a greater impact on it. In addition, the lack of dopant in pure SiO<sub>2</sub> sensors' sensing element improved their phase response stability over time. However, the absence of dopant enhances the possibility of a 2<sup>nd</sup> order mode cavity to interfere in the fundamental cavity. The undoped FP sensors exhibited modulated phase behaviour instead of constant upwards or downwards drifting compared to previous sensors presented. Nevertheless, undoped pure SiO<sub>2</sub> sensors showed a temperature drift less than 6°C for temperatures up to 1000°C. Also, by comparing the phase response, at a specific temperature, between the stability cycles it was found out that there was a phase difference for the doped FP sensors, whilst for the undoped FP sensors the phase difference between the cycles was negligible. Again, this is evidence that dopant diffusion phenomena affect the phase stability and robustness of optical Fabry-Pérot optical fibre sensors.

## Chapter 5: Dopant Diffusion of Optical Fibres at High Temperatures

In this chapter, the diffusion and tapering phenomena that occur in an optical fibre and can affect its phase stability and robustness at high temperatures are described. The optical fibre sensors tested at temperatures up to 1150°C over 100 days, were investigated for diffusion of the germanium dopant, through Scanning Electron Microscopy (SEM) coupled with Energy Dispersive X-ray (EDX) Spectroscopy. Based on theoretical modelling calculations, an analysis of a 2<sup>nd</sup> order mode interference in the fundamental cavity has been conducted.

A measured temperature profile of the furnace that was used is also demonstrated. The temperature profile of the furnace is correlated with tapering phenomena and experimental diffusion results in optical fibres. Also, an evaluation of the circumstances that could form a 2<sup>nd</sup> order mode cavity in the optical fibre, are analysed. In addition, an investigation of expanded core diameter longitudinally to the optical fibre is presented.

### 5.1 Longitudinal Temperature Furnace's Profile

The furnace Nabertherm RD 30/200/11 is a 36cm full length tube furnace with the maximum temperature at its center. In **Figure 92**, an illustration of the half-length temperature profile of the furnace, used for stability experiments, is depicted. A type N thermocouple was introduced in the furnace such a way its tip sits in its center. The furnace temperature was set to 1020°C and the thermocouple was given 2 minutes to thermally match the furnace. Once the thermocouple reached equilibrium, at 1020°C, the thermocouple has been removed of the furnace with a 1cm step.

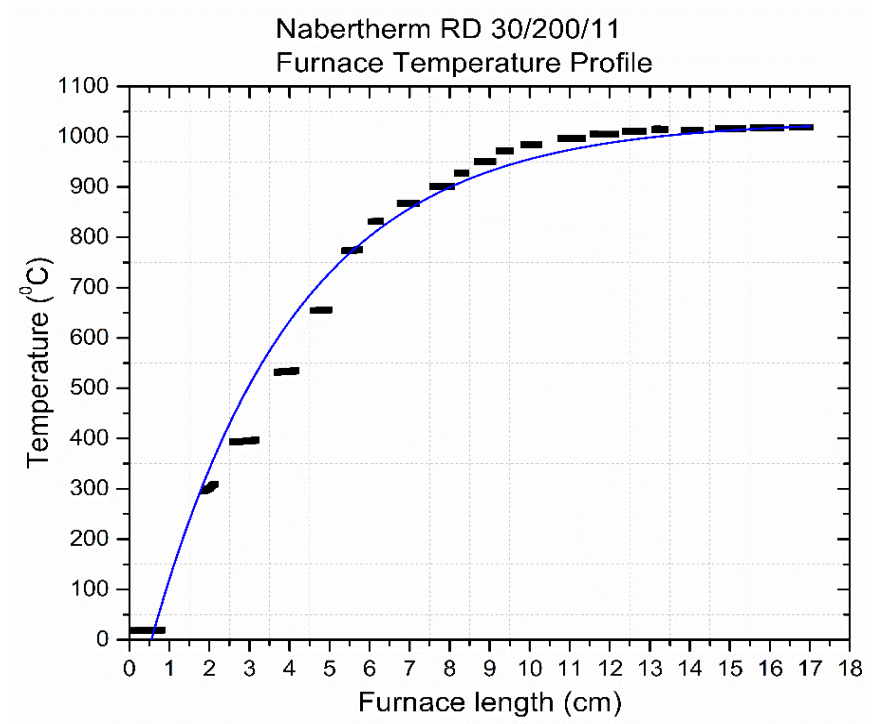


**Figure 92.** Temperature longitudinal profile of the tube furnace (Nabertherm RD 30/200/11) measured by an N-type thermocouple. Black data represent the experimental data, blue line is the theoretical exponential fitting.

The temperature profile of the Nabertherm furnace gives an estimation of the temperature range that heats the optical fibre at a specific position. As it was abovementioned, the Fabry-Pérot sensing element is positioned at the tip of the optical fibre. The remaining optical fibre length functions as a waveguide for the interference signal which is generated in the Fabry-Pérot cavity. This optical fibre length experiences temperatures below the maximum temperature we set on the furnace. Hence, these high temperatures affect the optical fibre sitting in the furnace. The temperature experimental data (black data), presented in **Figure 92**, exhibit an exponential behaviour starting from the edge of the ceramic tube up to its centre. This specific temperature profile of the furnace can justify potential tapering phenomena along the optical fibre spliced to our sensor [141-143]. The maximum dopant diffusion takes place at the centre of the ceramic tube, while moving out of the furnace the diffusion gradually starts decreasing.

## 5.2 Propagating mode analysis

During the annealing and thermal cycling of Fabry-Pérot sensor, a modulated phase behaviour in a temperature range between 200°C and 1000°C has been observed. This modulated behaviour is attributed to a 2<sup>nd</sup> order mode cavity that interferes with the fundamental cavity of the Fabry-Pérot sensor. According to the optical fibre theoretical background, quoted in **Chapter 2**, an optical fibre is considered single mode

for a normalized frequency  $V < 2.405$ . Above this threshold, the optical fibre can support more than one mode. The refractive indices that have been used throughout theoretical modelling are calculated from the Sellmeier coefficients ( $A_1, A_2, A_3, B_1, B_2, B_3$ ), found in literature [144, 145]. Both refractive indices of the core (black data) and the cladding (red data) of an SMF28 ultra optical fibre, are displayed at **Figure 93**.

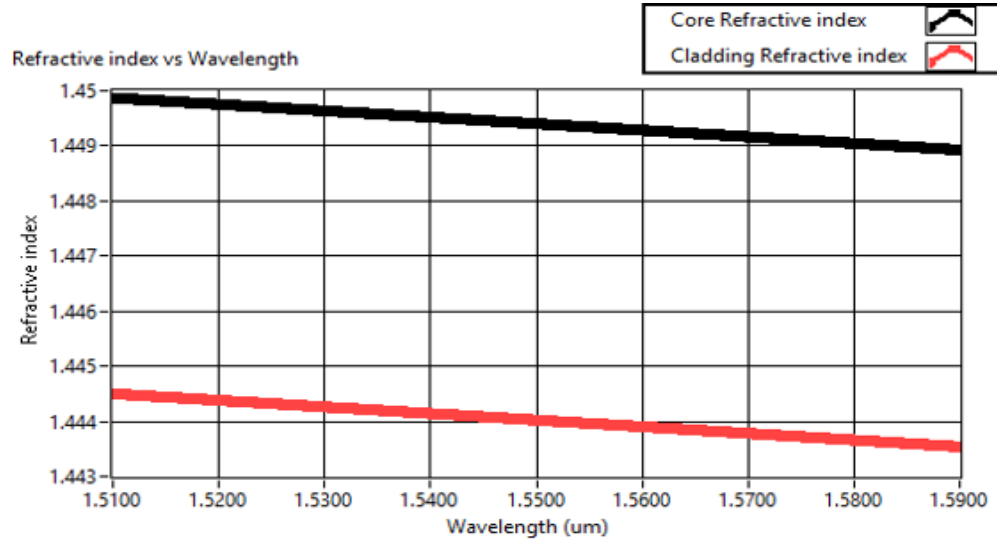


**Figure 93.** Core and cladding refractive indices of SMF28 optical fibre with respect to wavelength of our spectrum. Both values are calculated based on Sellmeier equation with coefficients found in the literature [144, 145].

Based on theoretical calculations, in **Figure 94** the normalized frequency  $V$  with regards to wavelength, for two different core radii is demonstrated. In the latter figure, black data corresponds to the initial radius of the core before the optical fibre is heated,  $\alpha = 4.1 \mu\text{m}$ , while the blue data correspond to the final radius of the core after being heated, which is  $\alpha = 5 \mu\text{m}$ . The final radius comes from the experimental results presented in **5.5.3**. The red dashed line in the same figure represents the threshold for which a fibre terminates to function as single mode. Considering that for a radius of  $\alpha = 5 \mu\text{m}$ , each wavelength of the spectrum can support a second order mode ( $LP_{11}$ ) in the fibre, it can be concluded that the appearance of a second cavity in a sensor with this core radius is feasible. Assuming that the taper is axisymmetric, as is usually the case with a single fibre taper, then the fundamental  $LP_{01}$  local mode can partially couple to  $LP_{11}$  mode which its different propagation constant causes the phase modulations at high temperatures [75, 76, 146].

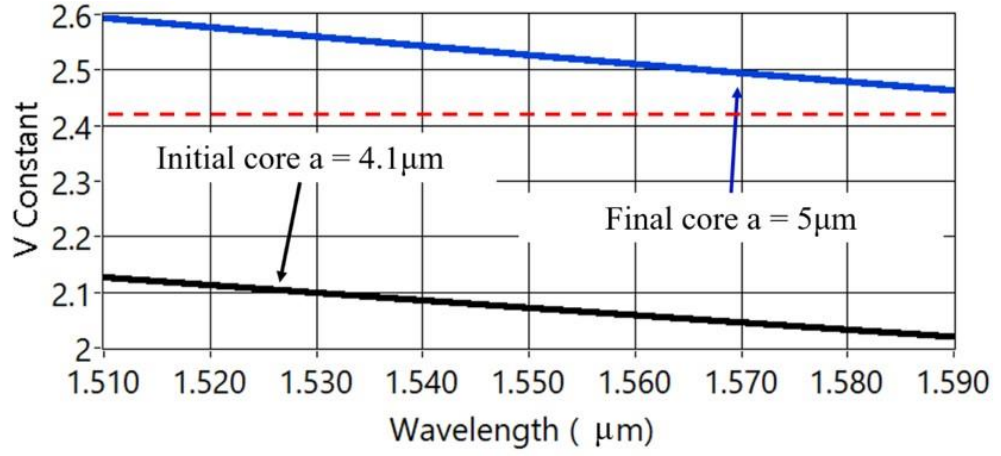


**Figure 94.** Theoretical calculation of V-number with respect to wavelength for the initial and final core fibre radii, before (black data  $a=4.1\mu\text{m}$ ) and after (blue data  $a=5\mu\text{m}$ ) diffusion. The red dashed line shows where the V-number is 2.405.

Using fibre optics toolbox of Matlab software package, a model was built to investigate the validation of the 2<sup>nd</sup> order mode in a  $4.2\mu\text{m}$  and a  $5\mu\text{m}$  core radius optical fibre. The input refractive indices of the optical fibre are  $n_{\text{core}} = 1.44934$  and  $n_{\text{clad}} = 1.44395$ . A slight germanium diffusion from core to cladding will transform the step index profile to a graded index profile, broadening the MFD of the fibre. For simplification purposes, the model calculates the propagating degenerated modes of a given optical fibre's radius for a stepped refractive index profile. The optical fibre is considered weakly guided due to the very small difference between the refractive index of the core and the cladding. In a weakly guided fibre mode  $\text{HE}_{11}$  is denoted as  $\text{LP}_{01}$  mode and the  $\text{HE}_{21}$ ,  $\text{TM}_{01}$ ,  $\text{TE}_{01}$  mode triplet as  $\text{LP}_{11}$  mode.

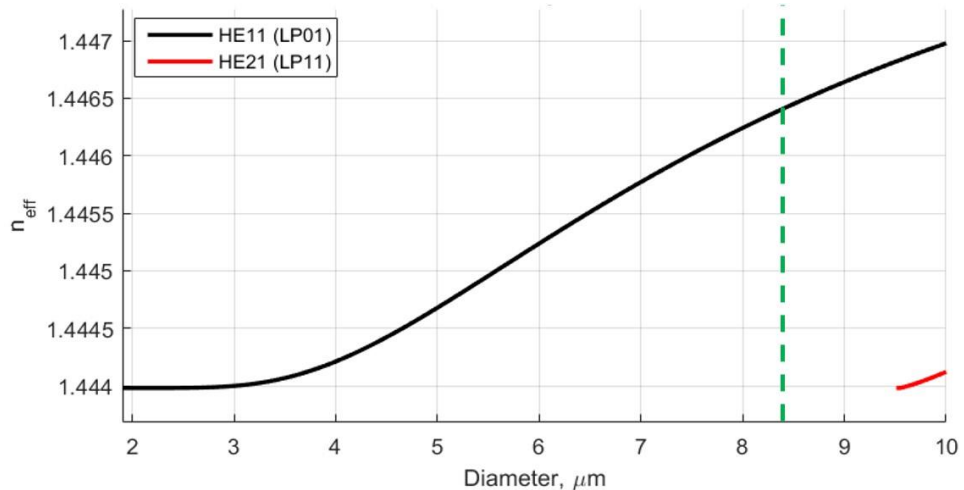


**Figure 95.** Effective refractive index with respect to core diameter for an optical fibre with  $10\mu\text{m}$  diameter. Both degenerate modes  $\text{HE}_{11}$  and  $\text{HE}_{21}$ , with their correspondent linear polarized modes  $\text{LP}_{01}$  and  $\text{LP}_{11}$ , respectively, are shown in caption. The green dashed vertical line points out the  $8.4\mu\text{m}$  diameter of a single mode optical fibre, before the beginning of diffusion.

In **Figure 95**, the effective refractive index versus core diameter is demonstrated. A core diameter of 8.4µm (green dashed vertical line) which corresponds to an unheated optical fibre supports only the fundamental LP<sub>01</sub> mode. For a 10µm diameter, which corresponds to the enlarged core diameter due to diffusion, a 2<sup>nd</sup> order mode can be supported. The red data correspond to the LP<sub>11</sub> mode that can propagate simultaneously with the fundamental mode in the F-P cavity. Modal dispersion of both propagating modes is depicted in **Figure 96**. As a result, the propagating mode analysis of an optical fibre with a characteristic core diameter of 10µm, after diffusion phenomena take place, can support a 2<sup>nd</sup> order mode in its sensing element cavity, which is the linear polarized LP<sub>11</sub> mode.

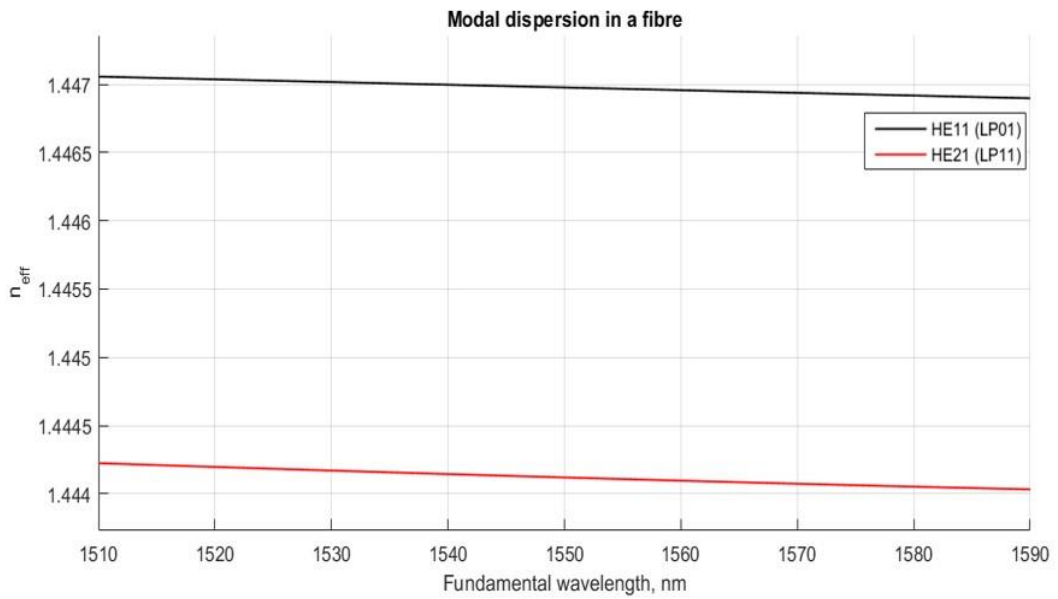


**Figure 96.** Effective refractive index versus wavelength of the fundamental LP<sub>01</sub> mode and the 2<sup>nd</sup> order LP<sub>11</sub> mode calculated for a 10µm core diameter optical fibre.

It is worth mentioning that the SMF28 fibre has a step index refractive index profile, but after a heating at high temperature the diffusion results showed that the fibre exhibited something closer to a graded index profile. Furthermore, the diffusion of the germanium dopant towards the cladding modifies the step index profile of the core to graded index profile. A graded index profile fibre contains a core in which the refractive index diminishes gradually from the centre axis out towards the cladding [147, 148].

$$V_{gr} = 2.405 * \left(1 + \left(\frac{2}{\alpha}\right)^{1/2}\right) \quad \text{Equation 20}$$

$$M = \frac{V_{gr}^2}{4} \quad \text{Equation 21}$$

The normalized frequency ( $V_{gr}$ ) and the number of modes ( $M$ ) for a graded index fibre with a parabolic index profile ( $\alpha=2$ ) are calculated from **Equation 20** and **Equation 21**, respectively [49, 147]. A 2<sup>nd</sup> order mode introduction in the sensing element is feasible according to Matlab calculations. The theoretical model results showed that a parabolic index profile with the 5 $\mu$ m core radius (black data) where the dopant diffusion took place at the edges of the core-cladding interface can support a 2<sup>nd</sup> order mode ( $M=2.85$ ). Similarly, when the dopant diffusion takes place on the full area of the core (blue data), a 2<sup>nd</sup> order mode cavity can be supported ( $M=2.71$ ). In the latter occasion, the diffusion leaves the centre of the core with the 85% of its initial refractive index and increases the core radius to 5.5 $\mu$ m. **Figure 97** portrays the refractive index profile of each occasion.

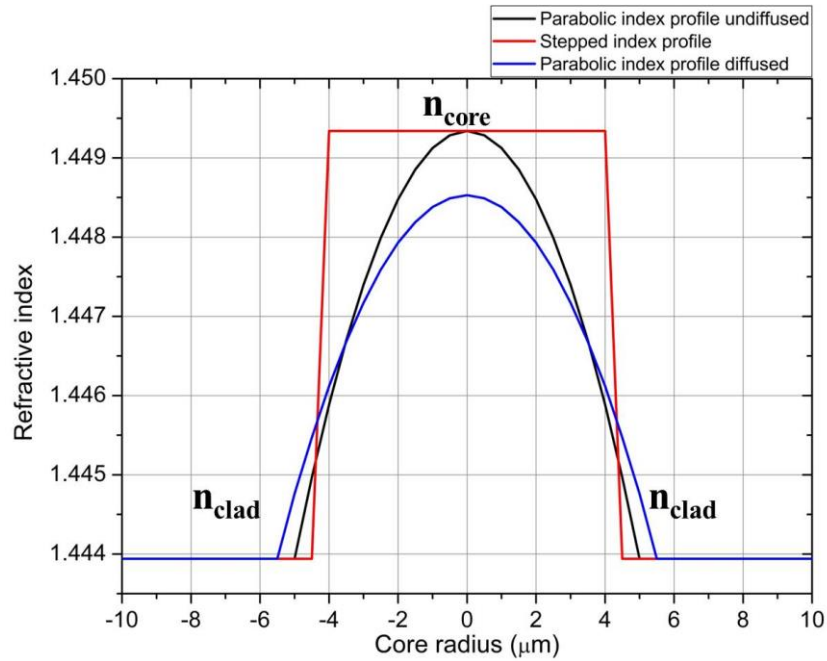


**Figure 97.** Refractive index profile of an optical fibre before and after dopant diffusion. Red data correspond to an unheated stepped index profile. Black data to a heated fibre with diffused edges graded index profile, and the blue data correspond to a heated fibre where dopant diffusion transforms the stepped index profile to a graded index parabolic profile.

### 5.3 Schematic tapering representation of Fabry-Pérot sensor

In 5.1 the temperature profile of the Nabertherm furnace that have been used in our experiments, was recorded. The temperature profile is characterized by an exponential behaviour starting from the edge of the ceramic tube up to its centre. According to that, the region of the sensor placed in the centre of the furnace experiences higher temperatures than the region positioned at the edge of the furnace. The length of the fibre which sits in the furnace is 17cm, thus the rest of the fibre in

which the fundamental signal is travelling, is heated. Hence, the dopant diffusion takes place along the whole fibre which sits in the furnace, causing an adiabatic tapering to the core of the fibre and leading subsequently to a monotonic increase of the core radius [142]. All the Fabry-Pérot optical fibre sensors that have been used throughout the phase stability experiments at high temperatures were manufactured with a SMF28 ultra waveguiding optical fibre. As it has been described in **Chapter 3**, the various types of sensors that were manufactured had a different type of optical fibre as a sensing element.

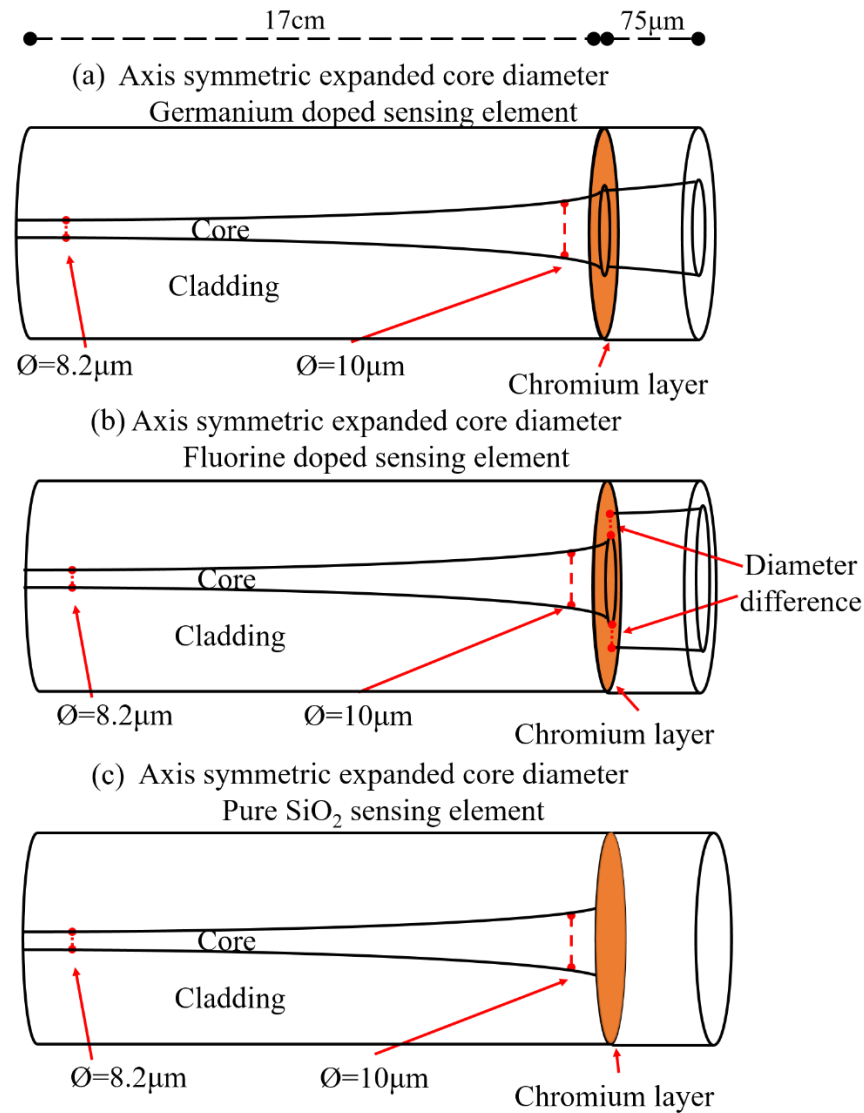


**Figure 98.** Schematic representation of a tapered expanded core diameter due to germanium dopant diffusion from core to cladding. (a) The sensing element follows the same performance. (b) The sensing element has a fluorine doped cladding, thus fluorine dopant diffusion from cladding to core takes place. (c) The sensing element is coreless pure SiO<sub>2</sub>, thus diffusion phenomena will not take place in it.

**Figure 98** portrays a schematic representation of germanium's diffusion along the SMF28 ultra waveguiding fibre. In addition, is depicted the core increase due to dopant



diffusion, in the sensing element of each type of Fabry-Pérot sensor. The expansion of the core diameter results to the increase of mode field diameter (MFD). For temperatures above 500°C, the thermal expansion coefficient (CTE) is responsible for the development of thermal stress for F-P sensors with different doped sensing elements, affecting the phase of each sensing element [63]. Both germanium doped and fluorine doped fibres experience a MFD broadening due to dopant diffusion, regardless of dopant direction, inwards or outwards respectively [149]. A typical core radius of a SMF28 ultra is 4.1µm and its correspondent MFD is 5.2µm. According to the theoretical calculations on Matlab software an expanded diffused core with a radius of 5µm shows a MFD of 6.34µm.

**Figure 98(a)** portrays the expanded tapered diameter of germanium doped core. The sensing element shares the same characteristics with the waveguiding fibre, so it is expected a uniform tapering between them. For this type of F-P sensor, the phase modulations made their appearance at a later stage during the thermal cycling, and after the sensors have been subjected to temperatures up to 1100°C for more than 90 days. The germanium has a low diffusion rate and the enlargement of core's diameter needs a period to reach a value that can support a 2<sup>nd</sup> order mode in its cavity.

On the other hand, in an F-doped F-P sensor the sensing element ends up to a larger core diameter than Ge-doped sensing element. In **Figure 98(b)**, a schematic representation of diffusion tapering for an F-doped F-P sensor is portrayed. The diffusion of fluorine from the cladding to the core occurs with a faster rate, as it is lighter than germanium [6]. The fast diffusion of fluorine gives the opportunity at the sensing element to support a 2<sup>nd</sup> order mode even during the annealing cycling. The F-doped F-P sensors were subjected to temperatures up to 1050°C over 55 days and according to the experimental results of **Chapter 4** the sensor proved to support a 2<sup>nd</sup> order mode cavity during both annealing and thermal cycling. Fluorine's core diameter broadening is larger than germanium doped sensing element, creating a diameter difference between the waveguiding fibre and the sensing element.

The main difference between the above-mentioned F-P sensors and the undoped pure SiO<sub>2</sub> F-P sensor is that there is no core in its sensing element, consequently the interference signal is not wave guided. Due to the short length of the sensing element (<100µm) there are no significant losses due to beam divergence. **Figure 98(c)** portrays a schematic representation of the coreless undoped pure SiO<sub>2</sub> F-P sensor, in which a 2<sup>nd</sup>

order mode cavity can be introduced from the core diameter broadening of the Ge-doped waveguiding fibre. Diffusion phenomena do not take place in this sensor's sensing element, thus the 2<sup>nd</sup> order mode cavity depends only by the broadening of waveguiding fibre's core. In this context, an enlarged core diameter of 10µm, with respect to **Figure 94**, can support a second order mode travelling in the core alongside the first order mode. There is a small percentage of energy exchange between the first and second mode, activating the second order mode and creating the propagation of another cavity's signal.

#### 5.4 Theoretical phase modulated behaviour

The partial power transfer from the fundamental mode cavity to the 2<sup>nd</sup> order mode cavity generates a superposition of both signals to the output interference signal, which is in the sensing element. Each mode's sinusoidal signal, including their superposition is described mathematically in **Equation 22**, **Equation 23** and **Equation 24**, respectively. The superposition output signal has a characteristic phase, frequency, and amplitude. The latter values are extracted through LabVIEW's single tone extraction VI and are fitted on the reflected sensor's spectrum. The single tone extraction VI takes a signal in, finds the single tone with the highest amplitude, or searches a specified frequency range, and returns the single tone frequency, amplitude, and phase. The phase modulations presuppose another sinusoidal signal in the fundamental cavity causing an oscillation at the single tone detection, and consequently at the phase detection. In **Equation 24** the parameters  $\alpha$  and  $b$ , are the coupled energy percentage of the total input power.

$$I^{1st\ mode} = I_1 + I_2 + 2 * \sqrt{I_1 * I_2} * \cos\left(\frac{4 * \pi * n_{eff}^{1st\ mode} * L}{\lambda}\right) \quad \text{Equation 22}$$

$$I^{2nd\ mode} = I_1 + I_2 + 2 * \sqrt{I_1 * I_2} * \cos\left(\frac{4 * \pi * n_{eff}^{2nd\ mode} * L}{\lambda}\right) \quad \text{Equation 23}$$

$$I^{total} = a * I^{1st\ mode} + b * I^{2nd\ mode} \quad \text{Equation 24}$$

$$\frac{dn}{dT} = 8.2 * 10^{-6} + 1.04 * 10^{-8} * T - 5.6 * 10^{-12} * T^2 \quad \text{Equation 25}$$

The 2<sup>nd</sup> order mode will propagate in the sensing element with a different propagation constant. The thermo-optic coefficient of germanium is  $6 * 10^{-4} \text{ } ^\circ\text{C}^{-1}$  at 25°C

[150], two orders of magnitude larger than fused silica. Considering that the core of the optical fibre is doped with germanium in a small percentage, the thermo-optic coefficient of fused silica, with a 2<sup>nd</sup> order dependency on temperature (*Equation 25*), will slightly differ from Ge-doped core material [60, 151, 152].

The phase response with respect to temperature has been modelled on LabVIEW software investigating how a 2<sup>nd</sup> order mode cavity can generate these phase modulations. Considering that partial coupling of 5%, 10% and 15% intensity from the fundamental to the second order mode was achieved. **Figure 99** presents the correspondent spectra for each occasion. In addition, increasing the coupling power transfer of the 2<sup>nd</sup> order mode in the cavity results to more intense phase modulations. This can be seen in **Figure 100** where the phase response of a 40µm F-P sensor has been modelled for three different power transfer percentages from fundamental mode to the 2<sup>nd</sup> order mode.

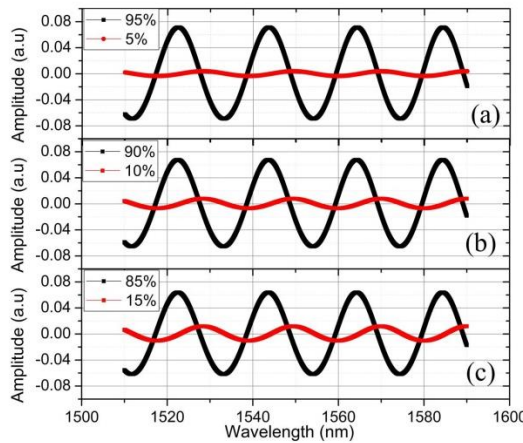


**Figure 99.** Theoretical co-plotted spectra of 1<sup>st</sup> and 2<sup>nd</sup> order mode cavity, of different energy coupling. In captions is quoted the energy percentage of the 1<sup>st</sup> and 2<sup>nd</sup> mode, respectively.

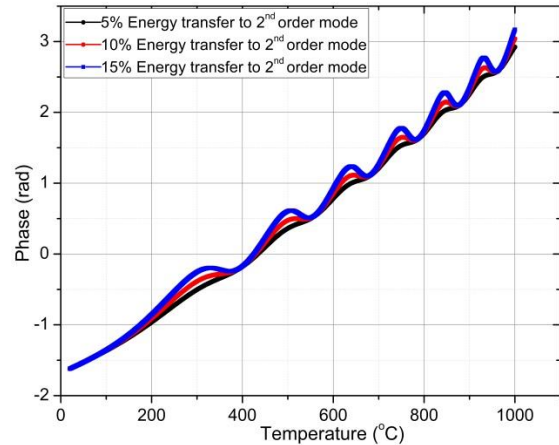


**Figure 100.** Theoretical calculations of phase modulations with respect to temperature. The phase response corresponds to a 40µm F-P sensor, while each data colour corresponds to a different coupled power transfer from the 1<sup>st</sup> order mode to the 2<sup>nd</sup> order mode cavity.

In **Figure 101**, a comparison of the experimental and theoretical phase modulated behaviour is presented. This figure presents the phase response of a Ge-doped F-P sensor, with 40µm cavity length, after has been stability tested between 900°C and 1100°C for 90 days. The sensor exhibited an intense modulated phase behaviour during its thermal cycling. The black data correspond to the experimental phase response while the red data to the theoretical calculated phase. In **Figure 101**, the introduction of a 2<sup>nd</sup> cavity signal interfering with the fundamental cavity resulted to the modulated phase response is depicted. The theoretical phase modulation is created by 95% power

coupling to the 1<sup>st</sup> order mode and 5% to the 2<sup>nd</sup> order mode. There is a good matching between the theoretical model and the experimental data, proving that the modulations during the thermal cycling emanate from a 2<sup>nd</sup> order mode cavity interfering with the fundamental cavity.

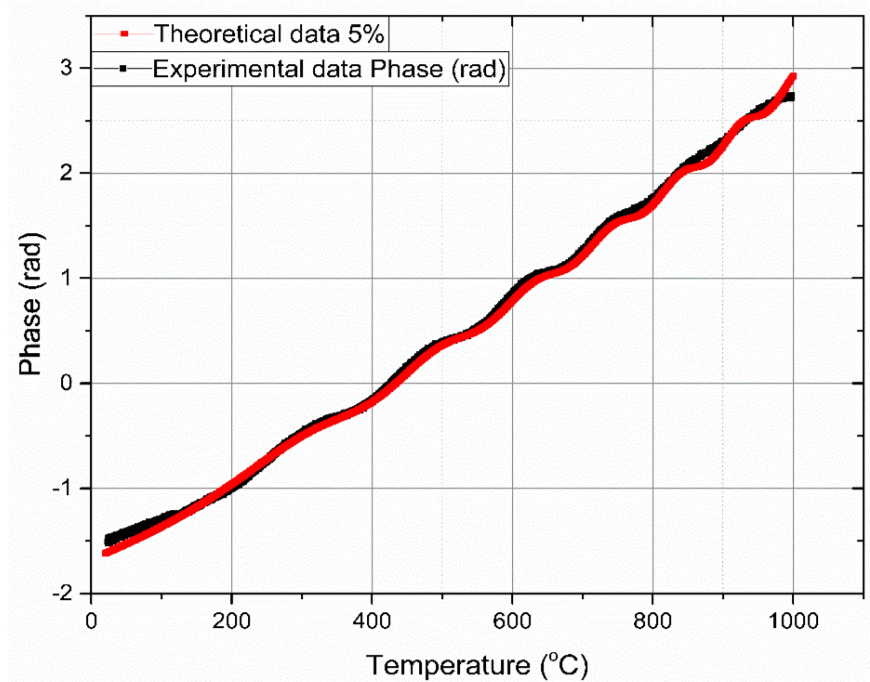


**Figure 101.** *Modulations at the phase response of a 40  $\mu\text{m}$  F-P sensor with regards to temperature. The black data correspond to experimental phase data and the red data to the theoretical data for a 5% energy transfer to the 2<sup>nd</sup> order mode cavity. In captions are given the fitting functions of both plots.*

**Figure 102** presents the residuals after a 2<sup>nd</sup> order polynomial fitted to the experimental (red square data) phase response and the theoretical (black triangle data) phase response. For temperatures above 800°C a mismatch is clearly visible, due to the dependency of phase on the thermal expansion coefficient (CTE) at high temperatures.

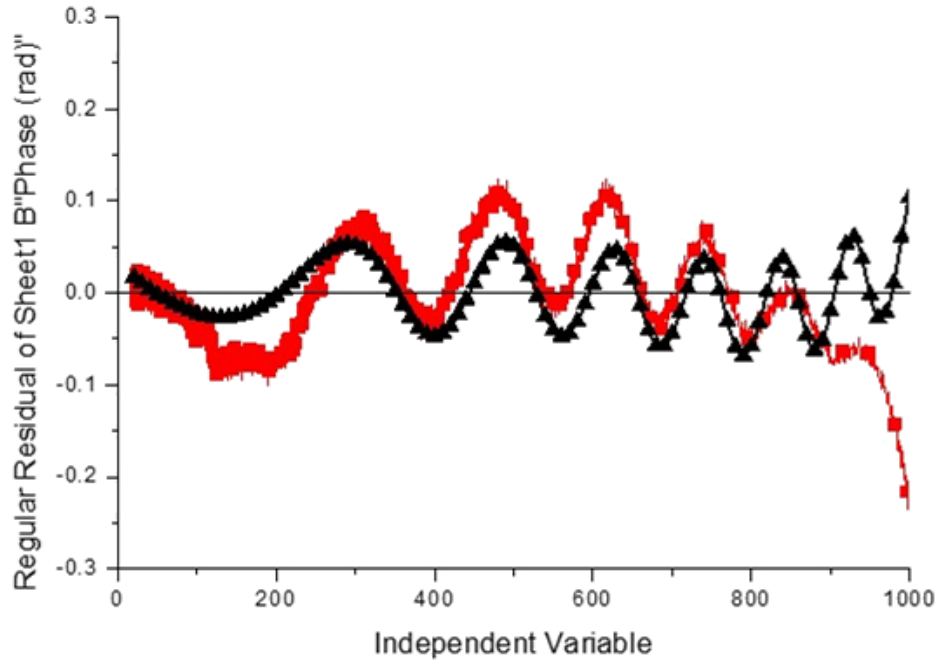


**Figure 102.** *Residuals of experimental (red square data) and theoretical (black triangle data) modulated phase fitted with a second order polynomial function.*

## 5.5 Dopant Diffusion Experimental Results

From the theoretical analysis, dopant diffusion has the capability to cause changes on the phase stability response of the F-P sensor. To demonstrate that this effect is indeed occurring within these sensors, it was necessary to measure the diffusion in the heated fibre. In this section are presented the experimental diffusion results which were obtained through an Energy Dispersive X-ray (EDX) Spectroscopy technique, measuring the percentage of the dopant's diffusion. The same technique was applied to both sensors, Ge-doped and F-doped, however as fluorine is a low-z material it proved to be insufficient to be measured by EDX, according to literature [77, 153, 154].

### 5.5.1 Fibre preparation for Energy Dispersive X-rays (EDX) analysis

One of the F-P fibre sensors was removed from the furnace and was cut in three pieces of approximately 9cm each. The fibres were placed in a resin mixture on a fixed position, preparing them for polishing. The polishing of the fibre was done with fine grade diamond films placed on a rotational polishing machine. The tip of the fibre must be smooth and clean removing any resin debris and residues which can interfere into the EDX measurements. After a smooth polished surface is achieved, the sample is coated with a thin layer of gold. The metal coating prevents charging of the specimen at high

vacuum, which would otherwise occur because of the accumulation of static electric fields. It also increases the number of secondary electrons that can be detected from the surface of the specimen in the SEM and therefore increases the signal to noise ratio.

During polishing, the rotation of the diamond pad creates detachment between the fibre and embedding resin (**Figure 103**). These voids generate conduction issues during EDX analysis and they are the main reason of the electron beam drift and noise introduction to the element concentration percentage. This effect was more intense during the multiple line scanning. To overcome these effects these voids should be filled with a conductive material to provide a path for the incident electrons to flow to ground. After a series of samples, it was managed to overcome and eliminate these problems and present the most reliable data.

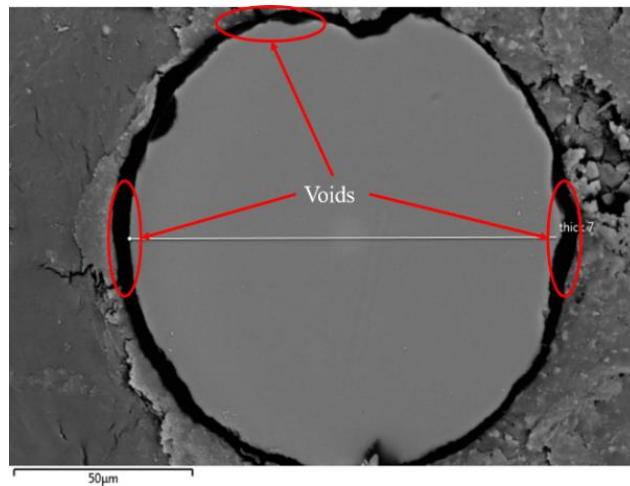


**Figure 103.** SEM photo of a fibre's cross section showing the detachment of the resin from the fibre. The voids are shown in red circles.

#### 5.5.2 Single EDX line scan

In **Table 7** in two columns the quantitative analysis element concentration of the sensor's core in wt. % are presented. These measurements were recorded after a single bombardment of electrons in the centre of the core for the heated and unheated optical fibre. Column (A) shows the element concentration for an unheated optical fibre and column (B) for a heated optical fibre subjected at high temperature cycling for a period of 85 days. At column (A) the germanium concentration in the core is 4.7 wt. %, which corresponds to 0.36% refractive index contrast between the core and the cladding. At column (B) the germanium concentration is 1.9 wt. %, which corresponds to 40% of the initial germanium concentration before heating of the fibre. The presence of gold (Au)

and carbon (C) in **Table 7** is due to the additional materials preparation of the sample for EDX analysis, and can be omitted.

**Table 7. EDX measurements of element detection of Ge-doped sensor's core before and after heating.**

	(A) NON-heated fibre Wt.%	(B) Heated fibre Wt.%
Si	33	32.6
Au	30.5	29.4
C	14.4	17.5
O	17.2	18.7
Ge	4.7	1.9

According to Corning's specifications for SMF28 ultra, the refractive index difference between the core and the cladding is 0.36%. In brief, the EDX analysis shows that after the sensor has been at high temperatures for 85 days, the refractive index contrast between the cladding and the core ends up at 0.144%. As the germanium cannot disappear from the optical fibre system, it can be concluded that the 60% of the germanium in the core has diffused to the cladding. A graphical representation of the elemental concentration is depicted in **Figure 104** and **Figure 105**, where they show the EDX analysis of Ge-doped sensor's core, illustrating the detected elements in peaks.

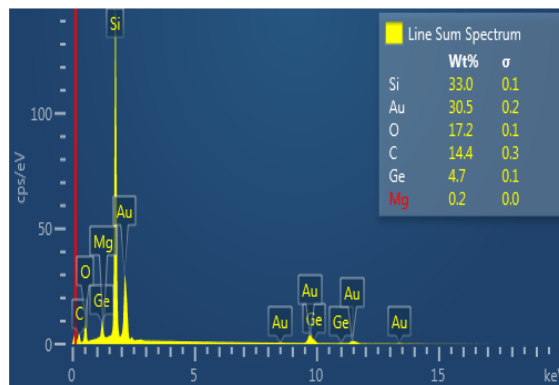


**Figure 104. EDX analysis of the unheated Ge-doped sensor's core before the 85 days stability test.**

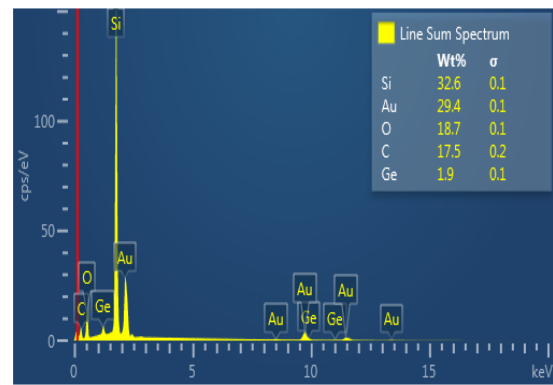


**Figure 105. EDX analysis of the heated Ge-doped sensor's core after the 85 days stability test.**

Then the same samples were tested for germanium concentration detection with a single line scan along the whole diameter of the fibre. At **Figure 106**, a SEM illustration of the Ge-doped sensor's cross section is presented. It depicts the core, the cladding, and the line scan of the EDX analysis. The same SEM/EDX experiment was conducted for the F-doped sensors but there was no detection of fluorine in the core, as the EDX analysis is ineffective at detect elements with an atomic number less than 10. According to the manual of the EDX technique, the standard measurement error is  $\pm 0.1$  wt. %.



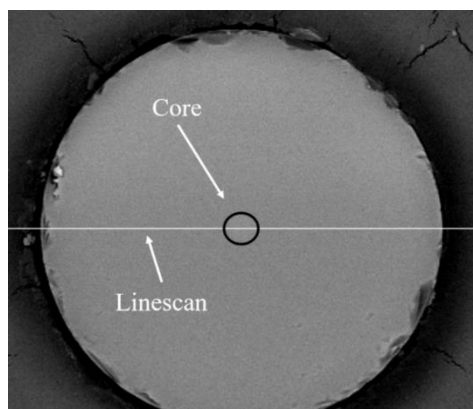


**Figure 106.** SEM photo of the Ge-doped optical fibre sensor, displaying the core, cladding and the line scan of EDX analysis.

In **Figure 107**, the black data correspond to the photon intensity count, of a fibre that has been heated for 85 days at temperatures up to 1100°C, while the blue data correspond to an unheated fibre. Both data sets are smoothed with 10-point averaging to reduce the signal to noise ratio. There is a difference of 150 X-ray photon counts between the two samples' peaks, which is correlated with the dopant diffusion from the core to the cladding. In **Figure 107** there is an evident difference between the wings of the plots, as well. The blue data plot (unheated fibre) has a sharper distribution with 5 $\mu$ m FWHM, whereas the black plot (heated fibre) shows a wider distribution of Ge with a of 8 $\mu$ m FWHM. After integrating the areas beneath the curves, the results show that the total doping is equal, for heated and unheated fibre, within ~14 $\mu$ m region of the core. In effect, the germanium dopant has diffused a short distance, increasing the core radius by 3 $\mu$ m, outwards into the cladding and spreading the refractive index profile.

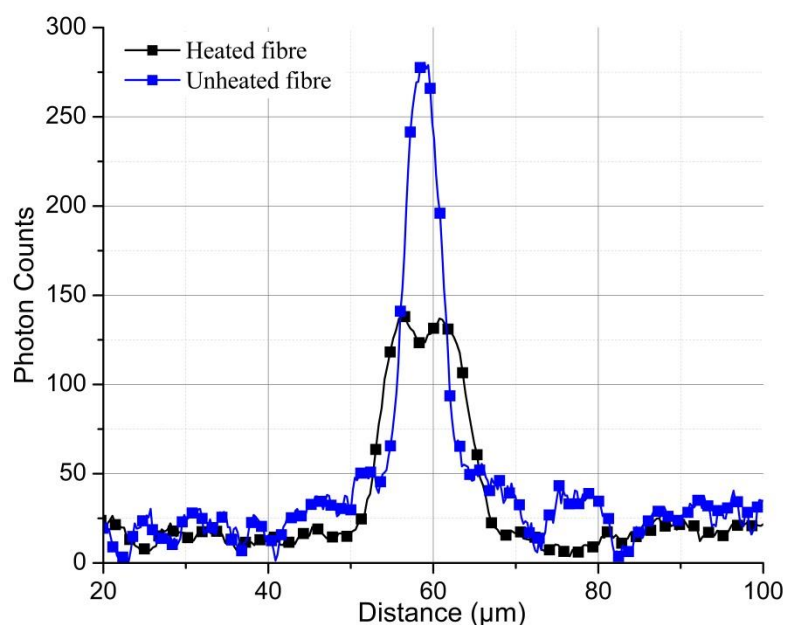


**Figure 107.** Wt. % detection throughout a single line scan with EDX analysis technique of Ge-doped sensor, before and after the stability test. X-axis represents the diameter of the optical fibre.



Another F-P optical fibre sensor remained within a temperature range up to 1050°C for approximately 90 days has been tested with EDX analysis. In this case, **Figure 108** demonstrates the germanium weight concentration percentage of both heated and unheated position of the optical fibre, after being fitted with a Gaussian function and then smoothed with a 10-point averaging. In **Figure 108**, the weight concentration difference between the fibres is 15%, which is less than the one shown in **Figure 107**. In addition, the measured FWHM of the unheated fibre is 4.86 $\mu\text{m}$  while for the heated fibre is 6.29 $\mu\text{m}$ . This is an evidence that the core diameter enlarges approximately 30% on top of its initial diameter. An unheated core diameter is 8.2 $\mu\text{m}$  at which corresponds to 4.86 $\mu\text{m}$  FWHM, according to that the calculated FWHM of 6.29 $\mu\text{m}$  indicates a core diameter of 10.8 $\mu\text{m}$ . This suggests that the germanium is diffusing towards the cladding of the fibre, due to thermal diffusion effects.

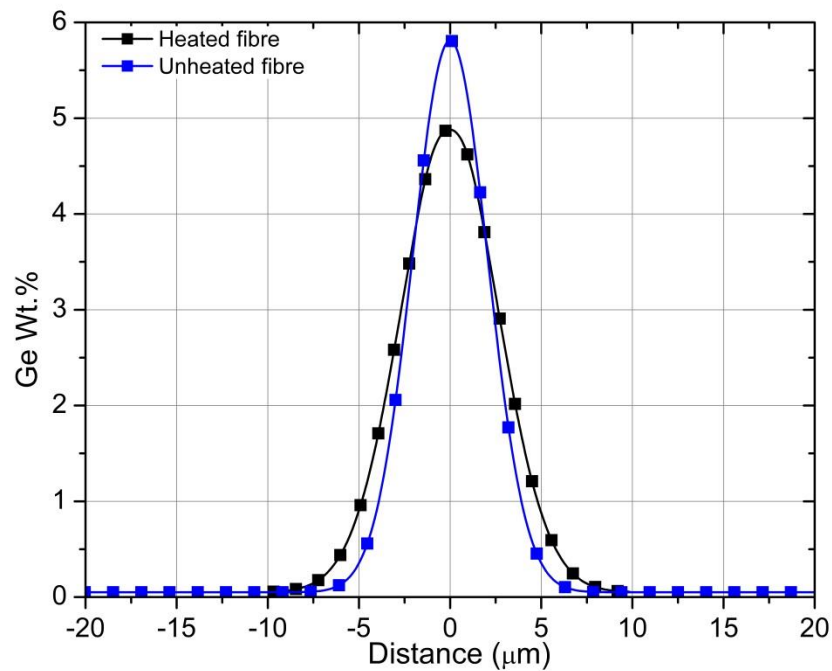


**Figure 108.** Wt. % detection throughout a single line scan with EDX analysis of the heated (black line) and unheated (blue line) Ge-doped optical fibre. Both data were smoothed with a 10-point averaging.

### 5.5.3 Multiple EDX line scan

Multiple line scans for germanium detection along the full area of the fibre's core, were applied. In **Figure 109**, a SEM image displays the EDX series of line scans that were applied on the core area is depicted. The spacing between the line scans is 2 $\mu\text{m}$  at the edges and 1 $\mu\text{m}$  in the centre, of the red block shown in the inset of **Figure 109**. In that way, is presented a complete estimation of the germanium across the full core area and the adjacent cladding.

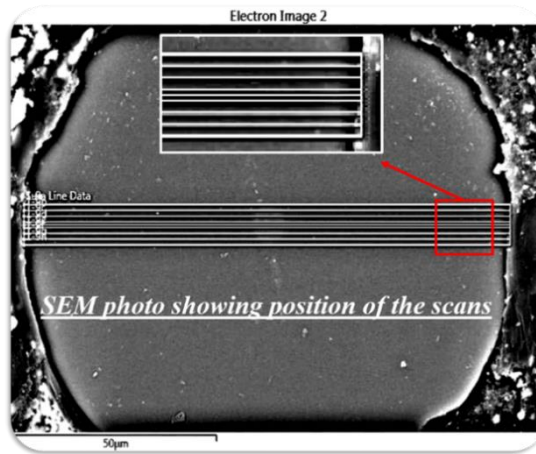


**Figure 109.** SEM photo displays the multiple line scans of core's full area. In the inset graph is depicted a maximized view of multiple line scans.

An optical fibre sensor was removed from the furnace and was cut in three pieces of 9cm each. **Figure 110** shows each piece of the fibre represents a specific position in the furnace. Thus, position 1 is the tip of the sensor which was exposed to the maximum heating ( $1021^{\circ}\text{C}$ ), position 2 is the middle of the fibre ( $985^{\circ}\text{C}$ ) and position 3 was kept at room temperature ( $25^{\circ}\text{C}$ ) throughout the stability tests.

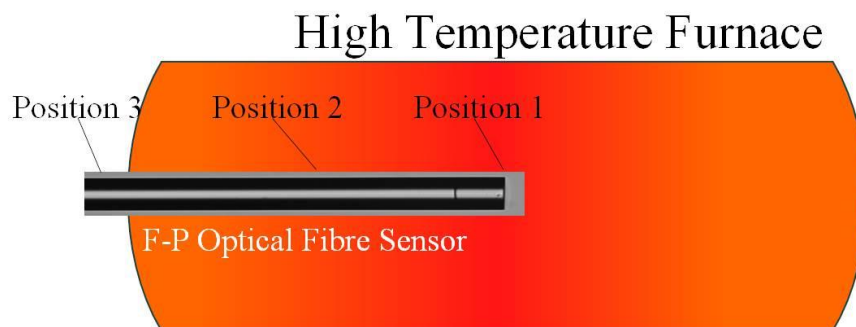
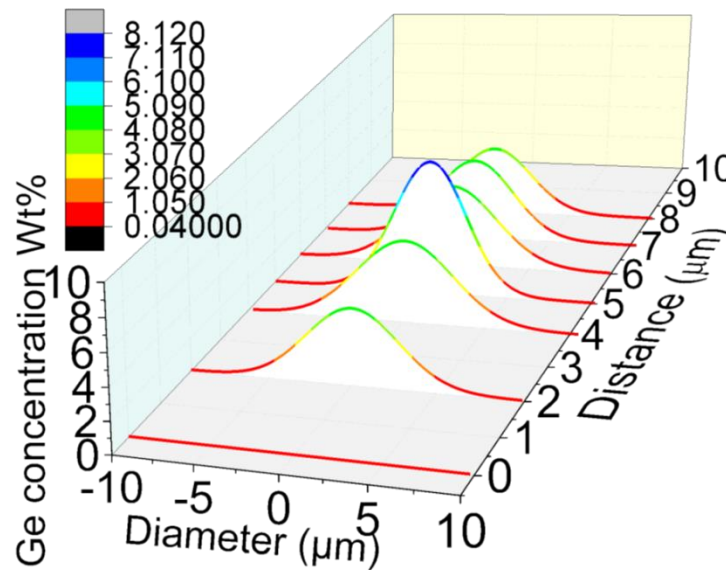


**Figure 110.** Optical fibre's positions in furnace that have been used for EDX analysis.

The F-P optical fibre sensor that has been used for the multiple line scan diffusion analysis has been tested in a range of temperatures between  $900^{\circ}\text{C}$  and  $1050^{\circ}\text{C}$ , over 100 days. **Figure 111**, **Figure 112** and **Figure 113** portray the germanium percentage concentration covering the full area of optical fibre's core. Each graph represents the different longitudinal position of the heated fibre. **Figure 111** shows the germanium percentage (wt. %) of the unheated fibre at position 3. **Figure 112** and **Figure 113** represent the germanium percentage (wt. %) of the heated fibre at position 2 and position 1, respectively.

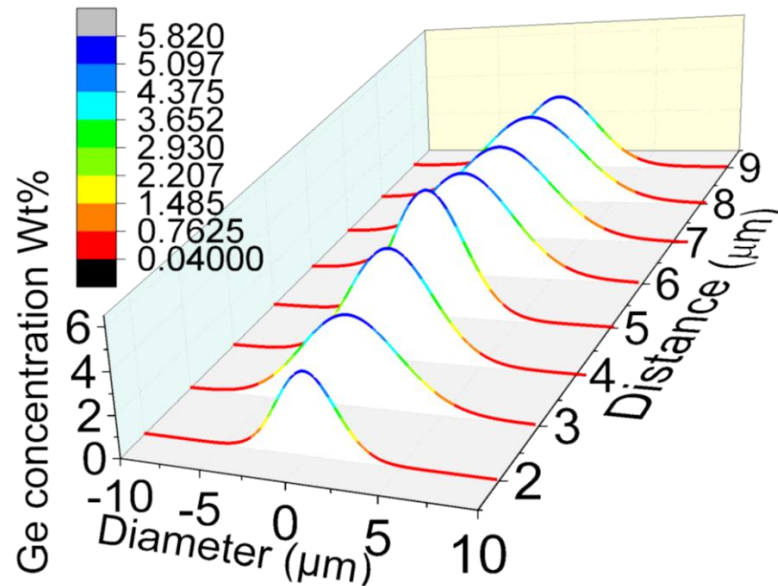
According to optical fibre core expanded tapering theory the relationship of each fibre's position in the furnace with the dopant diffusion is directly connected *via* the temperature gradient of the furnace temperature profile illustrated in 5.1. It is expected the fibres that have been exposed to high temperatures (position 2 and position 1) to

exhibit a wide germanium distribution along the core and show low peak germanium concentration in the centre of the core.



**Figure 111.** Display of core's germanium concentration percentage of position 3, correlated with the unheated optical fibre (25°C). Y axis corresponds to distance label and has been stretched for clarity.

On the other hand, fibres that have not been heated at all (position 3), they will keep a steep germanium distribution with the highest peak sitting at the centre of their core. This is obvious (**Figure 111**) where the unheated fibre (position 3) is presented. The detected germanium concentration in the centre of the core is 8.1 wt. % showing the highest peak compared to its lateral line scans. The fibre at this position holds a stepped index profile which is not visible due to accuracy limitations of the line scan technique. Also, the electron beam drifting had to overpassed as line scans that lie close to each other made the multiple line scan procedure.



**Figure 112.** Display of core's germanium concentration percentage of position 2, correlated with the heated optical fibre (985°C). Y axis corresponds to distance label and has been stretched for clarity.

In **Figure 112**, the germanium concentration of position 2 of the optical fibre is depicted. The highest peak of germanium concentration is approximately 5.8 wt. % in the centre of the core, which corresponds to the 70% of the initial core germanium concentration, according to rough calculations. This can be seen at the lateral line scans around the core in **Figure 112**, where their germanium concentration has a minimum difference with the concentration in its core. This is an adequate evidence which validates the transformation of a stepped index profile to a graded index profile, while in the same time tapered expansion of the core's diameter takes place.

As expected, the germanium concentration for the position of fibre (position 3) which has been heated the most shows the lowest peak in contrast to previous fibre positions that have been analysed. In **Figure 113** the broadened germanium distribution around the centre of the core (approximately at 5μm distance - Y axis) can be seen. The germanium concentration is 4.9 wt. % in the centre of the core, while the lateral line scans show a similar value of concentration. Comparing the initial germanium concentration of position 3 with the concentration of position 1, it can be concluded that high temperatures diffused germanium leaving the centre of the core with 60% of its initial concentration. The rest 40% was diffused towards the cladding transforming the optical fibre to a graded index profile.

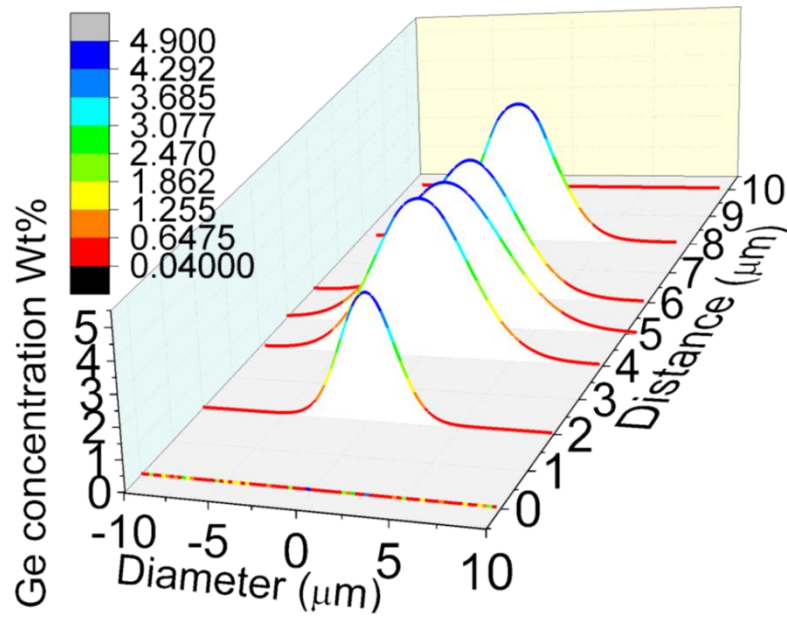


**Figure 113.** Display of core's germanium concentration percentage of position 1, correlated with the heated optical fibre (1021°C). Y axis corresponds to distance label and has been stretched for clarity.

The multiple line scans of core and cladding germanium concentration profile raised the opportunity to detect the maximum dopant concentration along the whole surface of fibre's cross section. Through this we eliminated the errors of manual single line scan selection, which could end up comparing concentrations of different distances along fibre's cross section. From the abovementioned results, the maximum germanium concentration sits in the centre of the core. As it is expected, position 1 has the minimum germanium dopant concentration (4.86 wt. %) while position 3 shows the highest germanium dopant concentration (8.1 wt. %).

**Figure 114** presents the core germanium concentration with respect to fibre radius, for the three positions of the same fibre, giving a metric estimation of the germanium distribution of each fibre's position. In the same figure, the blue data correspond to position 3 while the red data and black data correspond to position 2 and position 3, respectively. In the label is displayed the recorded temperature of the furnace at which corresponds each fibre's position, after setting the furnace at a maximum temperature of 1021°C.

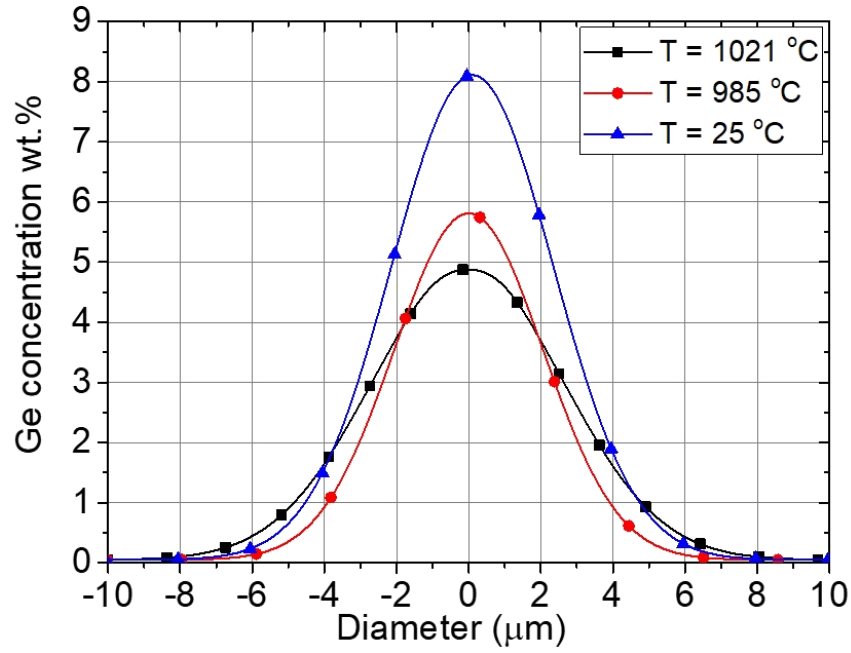


*Figure 114. Germanium concentration at the centre of the core of position 1 (black square data), position 2 (red circle data) and position 3 (blue triangle data) of the fibre with respect to fibre's radius.*

In **Figure 115**, a representation of the peak germanium concentration of core's centre (**Figure 114**) with respect to the longitudinal position of the optical fibre sitting in the furnace is presented. On the X-axis from the left to the right is depicted the depth of the furnace cylindrical tube, meaning that in longer lengths the temperature is higher. The beginning of the X-axis corresponds to the unheated piece of the fibre which is out of the furnace tube. An exponential fitting was applied to the experimental data, which is in accordance with the exponential temperature profile of the furnace.



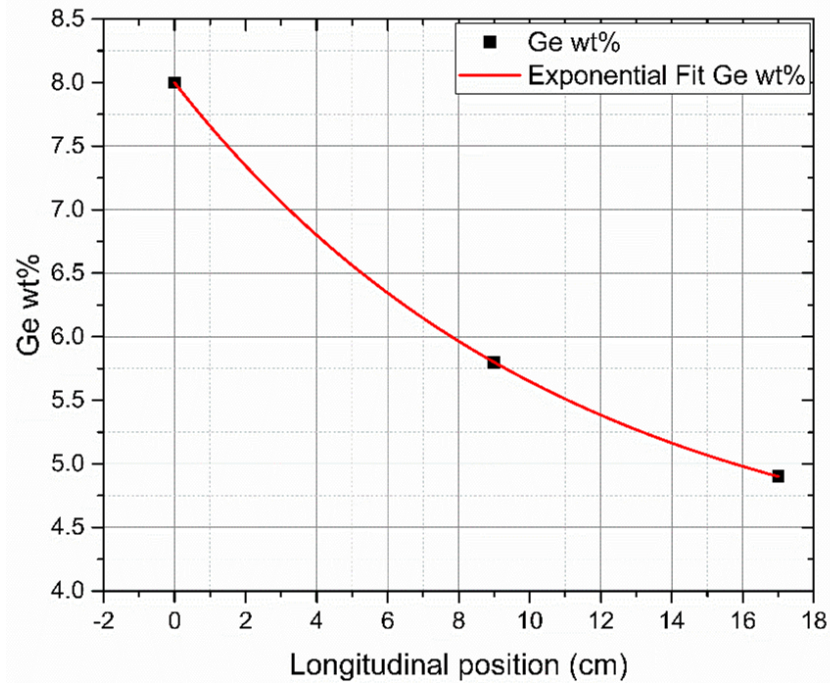


**Figure 115.** Germanium concentration with regards to optical fibre's longitudinal position placed in the furnace. At 17cm sits the heated position 1 fibre, while at 0cm the unheated position 3 fibre.

**Figure 116** and **Figure 117** illustrate the calculated FWHMs of the germanium concentration profile for both position 3 and position 1, respectively. Due to limitations at the EDX analysis line scans it was difficult to decrease their distance less than 1 $\mu$ m, increasing in this way the accuracy of our measurements. Thus, the short sample of data points at FWHM of each line scan reduces the accuracy of the Gaussian fitting at both figures.

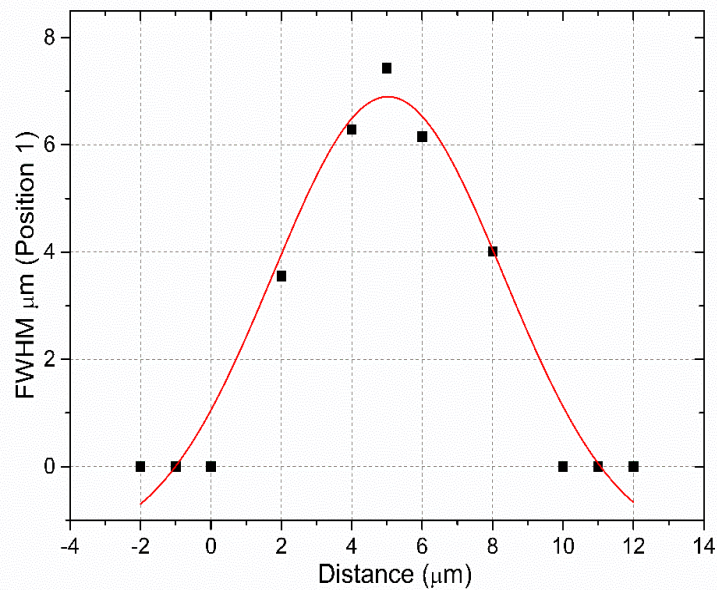


**Figure 116.** Gaussian fit of each line scan's FWHM of position 3 with respect to distance. Distance in X-axis denotes the distance fibre's diameter of the stretched Y-axis of Figure 111.

Additionally, a Gaussian fit to the FWHM profile of **Figure 116** and **Figure 117** is applied, which simulates the overall FWHM of the germanium distribution profile for each fibre position. In the insets of both figures, they can be seen the fitted values of the Gaussian fit. Although, the Gaussian fit at both figures is not very accurate, it does provide a suitable metric to compare the diffusion of germanium at each position.

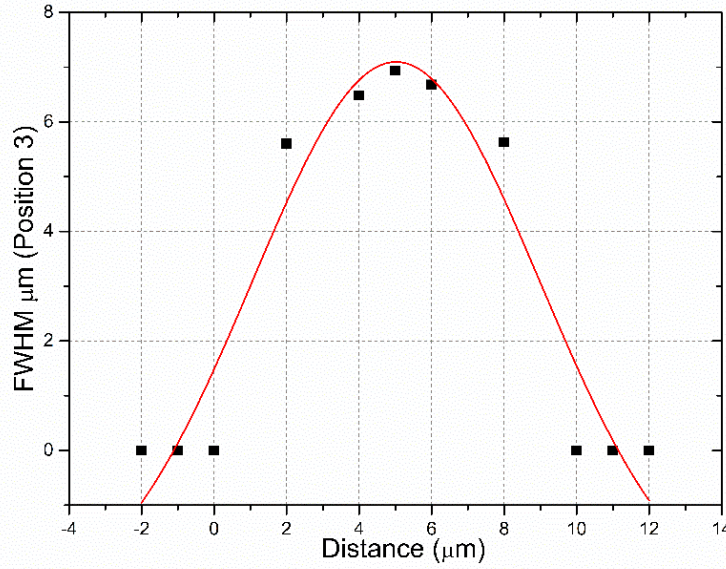


**Figure 117.** Gaussian fit of each line scan's FWHM of position 1 with respect to distance. Distance in X-axis denotes the distance fibre's diameter of the stretched Y-axis of Figure 113.

In **Figure 118** the calculated FWHM of each position of the same fibre, corresponding to dopant diffusion plotted against maximum temperature is presented. Position 1 of the fibre (**Figure 117**) has been exposed to the highest temperature, and it is characterized by the highest FWHM value (FWHM=9.32μm) among the three positions. On the other hand, position 3 (**Figure 116**), which has been unheated, should have the minimum FWHM value (FWHM=7.7μm). In **Figure 118**, was applied an exponential fitting estimating the behaviour of the diameter's broadening due to diffusion. Considering that the overall FWHM of an unheated fibre is 7.7μm, it can be calculated the core increase for the heated fibre with a FWHM of 9.32μm. The result is a 20% increase at the overall FWHM, meaning that the core diameter of the fibre has been broadened by the same amount due to dopant diffusion. In the same way, the 20% increase of FWHM leads to a rough estimation of core's radius increase from  $\alpha=4.1\mu\text{m}$  to  $\alpha=5\mu\text{m}$ . This then corresponds to the final radius of the fibre after being heated for 100 days at temperatures up to 1100°C. In addition, **Figure 118** shows the exponential behaviour of the FWHM agreeing with the furnace temperature profile which shows an exponential decrease form the centre towards its edge.



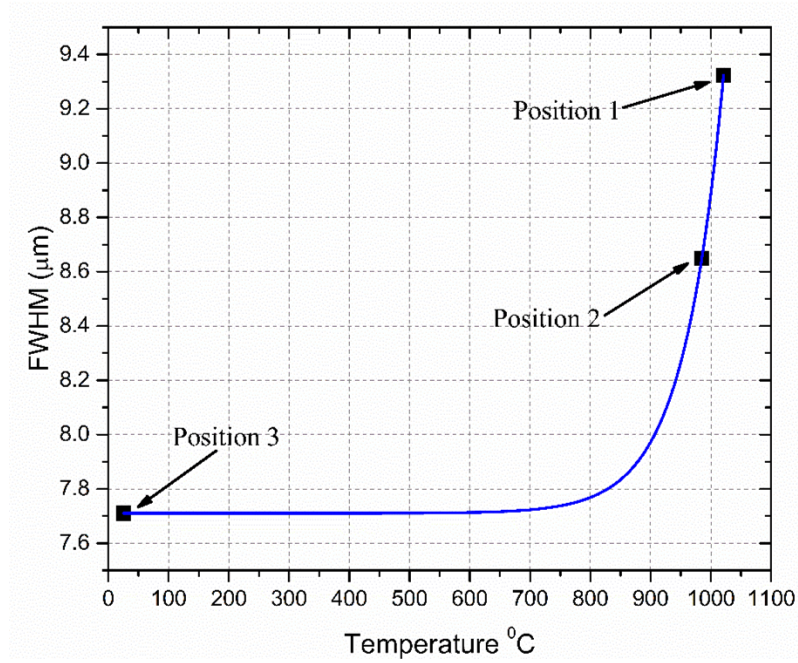


**Figure 118.** FWHM of core's germanium distribution for each fibre with respect to temperature, fitted with an exponential function.

## 5.6 Conclusions of Chapter 5

A thorough investigation, based on multiple EDX line scanning, extracting the germanium wt. % concentration and FWHM determination was presented. The investigation was applied on both heated and unheated pieces of the same fibre. Through theoretical calculations it was concluded that dopant diffusion and tapering due to exposure of the optical fibre to high temperatures, can lead to an introduction of a 2<sup>nd</sup> order mode cavity in the sensing element cavity of F-P sensor. The result is the introduction of a 2<sup>nd</sup> order mode (LP<sub>11</sub>) in the interference signal of the fundamental mode (LP<sub>01</sub>), generating a modulated phase behaviour during annealing and thermal cycling of the F-P optical fibre sensor.

An Energy Dispersive X-ray Spectroscopy (EDX) analysis on the germanium doped sensors has been accomplished to investigate the diffusion of germanium from the core to the cladding, after the sensor has been subjected to high temperatures. As a result, the germanium concentration in the core of the sensor has been dropped down to the 60% of the initial dopant concentration, after 85 days at temperatures above 900°C. Also, a multiple line scan EDX analysis of another set of heated fibres which were tested in a range of temperatures between 900°C and 1050°C over 100 days, gave similar results close to 60%. Through calculations of FWHM and germanium wt. % concentration the 40% of germanium dopant that have been diffused towards the cladding expanded the core radius by 0.9μm.

The result is a broadened core diameter of 10 $\mu$ m which can support a 2<sup>nd</sup> order mode cavity, according to our theoretical calculations. Thus, germanium dopant diffusion affects the core radius by making it larger, which can lead to expanding tapering phenomena and transformation of the single mode core to a multimode core, for specific wavelengths. Complementary to phase transition point and crystallization of fused silica at high temperatures, dopant diffusion can be an additional reason of F-P sensor's phase drifting at high temperatures.

## Chapter 6: Conclusions and Future Work

### 6.1 Conclusions and Discussion

The essence of this thesis is based on the optical fibre sensing field, aiming to make robust and reliable intrinsic Fabry-Pérot optical fibres for high temperature sensing. The characteristics and basic principles of optical fibres sensors were outlined. Optical fibres made of fused silica ( $\text{SiO}_2$ ) material, proved to be an excellent candidate for high temperature sensing applications. However, temperatures above  $1000^\circ\text{C}$  proved to have a huge impact on Fabry-Pérot sensors' phase stability response. The reason is the inwards or outwards dopant diffusion between optical fibre regions, depending on Fabry-Pérot sensor's optical fibre type, which affects the phase response stability of the Fabry-Pérot sensor. Different types of intrinsic Fabry-Pérot optical fibre sensors ( $125\mu\text{m}$ -Cr- $125\mu\text{m}$  diameter formation) were manufactured with sensing elements made by Ge-doped core, F-doped depressed cladding and pure  $\text{SiO}_2$ .

Following to the objectives that have been outlined at the begin of this thesis, a thorough investigation of Fabry-Pérot optical fibre sensors in a temperature range between  $850^\circ\text{C}$  and  $1100^\circ\text{C}$  very encouraging and promising results. The highest temperature at which long-term stability has been achieved was  $1000^\circ\text{C}$  for Fabry-Pérot sensors with Ge-doped and pure  $\text{SiO}_2$  sensing elements. Their resolution at that high temperature range was less than  $5^\circ\text{C}$  for a 1 sec measurement time, while for a 10-data points measurement average ( $\sim 1\text{Hz}$ ) dropped down to less than  $<2^\circ\text{C}$ .

**Table 8. Temperature drifts of different type of Fabry-Pérot sensors.**

<u>Temperature</u> <u>Type of sensor</u>	<b><i>1050°C</i></b> <i>(over 5 days)</i>	<b><i>1000°C</i></b> <i>(over 5 days)</i>	<b><i>900°C</i></b> <i>(over 8 days)</i>
<b><i>Ge-doped core SMF28 ultra</i></b>	<i>18.1°C</i>	<i>9°C</i>	<i>4°C</i>
<b><i>Pure fused silica – PCF</i></b>	<i>11.4°C</i>	<i>&lt;1°C</i>	<i>&lt;1°C</i>
<b><i>F-doped depressed cladding</i></b> <b><i>F-SM1500SC-P</i></b>	<i>&gt;100°C</i>	<i>&gt;100°C</i>	<i>&lt;10°C</i>

The long-term phase response stability results in a temperature range between  $850^\circ\text{C}$  and  $1150^\circ\text{C}$  for periods up 4 months, showed that Ge-doped core and pure  $\text{SiO}_2$  Fabry-Pérot sensors can be used for reliable temperature measurements for 5 days up to  $1000^\circ\text{C}$  with a temperature drift less than  $9^\circ\text{C}$  and  $1^\circ\text{C}$ , respectively. The temperature drift of each sensor can be seen in **Table 8**. In details, a temperature drift less than  $4^\circ\text{C}$  was achieved at ambient temperatures below  $950^\circ\text{C}$ . In the same way, pure  $\text{SiO}_2$  sensing

element Fabry-Pérot sensors' overall performance showed a temperature drift less than 1°C at 1000°C and 900°C over 5 and 8 days, respectively. These sensors exhibited the same temperature drift for temperatures below 1000°C up to 8 days giving the most satisfying stability results. On the other hand, high instability at the phase response has been noticed for F-doped depressed cladding Fabry-Pérot sensors at temperatures above 900°C, achieving a minimum temperature drift of 7°C at 850°C over 7 days. However, it should be noticed that all Fabry-Pérot sensors presented better phase response stability when a stability test cycle was preceded reaching up to 1100°C.

A challenging objective that has been investigated was the insufficiency of Fabry-Pérot sensors for the long-term performance stability at temperatures higher than 1000°C. The results showed that above 1000°C, the sensors proved to be highly unstable, with large discrepancies and unpredictable phase drifts in response. Ge-doped core and F-depressed cladding Fabry-Pérot sensors exhibited in common some characteristics during their stability tests. A phase difference between the same temperatures of a different stability cycle (phase response with respect to time) was visible to both Ge-doped and F-depressed cladding sensors. Complementary to this, similar phase differences were noticed between thermal cycles (phase response versus temperature) at different periods during a long-term stability test. On the other hand, these phase differences were eliminated or negligible at the pure SiO<sub>2</sub> sensors. This is attributed to the lack of dopant in their sensing element, which improved their phase response stability over time exhibiting low temperature drift results. The outcome is that the phase differences proved to be highly correlated with the permanent change of core's refractive index of the sensor due to dopant diffusion. Fluorine's diffusion rate is much faster than germanium's, hence its diffusion in the core affected its refractive index causing phase drifting even in the beginning of a stability test. Further analysis using multiple lines scanning of a heated germanium doped optical fibre cross section validated that the germanium concentration in the core of the sensing element was dropped down to the 60% of its initial dopant concentration. The germanium concentration of three positions, of the same optical fibre, showed that the position which was sitting in the centre of the furnace had 4.9 wt.% germanium concentration. The position of the fibre that was sitting at a quarter of the total length of the furnace showed 5.8 wt.% germanium concentration and the position outside of the furnace, referred as unheated, showed a germanium concentration of 8.1 wt.%. These fibres stayed for 85 days at temperatures above 900°C.

In addition, another effect that has been noticed to all types of Fabry-Pérot sensors was a modulated behavior at the phase response versus temperature graphs. The phase modulations made their appearance after different periods for each type of sensor, due to the different diffusion rate of sensing element's dopant. Our theoretical model's calculations confirmed that these phase modulations emanate from a partial coupling of total power to the 2<sup>nd</sup> order mode (LP<sub>11</sub>), and its introduction in the interference signal of the fundamental cavity mode (LP<sub>01</sub>). The most intense phase modulations occurred at the pure SiO<sub>2</sub> sensor, as its sensing element does not consist of a core and the light is not waveguided in it. Due to this, a 2<sup>nd</sup> order mode cavity is more possible to interfere. The dopant diffusion caused an enlargement of the optical fibre core's diameter transforming its refractive index profile from stepped to graded, and consequently from single mode to multimode for specific wavelengths. This agrees with the experimental diffusion results, as the mapping of germanium distribution of a heated optical fibre's cross section proved that the stepped index profile was transposed to graded index profile. The 40% of germanium in the core was diffused towards the cladding, enlarging core's diameter by 1.8µm. The result was a broadened core diameter of 10µm which enables the support a 2<sup>nd</sup> order mode cavity, agreeing with our theoretical calculations. Finally, the experimental results confirmed that the core diameter is exponentially increased in a tapered formation, longitudinal to the waveguiding optical fibre. The exponential formation comes from the exponential temperature profile of the furnace.

The conclusion is that long-term exposure of optical fibres to high temperatures causes inwards/outwards dopant diffusion to the core/cladding, respectively, and consequently an irreversible change in the fibre properties, gradually transforming the stepped refractive-index profile to a graded shape profile. As long as most optical fibres are doped with various elements for refractive index modification, it must be considered that dopant diffusion will lead to expanded core tapering phenomena and refractive index profile transformation. These effects are significantly enhanced at temperatures higher than 1000°C. The new contribution to knowledge addressed in this thesis is the successful long-term stability performance, up to 4 months, of Fabry-Pérot optical fibre sensors. Despite the various temperature drifts the sensors exhibited, at different temperature ranges, they were still operational at the end of these long-term stability tests. In addition, EDX multiple cross section linescan of optical fibre sensors is considered an innovative technique for dopant diffusion detection. This technique has

been used successfully applied to estimate dopant's percentage in the core and the cladding before and after the long-term stability tests.

## 6.2 Future Work

Dopant in the Fabry-Pérot sensing element has been eliminated by replacing it with a pure SiO<sub>2</sub> cavity. A feasible type of sensor of 125µm-Cr-125µm formation (type 1) with a 100µm diameter sapphire (Al<sub>2</sub>O<sub>3</sub>) sensing element could be manufactured. Some preliminary work has been conducted on welding and cutting a sapphire (Al<sub>2</sub>O<sub>3</sub>) disk onto a 125µm diameter SMF28 ultra optical fibre with ultrashort picosecond laser pulses. The sapphire fibre or disk cannot be spliced with the custom fibre splicing techniques, such as filament or arc fusion splicers due to its hardness. Instead, it could be welded to the tip of an optical fibre by high precision ultrashort laser micromachining, making in this way a robust Fabry-Pérot sensor for temperature monitoring above 1100°C. **Figure 119** shows a schematic diagram of the Fabry-Pérot sensor's integration. The sapphire crystal is characterized by high temperature melting point (2040°C) of no porosity or grain boundaries.

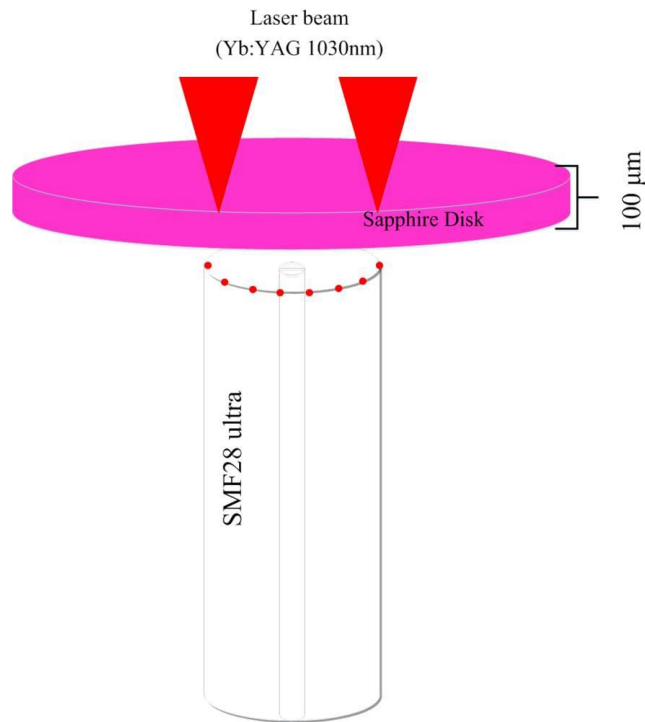


**Figure 119.** Schematic diagram of laser welding and cutting of a sapphire disk onto an optical fibre for intrinsic Fabry-Pérot optical fibre integration.

The goal of intrinsic Fabry-Pérot optical fibre sensors is their embedment in metallic structures, so that the sensors will be capable to temperature sensing from within a metallic component. The optimum sensor formation for encapsulation is the

stepped diameter Fabry-Pérot sensor (type 2). The small diameter (50 $\mu$ m) of the sensing element is excellent choice for encapsulation in fused silica capillaries.

Nevertheless, two challenges for future work should be considered. The first challenge is the manufacturing process which is time consumable, due to the many splicing-cleaving stages of fibres with different diameters. The manufacturing process of a single stepped Fabry-Pérot sensor needs very precise work for almost a day. An idea for elimination of these problems it would be the use of HF etching solution in replacement of the time consumable splicing and cleaving procedure. This can be succeeded by using a bundle of 125 $\mu$ m diameter SMF28 ultra optical fibres and submerge them in acid solution causing homogeneous decrease of diameter. Hence, the elimination of multiple splicing-cleaving steps, massive production of sensors and homogeneous sensors of the same SMF28 optical fibre can be achieved. By achieving that, the only remaining stages will be the chromium deposition on the 50 $\mu$ m diameter fibre and the splice of the 50 $\mu$ m diameter sensing element. The second challenge should be the 50 $\mu$ m diameter doped sensing element, which ideally could be replaced by a pure undoped material, such as sapphire. The welding and cutting technique with ultrashort picosecond laser pulses could be used effectively for the integration of a homogeneous stepped intrinsic Fabry-Pérot optical fibre sensor.

## REFERENCES

- [1] O. Strobel, "Introduction," *Optical and Microwave Technologies for Telecommunication Networks*, pp. 1-9: John Wiley & Sons, Ltd, 2016.
- [2] M. S. Ferreira, P. Roriz, S. O. Silva *et al.*, "Next generation of Fabry-Perot sensors for high-temperature," *Optical Fiber Technology*, vol. 19, no. 6, pp. 833-837, 2013.
- [3] C. E. Lee, A. M. Markus, E. Udd *et al.*, "Optical-fiber Fabry-Perot embedded sensor," *Optics Letters*, vol. 14, no. 21, pp. 1225, 1989.
- [4] S. P. Library, "Optical Fibre Threaded Pictures and Images," F. o. a. needle, ed., gettyimages, 2017.
- [5] K. Osenbach. "Custom Fiber Optic Patch Cables " 2017; [https://www.thorlabs.de/newgrouppage9.cfm?objectgroup\\_id=2410](https://www.thorlabs.de/newgrouppage9.cfm?objectgroup_id=2410).
- [6] S.-P. Jeng, "Anomalous diffusion of fluorine in silicon."
- [7] M. V. Minke, and K. A. Jackson, "Diffusion of germanium in silica glass," *Journal of Non-Crystalline Solids*, vol. 351, no. 27-29, pp. 2310-2316, 2005.
- [8] X. Li, "Embedded sensors in layered manufacturing," Mechanical engineering of stanford university, stanford university, 2001.
- [9] D. Havermann, "Study on Fibre Optic Sensors Embedded into Metallic Structures by Selective Laser Melting," Engineering & Physical Sciences Heriot Watt University, 2015.
- [10] J. Mathew, C. Hauser, P. Stoll *et al.*, "Integrating fibre Fabry-Perot cavity sensor in to 3D printed metal components for extreme high temperature monitoring applications," *IEEE Sensors Journal*, vol. 17, no. 13, pp. 1-1, 2017.
- [11] J. Mathew, O. Schneller, D. Polyzos *et al.*, "In-Fiber Fabry-Perot Cavity Sensor for High-Temperature Applications," *Journal of Lightwave Technology*, vol. 33, no. 12, pp. 2419-2425, 2015/06/15, 2015.
- [12] K. T. V. Grattan, and T. Sun, "Fiber optic sensor technology: an overview," *Sensors and Actuators A: Physical*, vol. 82, no. 1-3, pp. 40-61, 5/15/, 2000.
- [13] O. Strobel, "Fiber Manufacturing, Cabling and Coupling," *Optical and Microwave Technologies for Telecommunication Networks*, pp. 75-138: John Wiley & Sons, Ltd, 2016.
- [14] C. E. Lee, W. N. Gibler, R. A. Atkins *et al.*, "Metal-embedded fiber-optic Fabry-Perot sensors," *Optics Letters*, vol. 16, no. 24, pp. 1990, 1991.
- [15] M. Fernandez-Vallejo, and M. Lopez-Amo, "Optical fiber networks for remote fiber optic sensors," *Sensors (Basel)*, vol. 12, no. 4, pp. 3929-51, 2012.
- [16] A. D. Kersey, T. A. Berkoff, and W. W. Morey, "Multiplexed fiber Bragg grating strain-sensor system with a fiber Fabry-Perot wavelength filter," *Optics Letters*, vol. 18, no. 16, pp. 1370-1372, 1993/08/15, 1993.
- [17] K. Iwamoto, and I. Kamata, "Liquid-level sensor with optical fibers," *Applied Optics*, vol. 31, no. 1, pp. 51-54, 1992/01/01, 1992.
- [18] G. Tsagaridas, D. Polyzos, A. Ioannou *et al.*, "Theoretical and experimental study of refractive index sensors based on etched fiber Bragg gratings," *Sensors and Actuators A: Physical*, vol. 209, pp. 9-15, 2014/03/01/, 2014.
- [19] I. Garcia, J. Zubia, G. Durana *et al.*, "Optical Fiber Sensors for Aircraft Structural Health Monitoring," *Sensors (Basel)*, vol. 15, no. 7, pp. 15494-519, Jun 30, 2015.
- [20] J. C. Owens, "Optical refractive index of air: dependence on pressure, temperature and composition," *Appl Opt*, vol. 6, no. 1, pp. 51-9, Jan 1, 1967.
- [21] D. Barrera, V. Finnazi, J. Villatoro *et al.*, "Performance of a high-temperature sensor based on regenerated fiber Bragg gratings," in 21st International Conference on Optical Fiber Sensors, 2011.



- [22] C. E. Lee, R. A. Atkins, and H. F. Taylor, "Performance of a fiber-optic temperature sensor from  $-200$  to  $1050^{\circ}\text{C}$ ," *Optics Letters*, vol. 13, no. 11, pp. 1038-1040, 1988/11/01, 1988.
- [23] F. Mitschke, *Fiber optics : physics and technology*, Berlin ; London: Springer, 2009.
- [24] F. Berghmans, S. Eve, and M. Held, "An Introduction to Reliability of Optical Components and Fiber Optic Sensors," pp. 73-100, 2008.
- [25] N. P. Bansal, and R. H. Doremus, "Chapter 2 - Vitreous Silica," *Handbook of Glass Properties*, pp. 7-30, San Diego: Academic Press, 1986.
- [26] M. I. Ojovan, "Glass formation in amorphous  $\text{SiO}_2$  as a percolation phase transition in a system of network defects," *Journal of Experimental and Theoretical Physics Letters*, vol. 79, no. 12, pp. 632-634, 2004.
- [27] H. Alemohammad, E. Toyserkani, and C. P. Paul, "Fabrication of smart cutting tools with embedded optical fiber sensors using combined laser solid freeform fabrication and moulding techniques," *Optics and Lasers in Engineering*, vol. 45, no. 10, pp. 1010-1017, 2007.
- [28] Y. Zhao, and Y. Liao, "Compensation technology for a novel reflex optical fiber temperature sensor used under offshore oil well," *Optics Communications*, vol. 215, pp. 6, 2003.
- [29] Y. Zhu, Z. Huang, F. Shen *et al.*, "Sapphire-fiber-based white-light interferometric sensor for high-temperature measurements," *Optics Letters*, vol. 30, no. 7, pp. 711-713, 2005/04/01, 2005.
- [30] R. R. Dils, "High-temperature optical fiber thermometer," *Journal of Applied Physics*, vol. 54, no. 3, pp. 1198-1201, 1983.
- [31] T. Zhu, T. Ke, Y. Rao *et al.*, "Fabry-Perot optical fiber tip sensor for high temperature measurement," *Optics Communications*, vol. 283, no. 19, pp. 3683-3685, 2010.
- [32] D. A. a. D. Parande, "Optical sensors and their applications," *Journal of Scientific Research and Reviews*, vol. 1, no. 5, pp. 060 - 068, 2012.
- [33] K. C. Kao, and G. A. Hockham, "Dielectric-fibre surface waveguides for optical frequencies," *Electrical Engineers, Proceedings of the Institution of*, vol. 113, no. 7, pp. 1151-1158, 1966.
- [34] J.-Y. Lin, "Theory and analysis of phase sensitivity-tunable optical sensor based on total internal reflection," *Optics Communications*, vol. 283, no. 24, pp. 4899-4906, 2010/12/15/, 2010.
- [35] E. Udd, "Overview of Fiber Optic Sensors," *Fiber Optic Sensors, Second Edition*, Optical Science and Engineering, pp. 1-34: CRC Press, 2008.
- [36] B. E. A. Saleh, and M. C. Teich, "Fiber Optics," *Fundamentals of Photonics*, pp. 272-309: John Wiley & Sons, Inc., 2001.
- [37] B. Mellish, "Singlemode fibre structure," *.png*, Singlemode\_fibre\_structure, ed., Wikipedia, 2007, p. Diagram of a single mode (SM) optical fiber.
- [38] G. P. Agrawal, "Fiber-Optic Communication Systems," John Wiley & Sons, Inc., 2010, p. 626.
- [39] D. S. Kocijancic. "Light Propagation in Optical Fibres," [http://www.pef.uni-lj.si/eprolab/comlab/sttop/sttop-oe/CHAPTER3/C%203\\_Light%20propagation%20.htm#Attenuation\\_and\\_Dispersion](http://www.pef.uni-lj.si/eprolab/comlab/sttop/sttop-oe/CHAPTER3/C%203_Light%20propagation%20.htm#Attenuation_and_Dispersion).
- [40] K. Fidanboyulu, Efendioğlu, H. S., "Fiber optic sensors and their applications ". p. 6.
- [41] J. M. Senior, "Optical Fiber Communications Principles and Practice - 3rd Edition," pp. 12-20: Pearson - Prentice Hall, 2009.

- [42] D. Gloge, "Weakly Guiding Fibers," *Applied Optics*, vol. 10, no. 10, pp. 2252-2258, 1971/10/01, 1971.
- [43] D. B. S. Soh, J. Nilsson, S. Baek *et al.*, "Modal power decomposition of beam intensity profiles into linearly polarized modes of multimode optical fibers," *Journal of the Optical Society of America A*, vol. 21, no. 7, pp. 1241-1250, 2004/07/01, 2004.
- [44] G. Sagué, A. Baade, and A. Rauschenbeutel, "Blue-detuned evanescent field surface traps for neutral atoms based on mode interference in ultrathin optical fibres," *New Journal of Physics*, vol. 10, no. 11, pp. 113008, 2008.
- [45] R. Jenny, "Fundamentals of Optics - An Introduction for Beginners," *Vision Systems Designs*, 1 February 2001, 2001.
- [46] A. F. Herbster, and M. A. Romero, "Few-mode erbium-doped fiber amplifier design method based on the signal-pump overlap integral," *Optical Engineering*, vol. 53, no. 9, pp. 096101-096101, 2014.
- [47] Mrzeon, "Optical fiber types," *Image:Tipos\_fibra.jpg*, O. f. types, ed., Wikimedia, 2007, p. Optical fiber types
- [48] T. Kato, Y. Suetsugu, and M. Nishimura, "Estimation of nonlinear refractive index in various silica-based glasses for optical fibers," *Optics Letters*, vol. 20, no. 22, pp. 2279-2281, 1995/11/15, 1995.
- [49] D. Marcuse, "Gaussian approximation of the fundamental modes of graded-index fibers," *Journal of the Optical Society of America*, vol. 68, no. 1, pp. 103-109, 1978/01/01, 1978.
- [50] C. Qing, and C. Sien, "Approximate analytical description for fundamental-mode fields of graded-index fibers: beyond the Gaussian approximation," *Journal of Lightwave Technology*, vol. 19, no. 1, pp. 54-59, 2001.
- [51] M. S. D. Kovacevic, A. Nikezic, D. , "Light propagation in thermally expanded core fibers with graded-index," *Optica Applicata*, vol. Vol. 39, no. 2, pp. 267-276, 2009.
- [52] A. Sharma, S. I. Hosain, and A. K. Ghatak, "The fundamental mode of graded-index fibres: simple and accurate variational methods," *Optical and Quantum Electronics*, vol. 14, no. 1, pp. 7-15, 1982.
- [53] M. O. Vassell, "Calculation of propagating modes in a graded-index optical fibre," *Opto-electronics*, vol. 6, no. 4, pp. 271-286, 1974.
- [54] I. H. Malitson, "Interspecimen Comparison of the Refractive Index of Fused Silica," *Journal of the Optical Society of America*, vol. 55, no. 10, pp. 1205-1209, 1965/10/01, 1965.
- [55] G. Ghosh, "Model for the thermo-optic coefficients of some standard optical glasses," *Journal of Non-Crystalline Solids*, vol. 189, no. 1, pp. 191-196, 1995/08/02/, 1995.
- [56] T. Toyoda, and M. Yabe, "The temperature dependence of the refractive indices of fused silica and crystal quartz," *Journal of Physics D: Applied Physics*, vol. 16, no. 5, pp. L97, 1983.
- [57] E. D. Palik, "Chapter 3 - Thermo-Optic Coefficients A2 - Palik, Edward D," *Handbook of Optical Constants of Solids*, E. D. Palik, ed., pp. 115-261, Burlington: Academic Press, 1997.
- [58] G. M. H. Flockhart, R. R. J. Maier, J. S. Barton *et al.*, "Quadratic behavior of fiber Bragg grating temperature coefficients," *Applied Optics*, vol. 43, no. 13, pp. 2744, 2004.
- [59] M. E. Lines, "Physical origin of the temperature dependence of chromatic dispersion in fused silica," *Journal of Applied Physics*, vol. 73, no. 5, pp. 2075-2079, 1993.

- [60] G. Ghosh, "Sellmeier coefficients and dispersion of thermo-optic coefficients for some optical glasses," *Applied Optics*, vol. 36, no. 7, pp. 1540-1546, 1997/03/01, 1997.
- [61] C. O. fibres, "Product Information: Corning Single mode SMF-28 " *Optical fibre*, Corning, 2002.
- [62] N. P. Bansal, and R. H. Doremus, "Chapter 6 - Coefficient of Thermal Expansion," *Handbook of Glass Properties*, pp. 125-178, San Diego: Academic Press, 1986.
- [63] P. K. Bachmann, D. U. Wiechert, and T. P. M. Meeuwsen, "Thermal expansion coefficients of doped and undoped silica prepared by means of PCVD," *Journal of Materials Science*, vol. 23, no. 7, pp. 2584-2588, 1988.
- [64] L. Y. Shao, J. Canning, T. Wang *et al.*, "Viscosity of silica optical fibres characterized using regenerated gratings," *Acta Materialia*, vol. 61, no. 16, pp. 6071-6081, 2013/09/01/, 2013.
- [65] M. I. Ojovan, "Viscosity and Glass Transition in Amorphous Oxides," *Advances in Condensed Matter Physics*, vol. 2008, pp. 1-23, 2008.
- [66] R. Brückner, "Properties and structure of vitreous silica. I," *Journal of Non-Crystalline Solids*, vol. 5, no. 2, pp. 123-175, 1970/11/01/, 1970.
- [67] J. Canning, "Regeneration, regenerated gratings and composite glass properties: the implications for high temperature micro and nano milling and optical sensing," *Measurement*, vol. 79, pp. 236-249, 2016/02/01/, 2016.
- [68] J. Canning, W. Liu, K. E. D. L. C. L. J. J. Y. K. K. T. H. X. K. G. P. Cook *et al.*, "Annealing and Regeneration in Optical Fibres," *OSA Technical Digest (online)*. p. AM3C.2.
- [69] P. Mauron, P. M. Nellen, and U. Sennhauser, "High-Temperature Ageing of Modern Polymer-Coated Optical Fibres," *MRS Proceedings*, vol. 531, 2011.
- [70] M. I. Ojovan, "Ordering and structural changes at the glass-liquid transition," *Journal of Non-Crystalline Solids*, vol. 382, pp. 79-86, 2013/12/15/, 2013.
- [71] J. Kirchhof, S. Unger, K. F. Klein *et al.*, "Diffusion behaviour of fluorine in silica glass," *Journal of Non-Crystalline Solids*, vol. 181, no. 3, pp. 266-273, 1995/02/02/, 1995.
- [72] M. Ogino, Y. Oana, and M. Watanabe, "The Diffusion Coefficient of Germanium in Silicon," *physica status solidi (a)*, vol. 72, no. 2, pp. 535-541, 1982.
- [73] K. Shiraishi, Y. Aizawa, and S. Kawakami, "Beam expanding fiber using thermal diffusion of the dopant," *Journal of Lightwave Technology*, vol. 8, no. 8, pp. 1151-1161, 1990.
- [74] R. Oikari, T. Laurila, and R. Hernberg, "High-temperature effects in fluorine-doped, fused synthetic silica fibers," *Applied Optics*, vol. 36, no. 21, pp. 5058-5063, 1997/07/20, 1997.
- [75] M. Kihara, S. Tomita, and M. Matsumoto, "Loss characteristics of thermally diffused expanded core fiber," *IEEE Photonics Technology Letters*, vol. 4, no. 12, pp. 1390-1391, 1992.
- [76] M. Kihara, M. Matsumoto, T. Haibara *et al.*, "Characteristics of thermally expanded core fiber," *Journal of Lightwave Technology*, vol. 14, no. 10, pp. 2209-2214, 1996.
- [77] B. Hafner, *Energy Dispersive Spectroscopy on the SEM: A Primer*, University of Minnesota, Characterization Facility, 2015.
- [78] A. D. Yablon, "Optical and mechanical effects of frozen-in stresses and strains in optical fibers," *IEEE Journal of Selected Topics in Quantum Electronics*, vol. 10, no. 2, pp. 300-311, 2004.

- [79] F. Hanawa, Y. Hibino, M. Shimizu *et al.*, "Influences of the drawing conditions on optical characteristics in undoped-silica-core single-mode fibers," *Optics Letters*, vol. 12, no. 8, pp. 617-618, 1987/08/01, 1987.
- [80] Y. Hibino, F. Hanawa, and M. Horiguchi, "Drawing-induced residual stress effects on optical characteristics in pure-silica-core single-mode fibers," *Journal of Applied Physics*, vol. 65, no. 1, pp. 30-34, 1989.
- [81] K. Jens, B. Jörg, W. Katrin *et al.*, "Diffusion and Interface Effects during Preparation of All-Solid Microstructured Fibers," *Materials*, vol. 7, no. 9, pp. 6879-6892, 2014.
- [82] J. M. López-Higuera, J. D. C. Jones, M. López-Amo *et al.*, "High temperature sensor based on an in-fibre Fabry-Perot cavity," vol. 9157, pp. 91578L, 2014.
- [83] J. Yi, E. Lally, A. Wang *et al.*, "Demonstration of an All-Sapphire Fabry Perot Cavity for Pressure Sensing," *IEEE Photonics Technology Letters*, vol. 23, no. 1, pp. 9-11, 2011.
- [84] Q. Wu, Y. Semenova, P. Wang *et al.*, "A comprehensive analysis verified by experiment of a refractometer based on an SMF28–small-core singlemode fiber (SCSMF)–SMF28 fiber structure," *Journal of Optics*, vol. 13, no. 12, pp. 125401, 2011.
- [85] M. R. Islam, M. M. Ali, M.-H. Lai *et al.*, "Chronology of Fabry-Perot Interferometer Fiber-Optic Sensors and Their Applications: A Review," *Sensors (Basel, Switzerland)*, vol. 14, no. 4, pp. 7451-7488, 04/24, 2014.
- [86] K. A. Murphy, M. F. Gunther, A. M. Vengsarkar *et al.*, "Quadrature phase-shifted, extrinsic Fabry–Perot optical fiber sensors," *Optics Letters*, vol. 16, no. 4, pp. 273-275, 1991/02/15, 1991.
- [87] a. H. N. Bahareh Gholamzadeh, "Fiber Optic Sensors," *International Journal of Electrical, Computer, Energetic, Electronic and Communication Engineering*, vol. 2, no. World Academy of Science, Engineering and Technology, pp. 1107 - 1117, 2008.
- [88] K. J. Peters, and D. Inaudi, "Fiber optic sensors for assessing and monitoring civil infrastructures," *Sensor Technologies for Civil Infrastructures*, pp. 121-158: Woodhead Publishing, 2014.
- [89] C. Elosua, I. Matias, C. Barriain *et al.*, "Volatile Organic Compound Optical Fiber Sensors: A Review," *Sensors*, vol. 6, no. 11, pp. 1440, 2006.
- [90] M. L. Wang, J. P. Lynch, and H. Sohn, "Introduction to sensing for structural performance assessment and health monitoring," *Sensor Technologies for Civil Infrastructures*, pp. 1-22: Woodhead Publishing, 2014.
- [91] N. C. Yoder, and D. E. Adams, "Commonly used sensors for civil infrastructures and their associated algorithms," *Sensor Technologies for Civil Infrastructures*, pp. 57-85: Woodhead Publishing, 2014.
- [92] A. McDonach, P. D. Foote, P. T. Gardiner *et al.*, "Fibre Bragg grating strain sensors for aerospace smart structures," vol. 2361, pp. 290-293, 1994.
- [93] X. Bao, and L. Chen, "Recent Progress in Distributed Fiber Optic Sensors," *Sensors*, vol. 12, no. 7, pp. 8601, 2012.
- [94] P. J. Shull, G. A. Ferrier, X. Bao *et al.*, "Distributed Brillouin temperature measurements without frequency scanning for dynamic process monitoring," vol. 5393, pp. 66-75, 2004.
- [95] O. Schneller, J. Mathew, W. N. MacPherson *et al.*, "High temperature sensor based on an in-fibre Fabry-Perot cavity." pp. 91578L-91578L-4.
- [96] H. Y. Choi, K. S. Park, S. J. Park *et al.*, "Miniature fiber-optic high temperature sensor based on a hybrid structured Fabry–Perot interferometer," *Optics Letters*, vol. 33, no. 21, pp. 2455-2457, 2008/11/01, 2008.

- [97] C. Lin, Y. Q. Huang, W. Lei *et al.*, "A Novel Fabry-Perot Cavity Fiber Sensor," *Physics Procedia*, vol. 33, pp. 1939-1946, 2012/01/01/, 2012.
- [98] X. Wan, and H. F. Taylor, "Intrinsic fiber Fabry-Perot temperature sensor with fiber Bragg grating mirrors," *Optics Letters*, vol. 27, no. 16, pp. 1388-1390, 2002/08/15, 2002.
- [99] S.-C. Huang, W.-W. Lin, M.-T. Tsai *et al.*, "Fiber optic in-line distributed sensor for detection and localization of the pipeline leaks," *Sensors and Actuators A: Physical*, vol. 135, no. 2, pp. 570-579, 2007/04/15/, 2007.
- [100] S. Liu, Y. Wang, C. Liao *et al.*, "High-sensitivity strain sensor based on in-fiber improved Fabry- Perot interferometer," *Optics Letters*, vol. 39, no. 7, pp. 2121-2124, 2014/04/01, 2014.
- [101] X. Y. Zhang, Y. S. Yu, C. C. Zhu *et al.*, "Miniature End-Capped Fiber Sensor for Refractive Index and Temperature Measurement," *IEEE Photonics Technology Letters*, vol. 26, no. 1, pp. 7-10, 2014.
- [102] M.-s. Jiang, Q.-m. Sui, Z.-w. Jin *et al.*, "Temperature-independent optical fiber Fabry-Perot refractive-index sensor based on hollow-core photonic crystal fiber," *Optik - International Journal for Light and Electron Optics*, vol. 125, no. 13, pp. 3295-3298, 2014/07/01/, 2014.
- [103] W. Wang, and F. Li, "Large-range liquid level sensor based on an optical fibre extrinsic Fabry-Perot interferometer," *Optics and Lasers in Engineering*, vol. 52, pp. 201-205, 2014/01/01/, 2014.
- [104] A. Kaur, S. E. Watkins, J. Huang *et al.*, "Microcavity strain sensor for high temperature applications," *Optical Engineering*, vol. 53, no. 1, pp. 017105-017105, 2014.
- [105] G. Zhang, M. Yang, and Y. Wang, "Optical fiber-tip Fabry-Perot interferometer for hydrogen sensing," *Optics Communications*, vol. 329, pp. 34-37, 2014/10/15/, 2014.
- [106] H. Taylor, "Fiber Optic Sensors Based upon the Fabry-Perot Interferometer," *Fiber Optic Sensors, Second Edition*, Optical Science and Engineering, pp. 35-64: CRC Press, 2008.
- [107] Z. Yinan, L. Yanjun, W. Tao *et al.*, "Fringe Visibility Enhanced Extrinsic Fabry-Perot Interferometer Using a Graded Index Fiber Collimator," *IEEE Photonics Journal*, vol. 2, no. 3, pp. 469-481, 2010.
- [108] J. M. Kilpatrick, W. N. MacPherson, J. S. Barton *et al.*, "Phase-demodulation error of a fiber-optic Fabry-Perot sensor with complex reflection coefficients," *Applied Optics*, vol. 39, no. 9, pp. 1382-1388, 2000/03/20, 2000.
- [109] A. Othonos, "Fiber Bragg gratings," *Review of Scientific Instruments*, vol. 68, no. 12, pp. 4309-4341, 1997.
- [110] C. Ma, and A. Wang, "Signal processing of white-light interferometric low-finesse fiber-optic Fabry-Perot sensors," *Appl Opt*, vol. 52, no. 2, pp. 127-38, Jan 10, 2013.
- [111] E. W. Weisstein. "Nyquist Frequency," Jul 16, 2017; <http://mathworld.wolfram.com/NyquistFrequency.html>.
- [112] W. Zhang, J. Dai, B. Sun *et al.*, "Study on demodulation algorithm of fiber optic Fabry-Perot sensors based on spectrum adjusting." p. 68301N.
- [113] Wikipedia. "Resistance thermometer," [https://en.wikipedia.org/wiki/Resistance\\_thermometer](https://en.wikipedia.org/wiki/Resistance_thermometer).
- [114] I. OMEGA Engineering. "Tungsten-Rhenium Thermocouples," 5 Aug, 2017; <http://www.omega.com/techref/pdf/z202.pdf>.
- [115] R. I. Corporation, "Thermocouple Info," <http://www.thermocoupleinfo.com/>, 2011.

- [116] W. contributors. "Thermocouple," 20 August 2017; <https://en.wikipedia.org/wiki/Thermocouple>.
- [117] I. Gilson Engineering Sales. "Gilson Engineering Sales, INC. Thermocouple Technical Information," 2010; <http://www.gilsoneng.com/>.
- [118] R. M. Park, R. M. Carroll, P. Bliss *et al.*, "Chapter 2—Principles of Thermoelectric Thermometry," pp. 4-4-39, 1993.
- [119] R. E. Bentley, "Thermoelectric Hysteresis in Nickel-Based Thermocouple Alloys," *Journal of Physics D-Applied Physics*, vol. 22, no. 12, pp. 1902-1907, Dec 14, 1989.
- [120] P. Pavlasek, C. J. Elliott, J. V. Pearce *et al.*, "Hysteresis Effects and Strain-Induced Homogeneity Effects in Base Metal Thermocouples," *International Journal of Thermophysics*, vol. 36, no. 2-3, pp. 467-481, 2015.
- [121] I. M. Tougas, M. Amani, and O. J. Gregory, "Metallic and ceramic thin film thermocouples for gas turbine engines," *Sensors (Basel)*, vol. 13, no. 11, pp. 15324-47, Nov 08, 2013.
- [122] R. P. Benedict, "Thermoelectric Thermometry," pp. 74-126, 1984.
- [123] P. R. N. Childs, "Thermocouples," pp. 98-144, 2001.
- [124] R. E. Bentley, "Long-Term Drift in Mineral-Insulated Nicrosil-Sheathed Type-K Thermocouples," *Sensors and Actuators a-Physical*, vol. 24, no. 1, pp. 21-26, May, 1990.
- [125] N. A. Burley, "Nicrosil/Nisil Type N Thermocouples," *National Institute of Standards and Technology*, Omega, p. 4.
- [126] F. E. Ltd. "Fibre Cleaver – CT-30A," <https://www.fujikura.co.uk/products/fusion-splicers-and-accessories/fusion-splicer-accessories/fibre-cleavers-ct-30a/#productDescription>.
- [127] I. Photon Kinetics. "FK11 & FK12 Precision Fiber Optic Cleavers," 2017; <http://www.pkkinetics.com/products/productdetail.aspx?model=FK11>.
- [128] D. M. Mattox, "Physical Sputtering and Sputter Deposition (Sputtering)," pp. 343-405, 1998.
- [129] P. Sigmund, "Sputtering by ion bombardment theoretical concepts," vol. 47, pp. 9-71, 1981.
- [130] D. M. Mattox, "Deposition Processes," pp. 11-33, 2003.
- [131] T. F. C. Inc. "The Essential MacLeod," Jul 17, 2017; <https://www.thinfilmcenter.com/essential.php>.
- [132] T. Baghdasaryan, T. Geernaert, F. Berghmans *et al.*, "Geometrical study of a hexagonal lattice photonic crystal fiber for efficient femtosecond laser grating inscription," *Optics Express*, vol. 19, no. 8, pp. 7705-7716, 2011/04/11, 2011.
- [133] G. Ghosh, M. Endo, and T. Iwasaki, "Temperature-dependent Sellmeier coefficients and chromatic dispersions for some optical fiber glasses," *Journal of Lightwave Technology*, vol. 12, no. 8, pp. 1338-1342, August 1994, 1994.
- [134] G. M. Flockhart, R. R. Maier, J. S. Barton *et al.*, "Quadratic behavior of fiber Bragg grating temperature coefficients," *Appl Opt*, vol. 43, no. 13, pp. 2744-51, May 1, 2004.
- [135] D. Polyzos, M. Jinesh, W. N. MacPherson *et al.*, "Long-term stability testing of optical fibre Fabry-Perot temperature sensors," vol. 9852, pp. 985218, 2016.
- [136] Z.-L. R. Yun-Jiang Rao, Yuan Gong, "Interrogation and Multiplexing Techniques for FFP Sensors," *Fiber-Optic Fabry-Perot Sensors*, Fiber-Optic Fabry-Perot Sensors, pp. 129-154: CRC Press, 2017.
- [137] L. Stoch, M. Łaczka, and I. Wacławska, "DTA and x-ray diffraction study of the phase transformation of silica minerals," *Thermochimica Acta*, vol. 93, pp. 533-536, 1985.



- [138] D. Polyzos, J. Mathew, W. N. MacPherson *et al.*, "High temperature stability testing of Ge-doped and F-doped Fabry-Perot fibre optical sensors."
- [139] A. D. Yablon, "Optical Fiber Fusion Splicing," *Springer*, vol. 3.3, pp. 8, 2005.
- [140] L. T. Oikari R, Hernberg R., "High-temperature effects in fluorine-doped, fused synthetic silica fiber," *Applied optics, Optical Society of America*, vol. 36, no. 21, pp. 5058-63, July 20, 1997.
- [141] F. Gonthier, A. Hénault, S. Lacroix *et al.*, "Mode coupling in nonuniform fibers: comparison between coupled-mode theory and finite-difference beam-propagation method simulations," *Journal of the Optical Society of America B*, vol. 8, no. 2, pp. 416, 1991.
- [142] D. Marcuse, "Mode Conversion in Optical Fibers with Monotonically Increasing Core Radius," *Journal of Lightwave Technology*, vol. 5, no. 1, pp. 125-133, Jan, 1987.
- [143] P. M. Shankar, L. C. Bobb, and H. D. Krumboltz, "Coupling of Modes in Bent Biconically Tapered Single-Mode Fibers," *Journal of Lightwave Technology*, vol. 9, no. 7, pp. 832-837, Jul, 1991.
- [144] C. Richard M, "Hydrogen Sensing Using Palladium Coated Long Period Gratings," School of Engineering and Physical Sciences, Heriot Watt University, 2012.
- [145] I. H. Malitson, "Interspecimen Comparison of the Refractive Index of Fused Silica\*,†," *Journal of the Optical Society of America*, vol. 55, no. 10, pp. 1205-1209, 1965/10/01, 1965.
- [146] T. Haibara, T. Nakashima, M. Matsumoto *et al.*, "Connection loss reduction by thermally-diffused expanded core fiber," *IEEE Photonics Technology Letters*, vol. 3, no. 4, pp. 348-350, 1991.
- [147] P. Lecoy, *Fiber-Optic Communications*, March 2013 ed., p.^pp. 42-45, Wiley Online Library: Wiley-ISTE, 2013.
- [148] M. C. T. Bahaa E. A. Saleh, "Fundamentals of Photonics, 2nd Edition," *chapter 8 - FIBER OPTICS*, p. 1200: John Wiley & Sons, Inc., 2007.
- [149] J. S. Harper, C. P. Botham, and S. Hornung, "Tapers in single-mode optical fibre by controlled core diffusion," *Electronics Letters*, vol. 24, no. 4, pp. 245, 1988.
- [150] E. Atad-Ettedgui, B. J. Frey, J. Antebi *et al.*, "Temperature-dependent refractive index of silicon and germanium," vol. 6273, pp. 62732J, 2006.
- [151] G. Ghosh, Endo, M. and Iwasalu, T., "Temperature-Dependent Sellmeier Coefficients and Chromatic Dispersions for Some Optical Fiber Glasses," *JOURNAL OF LIGHTWAVE TECHNOLOGY*, vol. 12, no. 8, pp. 4, August 1994, 1994.
- [152] X. Zhang, D. Erickson, X. Fan *et al.*, "Measurements of thermo-optic coefficient of standard single mode fiber in large temperature range," vol. 9620, pp. 96200Y, 2015.
- [153] AMMRF. "Quantitative EDS X-ray microanalysis using SEM," <http://www.ammrf.org.au/myscope/analysis/eds/accuracy/>
- [154] AMMRF. "Accuracy, Precision and Detection Limits," <http://www.ammrf.org.au/myscope/analysis/eds/quantitative/>.